Master's Thesis

Utrecht University

Condensed Matter & Interfaces

Lanthanide Luminescence in Elpasolite Semiconductor Nanocrystals: Nanophosphors for Cutting Edge Display Technology

Author
Lars Sonneveld

Daily supervisor
Jur de Wit
Supervisor
prof. dr. Andries Meijerink
Second examiner
dr. Celso de Mello Donegá

February 28, 2022

Utrecht University

Layman's summary

In this thesis, we research phosphors for display technology. Phosphors are materials which emit visible light under UV light. Some phosphors can also emit light when visible light shines on it. Phosphors that convert blue light to red and green light are highly desirable. This is because displays are commonly made by using a blue LED light as the main light source. This blue light source is coated with red and green emitting phosphors. As a result, some of the blue light is absorbed and converted to red and green light. The combination of the red, green and blue light looks like white light to the human eye. In displays, this white light source is located in the back of the screen. With color filters, we can separate the red, green and blue components again from the white light source. Through additive color mixing, only the primary colors red, green and blue are needed to display every single color known to the human eye. This way we can show every color on a display screen.

To separate the red, green and blue components from the white light source, it helps to have a white light source with very pure red, green and blue components as a starting point. Therefore, we need phosphors that convert the blue light to very pure red and green light. Terbium and europium are two elements that belong to the lanthanide group, which is often located at the bottom of the periodic table. Terbium and europium in elemental form just look like ordinary metals. However, when you put a very small amount of these elements inside of a crystal, they can show luminescence. When they absorb UV-light, terbium glows bright green and europium glows warm red, shown in **figure 1**. Their luminescence is very pure green and red and therefore they exhibit very desirable properties for displays.

The drawback to terbium and europium is that they absorb light very weakly. As a result, when they are coated on blue LED lights, most of the blue light will pass through and no red and green light is produced. In this thesis, we try to incorporate terbium and europium into a semiconductor crystal which absorbs the light very strongly for terbium and europium. Semiconductors absorb light very strongly and for this reason they are also used in solar panels. In solar panels, light is absorbed by a semiconductor and this creates energy that is turned into electricity. In our research, we hope that the energy created by light absorption is absorbed

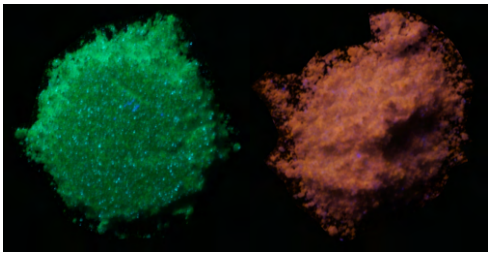

Figure 1: Photograph of phosphors containing terbium (left) and europium (right) under UV light

by terbium and europium so that they can emit green and red light. This way we let the semiconductor do the work for terbium and europium.

There is one more thing we want aside from strong absorption of blue light that is converted to red and green light, namely very small crystals. A new innovation in display technology is microLED displays. In microLED displays, the tiny pixels that make up a display are each very small blue LEDs, which are coated with red and green phosphors. Pixels can be as small as 0.150 millimeter. This is close to the diameter of the grains of phosphors, which makes an even coating of the phosphors on the microLEDs impossible. Therefore, we want to make nanocrystal phosphors. Nanocrystals have sizes of between 1 and 100 nm. For reference, the width of a human hair is about 100,000 nm. Because nanocrystals are so small, they require challenging special synthesis techniques.

We discovered two new red and green phosphors in this thesis. We found that in the crystal Cs_3InCl_6, incorporating a small amount of europium resulted in bright red luminescence and a small amount of terbium resulted in bright green luminescence under UV light. The phosphors absorb UV light very strongly. However, the crystal is not able to absorb blue light and we have only made large crystals yet, which are actually the powders shown in **figure 1**.

Abstract

MicroLED is promising new display technology that can significantly improve the quality of modern displays. For the technology to succeed, new phosphors have to be developed which are strongly absorbing, have small dimensions and have narrow band red and green emission. Semiconductor nanocrystals such as CdSe or perovskite quantum dots show great potential for microLED, but the use of cadmium and lead presents toxicity issues and perovskite nanocrystals suffer from stability issues. In this thesis, we investigate doping non toxic elpasolite semiconductor nanocrystals with lanthanide ions and study the energy transfer mechanism of the semiconductor host to the lanthanide ions. We concluded that in bismuth-based elpasolites, the emission of Eu^{3+} and Tb^{3+} is quenched due to charge transfer quenching. In indium-based elpasolites, charge transfer quenching is less of an issue and consequently we found that Cs_3InCl_6 exhibits intense red or green emission from the Eu^{3+} or Tb^{3+} dopants, which possibly is sensitized by the host material. We found that the energy transfer of host to lanthanide likely occurs by trapping of photoexcited charge carriers on lanthanide centers resulting in a charge transfer state that relaxes to the f-orbital energy levels of the lanthanides, followed by emission from f-f transitions. Our findings show the potential of elpasolite semiconductors as a host for lanthanide dopants. With further shifting of the absorption band of Cs_3InCl_6 towards the blue region, it could have potential for application in microLED.

Contents

1 Introduction **9**

2 Theoretical background **13**

2.1 Display technology 13

2.2 Photoluminescence 16

2.3 Semiconductors 19

2.3.1 Semiconductor luminescence 20

2.3.2 Semiconductor nanocrystals 22

2.4 Lanthanide ions 23

2.4.1 Properties of lanthanides 23

2.4.2 Considerations when doping lanthanides ions 24

2.4.3 Spectroscopy of lanthanide ions 25

3 Experimental methods **33**

3.1 Chemicals 33

3.2 Synthesis procedures 33

3.2.1 Cs_2AgBiX_6 (X = Cl, Br) and $Cs_2NaBiBr_6$ nanocrystals 33

3.2.2 $Cs_2NaBi_xEu_{1-x}Cl_6$ (x = 0, 0.25, 0.5, 0.75, 1) microcrystals 34

3.2.3 $Cs_2AgInCl_6$ 35

3.2.4 Cs_3InCl_6 35

3.3 Characterization 36

3.3.1 Structural characterization 36

3.3.2 Optical characterization 36

3.3.3 Low temperature measurements 37

4 Results and discussion **39**

4.1 Bismuth-based elpasolite materials 39

4.1.1 $Cs_2AgBiCl_6$ nanocrystals 40

4.1.2 $Cs_2AgBiBr_6$ 52
4.1.3 $Cs_2NaBi_xEu_{1-x}Cl_6$ microcrystals 63
4.1.4 $Cs_2NaBiBr_6$ 67
4.2 Indium-based elpasolite materials 70
4.2.1 $Cs_2AgInCl_6$ 71
4.2.2 Cs_3InCl_6 72

5 Conclusion and outlook **81**

Chapter 1

Introduction

Not a day goes by that you don't look at a display device. Whether it be checking your smartphone screen for messages or watching the news on your television. Displays act as an important bridge between the vast amount of information available and society. Chances are you are reading this on a display right now. It is no wonder that display technology is constantly evolving to provide the best user experience possible.

The picture quality of a display can be improved in several ways. Among the most important factors for a high quality display are a high range of colors and deep black levels [1]. A high color range can be obtained by creating pixels with very pure red, green and blue components. The most widely used display technology is liquid crystal display (LCD) technology [2]. A white backlight consisting of a combination of red, green and blue light is located in the back of the screen. Various layers of polarizers, liquid crystals and color filters work together to create millions of pixels which can individually display a color created by a combination of red, green and blue light. With only these three colors, every possible color known to the human eye can be displayed [3].

Figure 1.1 shows schematically how the pixels of a display look upon magnification along with a close up picture of a display. To achieve the widest range of colors, these individual red, green and blue components have to be as pure as possible. To create these pure colors in a

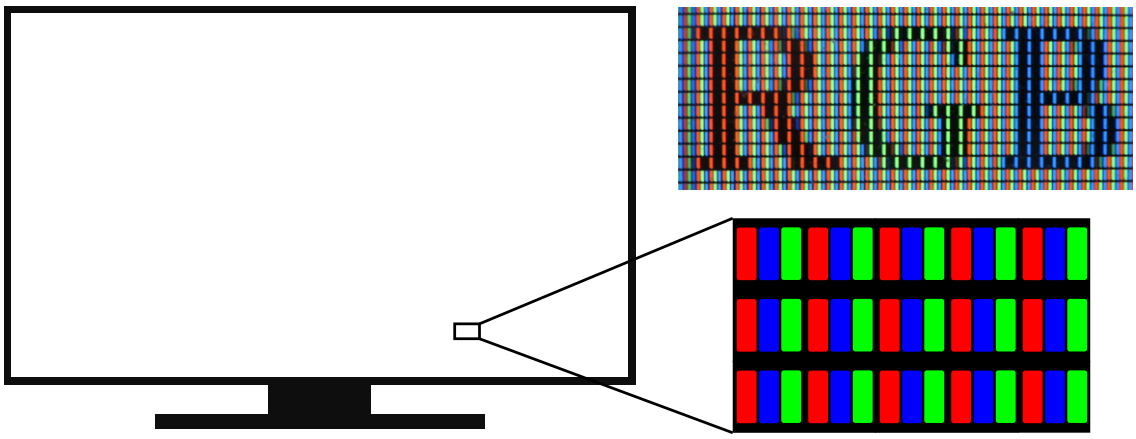

Figure 1.1: Pixels in a display up close. The drawing (left) shows a magnification of the white pixels of a display. The picture (top right) shows a close up of a display in reality.

backlight, a LED chip is used which emits blue light with a very narrow emission band. The LED-chip is coated with phosphors which convert some of the blue emission to narrow band red and green emission. By controlling the amount of phosphors applied on the LED-chip, a light source with a correct balance of red, green and blue light can be made. Traditional phosphors used for these applications are commonly inorganic crystals with a small amount of luminescent "impurities". These impurities are intentionally doped into the crystal lattice and often are transition metal ions or lanthanide ions. Two examples of commercially used phosphors are K_2SiF_6:Mn^{4+} (red emitting phosphor) and $\beta-$SiAlON:Eu^{2+} (green emitting phosphor) [4]. In these phosphors, the luminescent impurities are respectively Mn^{4+} and Eu^{2+}. These "activator" ions absorb the blue light from the LED-chip and emit red and green light through the process of photoluminescence (PL). High quality phosphors with narrow emission bands are highly desired as they increase the range of colors that a display can produce.

The backlight of an LCD display is always on which makes deep black levels difficult to realize with LCD technology. To create black on an LCD display, the white light from the backlight is blocked by filters. These filters are not perfect though. This results in slippage of some of the light through the filters. Consequently, black is not truly black. You might recognize this yourself: a black background on an LCD screen might show a slight blue hue. The poor black levels result in poor contrast values. A promising technology which is being developed for displays is microLED. Over the years, research has been able to reduce the size of LEDs to less than 100 μm [5, 6], which are accordingly called microLEDs. In microLED displays, the individual pixels are three very small blue emitting microLED chips coated with red or green emitting phosphors or no phosphor for the blue component. Therefore the pixels individually emit red, green and blue light. Since the pixels itself are microLEDs, the pixels are self-emitting and can turn on and off individually. So when black is displayed, the pixel is fully turned off, resulting in a truly black pixel. This results in superior contrast values and deep black levels.

The development of phosphors for microLED poses a challenge, as traditional phosphors are unsuitable for microLED [7]. MicroLED chips are so small that their size is comparable to the grain size of traditional phosphors. Therefore it is impossible to create an even coating of the phosphor on the microLED chips. Additionally, only a very thin layer of phosphor is applied and to completely absorb the incoming blue light extremely strong absorption is needed [8]. Traditional phosphors generally lack this strong absorption. Therefore, new phosphors have to be developed which are strongly absorbing and have small dimensions.

A promising candidate for microLED phosphors are semiconductor nanocrystals (SNC's). SNC's kill two birds with one stone, as semiconductors have extremely strong absorption due to band-to-band absorption and their size is well-below that of the microLED chips. Nanocrystals made of type II-VI semiconductor CdSe have reached photoluminescence quantum yields (PLQY) of more than 90% [9, 10]. More recently, lead halide perovskite nanocrystals have drawn a lot of attention, boasting PLQY's of up to 100% [11, 12]. However, both type II-VI SNC's and perovskite SNC's have toxicity concerns as they contain cadmium and lead [1]. Perovskite SNC's also suffer from stability issues [13].

A promising alternative to lead halide perovskite nanocrystals emerged when McClure *et al.* [14] first published about "lead-free halide perovskite semiconductors". These materials substitute the toxic divalent lead in lead halide perovskites for monovalent silver and trivalent bismuth, which alternate each other in the crystal lattice. This results in a non-toxic and more stable crystal with similar properties to perovskite nanocrystals. Since then, many more of these

"double perovskite" crystals have been made [15]. The material is often referred to as double perovskites due to their similarity to perovskites, but the correct naming for the crystal structure is the "elpasolite" structure. Like perovskites, these materials have very strong band-to-band absorption. The downside though, is that their emission is mostly trap-related and consequently very broad, which is undesired for narrow band phosphors for display technology. Additionally, their PLQY is typically significantly lower than their perovskite counterparts [15]. A promising strategy to improve the PL characteristics is to dope the material with narrow-band luminescent impurities, like in traditional phosphors. The elpasolite crystal structure lends itself excellently to doping with lanthanides. The crystal has a large trivalent site with a high coordination number of 6, suitable for the large trivalent lanthanide ions. Various lanthanide ions have successfully been doped into elpasolite crystals enhancing their PL properties, showing promising results for this strategy [16–19].

In this thesis we investigate doping various elpasolite systems with lanthanides. The lanthanide ions Eu^{3+} and Tb^{3+} are known for their respectively red and green sharp emission lines due to intraconfigurational f-f transitions [20]. This makes them very suitable dopants for narrow band phosphors used in displays. However, these f-f transitions are forbidden by the selection rules and therefore have very weak absorption [20]. An established method to improve the absorption of lanthanide-based luminescent materials is using a sensitizer. This sensitizer absorbs light strongly and then excites a lanthanide ion in the lattice through the process of energy transfer (ET). In our case, the sensitizer is the elpasolite semiconductor nanocrystal host lattice. This way we obtain a stable non-toxic nanocrystalline material with strong host absorption and desired red and green emission from the Eu^{3+} and Tb^{3+} dopants, fulfilling the demands for phosphors for microLED application. Aside from making a microLED phosphor, we investigate the ET mechanism from host lattice to lanthanide. There have been speculations about the ET mechanisms in these materials [16, 18, 19], but this is a concept which is often not well-understood. We aim to elaborate on possible ET mechanisms in these materials.

In order to achieve these goals, we synthesize the microcrystals and nanocrystals of various elpasolite systems and dope them with various lanthanide ions. The microcrystals are synthesized rather easily by precipitation from solution or in some cases by high temperature solid-state reaction in an evacuated quartz tube. The nanocrystals are synthesized with the hot-injection method. To investigate the PL performance and ET mechanism we verify the crystal phase of the compounds and we perform various optical experiments, such as absorption, PL spectroscopy and PL decay measurements.

This thesis is outlined as follows: after this introduction in chapter 2, we go over the theoretical background needed to understand the concepts discussed in this thesis. In particular, we discuss the theory behind display technology, photoluminescence, semiconductors and lanthanides. Chapter 3 discusses the experimental procedures used for synthesizing the materials as well as the characterization methods used for the analysis of the materials. Chapter 4 presents the results of the research on the synthesized materials. We analyze the structural properties of the materials and we thoroughly discuss the PL properties and mechanisms of ET between the host material and lanthanides. In chapter 5, we conclude with the main findings of our research. An outlook is given about the directions of future research.

Chapter 2

Theoretical background

This chapter provides the theoretical background to understand the later chapters of this thesis. The chapter is divided into several sections: First, we discuss display technology in more detail. Following this, the general theory of photoluminescence is briefly discussed. After this, we go more into depth about semiconductors and their optical and electronic properties and the elpasolite structure. Lastly, we discuss the optical and electronic properties of lanthanide ions.

2.1 Display technology

A display consists of arrays of millions of pixels. On a display, the individual pixels display a color and intensity which corresponds to the color of an image at the pixels location. A pixel consists of a red green and blue component. The red green and blue components light up with different intensities. As the viewing distance increases, the human eye cannot distinguish the individual red green and blue components anymore and the pixel color is perceived as a combination of the three subpixel colors. By combining these three colors in different ways, every color can be made [3]. A display with a wide range of colors can be made by selecting phosphors which have very narrow red and green emission bands. The more pure the individual red, green and blue components are, the greater the range of colors the pixels can display.

The color range can be visualized in a chromaticity diagram developed by the Commission Internationale de l'éclairage (CIE) [21]. **Figure 2.1** shows an example of the chromaticity diagram. In the diagram, colors correspond to specific coordinates. The outer edges of the diagram show the pure colors with corresponding wavelengths. As light of different wavelengths is mixed, the coordinates of the color shift more to the middle of the diagram. If you display three different colors on the chromaticity diagram, you can connect them to form a triangle. The area this triangle surround represents every color you can obtain by mixing the three colors. It now becomes clear why having pure red, green and blue components is important. A triangle made with pure 450 nm, 520 nm and 620 nm light spans almost the complete chromaticity diagram. So with these three wavelengths you can almost cover the entire the entire color range known to the human eye. However, the RGB components in displays are not monochromatic red or green light, therefore the triangle is contracted inwards. The triangle in the figure represents the RGB color gamut, a common color range standard in display industry [1]. It is clear that the triangle does not cover a significant part of the available colors. This illustrates the significance of research for narrow band phosphors.

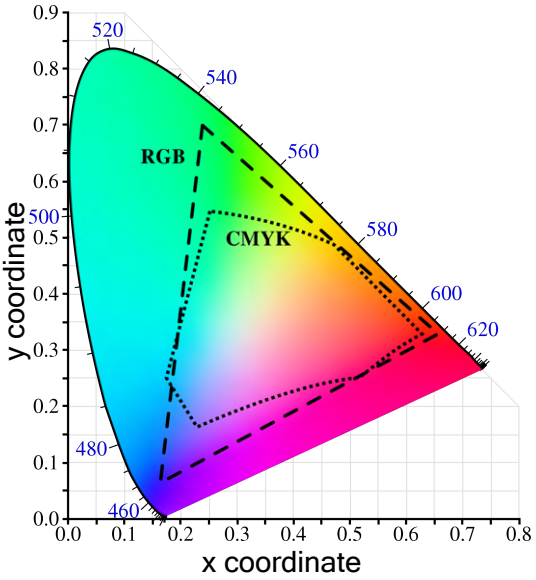

Figure 2.1: The CIE color space, showing the RGB color gamut.

To understand why LCD displays lack in contrast values a brief explanation of the technology is given. A simplified schematic of the layers of an LCD screen is shown in **figure 2.2 (a)**. In the back, a white backlight is located which consists of blue LEDs coated with red and green emitting phosphors. The white light first passes through a polarizing film to polarize the light along the vertical direction. Then the polarized light hits the TFT-LCD layers. These layers consists of a thin film transistor (TFT) layer with a transparent electrode, followed by a layer of a liquid crystal matrix, follow by another transparent electrode. When the TFT is turned on, a voltage is applied between the electrodes and this causes the liquid crystals to twist and form a helix. When polarized light passes through the helix, the direction of the polarization twists with the helix, shown in **figure 2.2 (b)**. As a result, when the TFT is on, the polarized light is twisted 90 degrees and it is able to pass through the second horizontal polarizing film.

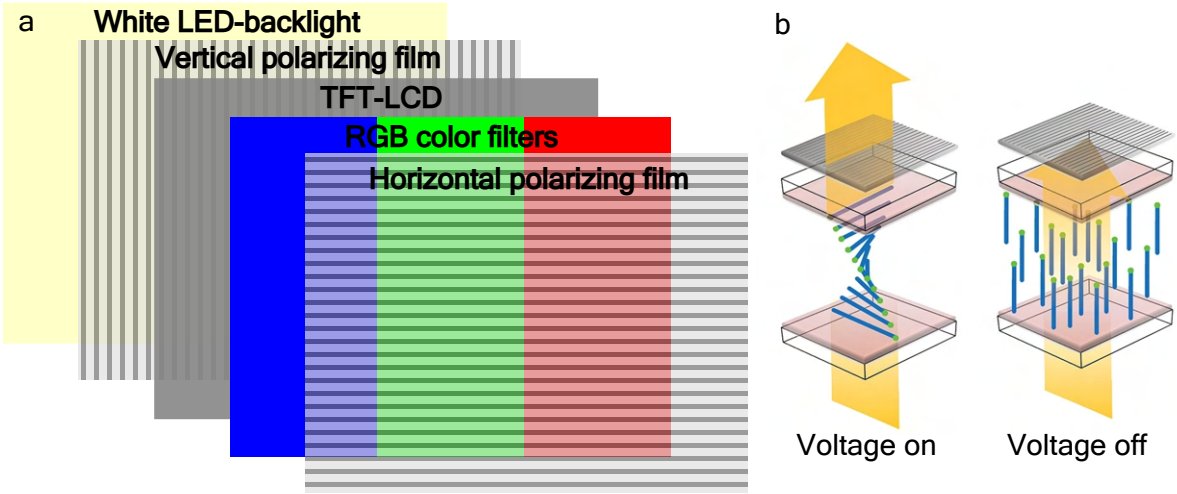

Figure 2.2: The inner workings of an LCD display. **(a)** A schematic of the different layers of an LCD display. **(b)** Schematic showing the twisting of the liquid crystals when applying a voltage, allowing light to pass through the second polarizer.

When the TFT is off, the light is polarized in the vertical direction and cannot pass through the second horizontal polarizing film. Before the light passes through the second polarizer, it passes through red, green and blue color filters. Each pixel has a red, green and blue color filter. Each color filter corresponds to one TFT and thus every pixel consists of a red, green and blue subpixel that transmit light individually.

The drawback to LED-LCD screens is that the backlight is always on and the double polarizing films are unable to block the light fully. As a consequence, black is not truly black on these displays which results in low contrast values. This is especially noticeable in dark scenes. There have been many innovations to improve this quality in displays. One of the most popular is organic light emitting diode (OLED). In OLED, the pixels consist of electroluminescent organic molecules between a cathode and anode. When a voltage is applied across the electrodes, the electroluminescent molecules emit light [1]. Because the light emitters are molecules and thus very small, they are small enough to integrate as individual pixels. This way pixels can be turned on and off individually. So when black is displayed, the pixel is off resulting in truly black. However, the drawback to OLED is that production costs are very high and since the emitters are organic molecules they have issues with stability [1, 22]. The stability issues results in short lifespan of display and also limit the amount of current that can be passed through the emitters, resulting in lower brightness. Higher currents and thus higher brightness is possible, however this carries the risk of the degradation of the pixels. This presents itself as burnt in spots on the screen where the same image is displayed for prolonged amounts of time, such as logos of television channels.

MicroLED is an interesting new technology which tackles the issues LCD and OLED displays have. Because the microLED chips are individual pixels and can turn on and off by themselves, they bypass the need for a layer of liquid crystals. An example of a schematic of a pixel in a microLED display is shown in **figure 2.3 (b)**. Blue emitting microLEDs are placed on an array of LED drivers. Two microLED chips are covered with a phosphor to convert the blue light to green and red light. One microLED chip is not covered with a phosphor and the blue light passes through freely. Red, green and blue color filters can still be placed on the subpixels to improve the color quality of each of the subpixels. Using this system, individual subpixels can be turned off. As a result, black is truly black in microLED displays, improving the contrast and thus picture quality of the display. The advantage compared to OLED is that this technology is based on inorganic phosphors, which have significantly better stability. Therefore, microLED displays can have higher brightness and longer life span [1, 22].

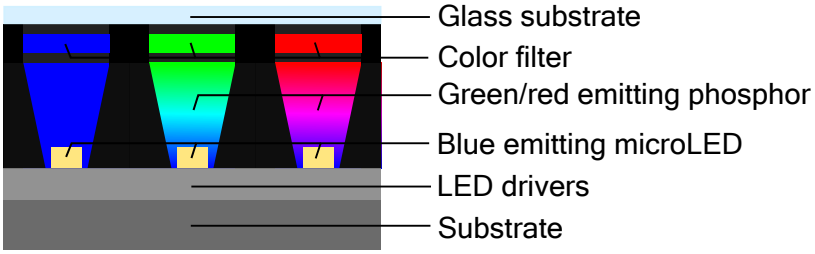

Figure 2.3: Schematic of a microLED pixel.

2.2 Photoluminescence

The phosphors convert the incoming blue light to red and green light through the process of photoluminescence. Photoluminescence is the process of light emission from a material after absorption of photons. When a material absorbs a photon, the system is excited from its ground state into an excited state. From this excited state multiple processes can occur. The processes involved with photoluminescence are explained in this section. In the explanation of these concepts as well as in the rest of this thesis, configuration coordinate diagrams are used. Therefore, these will now be briefly explained.

Consider a central ion which is surrounded by ligands. Intuitively, one can think of the bonds between the central ion and its ligands as springs. The central ion is in equilibrium when the ion is stationary and the force acting on the ion in every direction is equal. At this point the ion is in an equilibrium position. Any deviation from this equilibrium position R_0 results in a restoring force which is proportional to the displacement: $F = -k(R - R_0)$, where k is the spring constant and R is the displacement. Integrating the force with respect to the displacement yields the potential energy: $E = \frac{1}{2}k(R - R_0)^2$ [23]. This is a parabolic function in which the potential energy is increased upon deviation from the equilibrium, shown in **figure 2.4 (a)**.

The potential energy of the linear spring is a good model for macroscopic systems, but at the small scale of atoms the model breaks down. At this scale, quantum effects present itself and the system can only have certain discrete energies. These energies can be calculated by solving the Schrödinger equation. The quantum mechanical description of this system - called the quantum harmonic oscillator - yields discrete energy levels on the potential energy parabola with energy $E_n = (n + \frac{1}{2})\hbar\omega$, where n (= 0, 1, 2, ...) is the vibrational quantum number and ω is the frequency of the oscillator [23]. **Figure 2.4 (b)** shows the quantum harmonic oscillator with the energy levels of the first ten vibrational modes. The discrete energy levels are states which have a corresponding electron wavefunction. The probability densities of the wavefunctions are shown on the energy levels. The energy of the systems can only have the values of the discrete energy

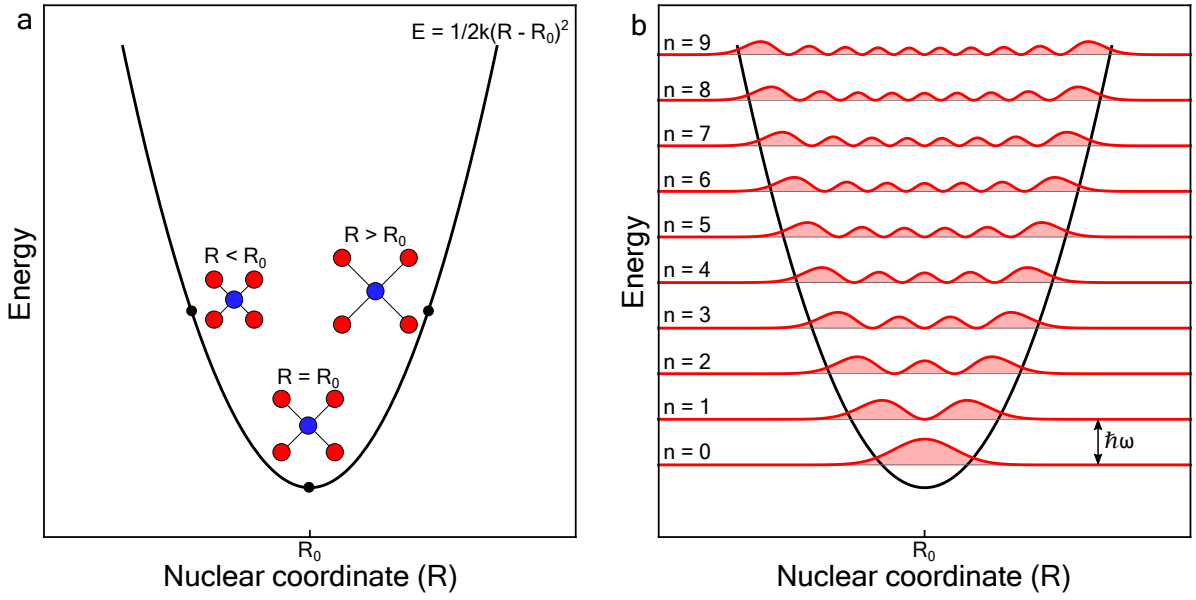

Figure 2.4: Potential energy curves of the **(a)** classical model and **(b)** quantum mechanical model.

levels in the figure. This gives rise to well-defined transitions between different vibrational states. The probability densities show that the probability of finding the central ion is highest at R_0 in the lowest vibrational state. In higher vibrational states this is at the edges of the parabola.

These parabolas can be used to describe an electronic state with its corresponding vibrational energy levels. In a configuration coordinate diagram, different electronic states of an ion in a crystal are displayed as different parabolas. For example, an electronically excited state may be represented by a parabola with a higher energy than the ground state parabola. Electronic transitions occur practically instantaneous when compared to nuclear displacement, therefore the nuclear coordinates are equal right before and after an electronic transitions [24]. Consequently, an electronic transition is represented by a vertical arrow in the configuration coordinate diagram. Transitions are more likely to occur if there is overlap of the wavefunctions of the two transitions [24]. Since the probability density of the wavefunctions is located near the edges of the parabola, arrows are usually drawn from edge to edge of the parabola, as the wavefunctions overlap between transitions is usually largest there. This way different electronic states can be represented in one diagram to explain transitions between states.

To see how these of these potential energy curves can be applied, we explain the process of photoluminescence using them. The initial step in the process of photoluminescence is the absorption of a photon. The luminescent center absorbs a photon and is promoted to an excited state. There are various factors which influence the way a luminescent material absorbs its energy. These factors influence the position, broadness and intensity of an absorption band.

In the simplest situation, the excitation of a luminescent ion is solely an electronic transition. A photon reaches the luminescent center and an electron is excited from its ground state to an excited state. **Figure 2.5 (a)** shows what this situation looks like in a configuration coordinate diagram. An energy transition takes place from the lowest vibrational level in the ground state to the lowest vibrational level in the excited electronic state with a higher potential energy, indicated by the upwards arrow. This is a purely electronic transition and results in a narrow

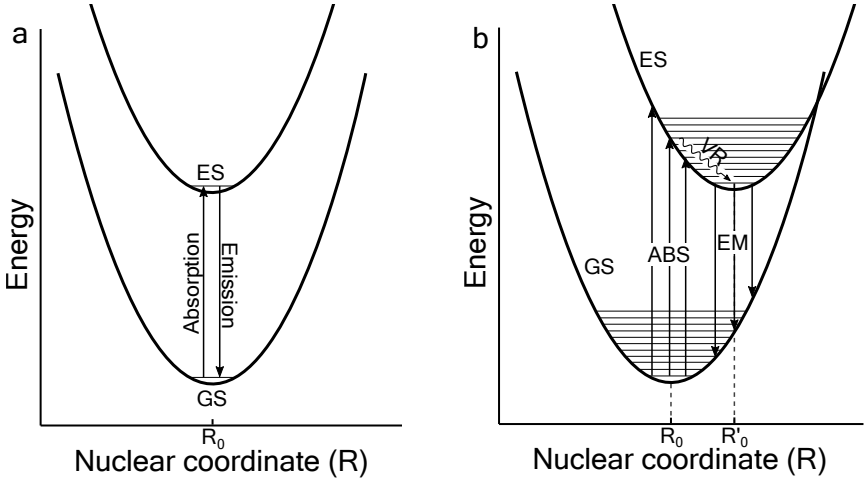

Figure 2.5: Configuration coordinate diagrams showing absorption and emission. **(a)** Absorption of a photon, exciting from the lowest vibrational level of the ground state (GS) to the lowest vibrational level of the excited state (ES), followed by emission. **(b)** Absorption of a photon, exciting into an ES in a higher vibrational level. This is followed by vibrational relaxation to the lowest vibrational state of the ES. Then emission occurs from the offset ES, resulting in broad emission with a large Stokes shift.

absorption band. The absorption band is narrow because only one transition occurs with a single energy: that of vibrational level 0 of the ground state to vibrational level 0 of the excited state. This transition is called the zero-phonon line. The position of these transitions on the spectrum is dictated by the energy difference between the ground state and the excited state.

In a similar process, emission can occur. After absorption, the system is in an excited state. The excited state is energetically unfavorable and the system wants to return to a lower energy state. The system can then relax to the ground state while emitting a photon, indicated by the downwards arrow. This process is essentially the inverse of absorption. The emission of the photon occurs from the same energy level after absorption and consequently is also very narrow and roughly equal in energy to the absorption peak.

Although sharp line absorption and emission does exist, it is much more common to see broad absorption and emission bands. This is the case because more often than not, the excited state parabola does not align with the ground state parabola in the y-direction of the configuration coordinate diagram. When a luminescent center enters an excited state, its electronic configuration is changed. Valence electrons which contribute to bonding can be excited to orbitals which contribute differently to bonding, for example anti-bonding orbitals. When this happens, the bonding strengths of the luminescent center to its ligand changes, causing a different equilibrium position of the parabola. This results in an offset of the equilibrium position of the excited state parabola (R_0') to the ground state parabola (R_0), shown in **figure 2.5 (b)**. When the excited state band is offset, excitation by a photon promotes and electron to a higher electronic state, but also to a higher vibrational state, shown in **figure 2.5 (b)** as upwards arrows. The transitions are combined electronic and vibrational transitions, which are accordingly called vibronic transitions. Multiple of these vibronic transitions can occur which results in a spectrum with several vibronic transition peaks. Due to line broadening these peaks form a continuous absorption band, however in some cases the discrete vibronic peaks can be distinguished, especially at cryogenic temperatures.

The emission is also different when the excited state band is offset. After absorption, the system is in an electronic and vibrational excited state. Before emission occurs, the excited state first non-radiatively relaxes to the lowest vibrational state of the excited state parabola. From there, emission occurs in a similar fashion to absorption: the offset of the excited state parabola also results in combination of vibronic transitions in the emission spectrum, shown by the downward arrows in **figure 2.5 (b)**. The system is then in the electronic ground state but still in a higher vibrational state, so from there it can non-radiatively relax to the vibrational ground state. Due to the vibrational relaxations after absorption, the energy of the emitted photons is lower compared to absorption, resulting in a shift of the emission peak to lower energies relative to the absorption peak. This shift is called the Stokes shift. Systems with an excited state with a large offset typically have a large Stokes shift.

The intensity of an absorption band is determined by selection rules. Selection rules dictate whether an electronic transition is allowed or forbidden. Allowed transition can freely occur and result in strong absorption of light. Forbidden transitions theoretically cannot occur. In practice however, these transition still occur albeit weaker, because the selection rules can be relaxed. The analogy of a traffic light is often used: when the light is green, everyone crosses the street. When the light is red, people do not cross the street, however there will always be a few daring individuals which cross the street anyways. There are two different selection rules: the parity selection rule and the spin selection rule. The parity selection rule applies to

luminescent centers with inversion symmetry. It states that in order for a electronic transition to occur, there must be a change in parity of the wavefunctions of the initial and the final state. This means that electronic transitions between the same orbitals are forbidden, i.e., s-s, p-p, d-d, f-f transitions. The spin selection rule dictates that an electronic transition is forbidden if the transition involves a spin flip [20].

Like absorption transitions, the radiative transition to the ground state can also be forbidden by the selection rules. This does not necessarily result in emission with lower intensity though. A forbidden emission transition is characterized by a long lifetime of the emission. Fully allowed transitions typically have lifetimes in the nanosecond range. Forbidden transitions can have emission lifetimes in the microseconds range [20].

From the excited state, non-radiative relaxation to the ground state can also occur, resulting in quenching of the emission. The different luminescence quenching mechanisms is explained separately in the next sections for each specific case.

2.3 Semiconductors

Semiconductors are a class of materials with interesting properties that are somewhere in between insulators and metals. They are like insulators in the sense that there is a gap between the valence band and the conduction band of the material. However, despite of the band gap, semiconductors can conduct electricity similar to metals. This conductivity arises due to the formation of charge carriers. Charge carriers are electronic particles that are generated when an electron is excited from the valence band to the conduction band of the material. The electron is a charge carrier which is in the empty orbitals of the material and it can travel from orbital to orbital in the material. When the electron is excited to the conduction band, it leaves behind an empty spot in the valence band. This is where another charge carrier is generated, the hole. While the hole itself is not a particle, electrons in the valence band can constantly fill up the holes place, changing the holes location. This effectively results in a positively charged hole traveling through the material. While the hole is not actually a particle, it is often described as one since it behaves exactly opposite to an electron. Therefore holes are called quasiparticles. An electron-hole pair is often also called an "exciton". These charge carriers in a material give rise to the conductivity of the semiconductors [25].

Charge carriers can be generated in multiple ways, most notably heat and light. The thermal radiation of heat can promote electron from the valence band to the conduction band, generating charge carriers. From this it can be understood that the conductivity of a semiconductor increases with temperature, contrary to metals. If a semiconductor is hit by light with an energy of more than the band gap, electrons can also be promoted from the valence band to the conduction band. This is the theory behind solar panels: simply put, light with an higher energy than the band gap hits a semiconductor solar panel and charge carriers are formed in the solar cell. These charge carriers are harvested to produce electricity.

It is important to note that charge carriers can also be generated in insulators. Therefore, insulators can in theory be made conductive as well. The charge carriers in insulators are not mobile however, they have a hard time travelling through the material. In semiconductors the charge carriers are much more mobile. This is due to higher delocalization of the charge carriers compared to insulators. This delocalization arises from the nature of the elements

that the semiconductor consists of and due to the overlap of the orbitals of the elements in the crystal. Extremely electronegative elements such as fluorine hold on to their electrons very strongly and therefore do not promote delocalization. The other extreme is metals. In metals the electrons are completely delocalized over the material, creating a sea of electrons. Orbital overlap between the constituents of a crystal can also promote delocalization. For example, $PbCl_2$ is an insulator, while $CsPbCl_3$ is a semiconductor. This is a result of how the elements are arranged in the crystals. In $CsPbCl_3$, the crystal forms [PbCl6] corner sharing octahedra. This forms chains of Cl-Pb-Cl-Pb-Cl throughout the crystal, resulting in great orbital overlap between the crystals constituents and delocalization of charge carriers along the orbitals. These chains are not present in $PbCl_2$, resulting in more localized bond between Pb and Cl.

2.3.1 Semiconductor luminescence

Semiconductors can also exhibit photoluminescence. Like absorption of light promotes an electron to the conduction band leaving behind a hole, the electron-hole pair can also recombine: the electrons relaxes from the conduction band to the valence band. This process emits a photon with an energy roughly equal to the band gap energy and is called band edge emission. Because the states involved in the transitions are delocalized and not from one center localized in the crystal, the process cannot be represented with the configuration coordinate diagram. Instead, these transitions are often displayed in a schematic shown in **figure 2.6**. The transition indicated by arrow 1 indicates free exciton recombination. As the figure suggests, there are more possibilities for exciton recombination. While free exciton recombination can occur, is is more common that the recombination involves a state within the band gap. These states are often present due to defects in the material. Most of the time, emission with an energy close to the band gap energy originates from recombination of an electron (hole) with a hole (electron) that is in a shallow trap with an energy just above (below) the valence (conduction) band. Emission can also occur when an electron or hole is trapped in a state deeper within the band gap. This emission has a significantly smaller energy than the band gap and is often broad.

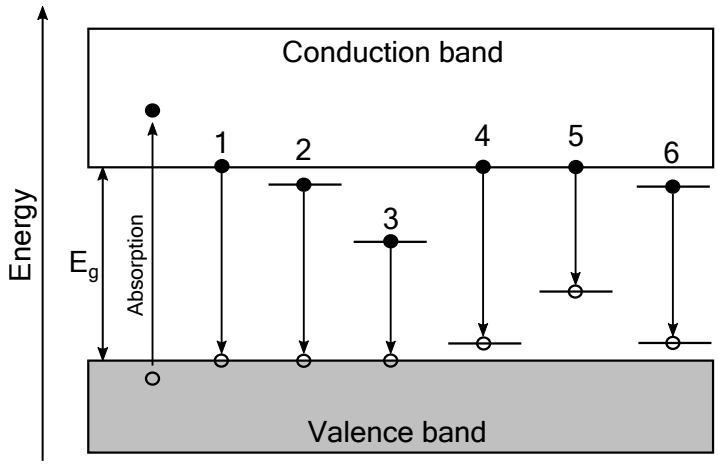

Figure 2.6: The energy band model, showing the conduction band and the valence band. The different transitions are: (1) Free exciton recombination. (2) Near band-edge recombination of a free hole and an electron in a shallow trap. (3) Recombination of a free hole with an electron in a deep trap. (4) Recombination of a free electron with a hole in a shallow trap. (5) Recombination of a free electron with a hole in a deep trap. (7) Donor-acceptor recombination.

A peculiar case of emission due to exciton recombination is self-trapped exciton (STE) emission. STE emission occurs when a electron or hole recombines with a self-trapped hole or electron. Electrons and holes can get trapped in the crystal due to lattice deformations. Self-trapping occur in "soft" lattices that have strong electron-phonon coupling. In simple terms, when electrons couple strongly to phonons, the crystal lattice easily deforms around the electrons due to their charge. This effect is strong in soft ionic crystal. The deformation of the lattice around a charge carrier can ultimately result in the trapping of a charge carrier: when the deformation around the charge carrier results in a more stable state, the carrier can be localized at the deformation, called self-trapping. Self-trapping is hard to visualize in a configuration coordinate diagram or in the figure of **figure 2.6**, because it involves the transition from the delocalized free exciton state to a localized STE state. However, we can try to visualize it in a configuration coordinate diagram. The situation is shown in **figure 2.7**. The free exciton is displayed as an excited state band in the configuration coordinate diagram. This is technically incorrect, since it implies that the free exciton state is a localized state in the crystal. However, the figure still serves as a good illustration. The free exciton state represents an electron in the conduction band and a hole in the valence band. In this instance, the hole causes a local deformation of the crystal lattice. The deformation stabilizes the hole and therefore the STE state has a lower energy than the free exciton state. That causes the hole to be stuck in the more stable state, effectively trapping itself. Because the trapping induces a strong lattice deformation and thus a change in bond lengths, the STE band is significantly offset from the free exciton band. As we discussed earlier, emission from this state then results in a large Stokes shift of the emission and a broad emission band.

Quenching of semiconductor luminescence happens in several ways. Most often, quenching occurs through a defect state within the band gap [26]. When charge carriers are generated, they easily travel through the material and can very easily be trapped on defects in the crystal, such as vacancies or surface states. Sometimes, emission can occur from these defect states, but often it leads to quenching of the luminescence. The luminescence of self-trapped excitons is often strongly quenched. When we look at the configuration coordinate diagram of **figure 2.7**, we see that the STE state has a large offset from the ground state parabola. This causes the parabolas of the STE state and GS to overlap. The overlap of these bands shows that there is wavefunction overlap between the STE state and the GS at higher vibrational levels. Via this route "crossover"

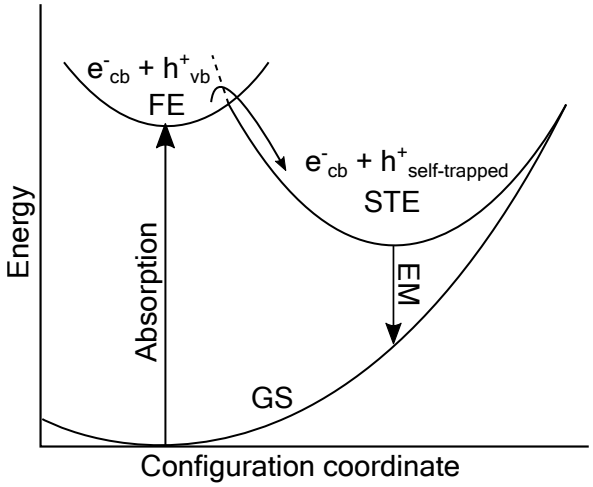

Figure 2.7: Configuration coordinate diagram showing the self-trapped exciton state.

can occur from the STE to the GS without emitting light. Note that this overlap is not at the lowest vibrational state of the STE state. Therefore, for the crossover to occur, higher vibrational states of the STE state have to occupied. In other words, the crossover needs heat energy to occur. Consequently, quenching due to crossover to the GS is a thermally activated process. At 0 K, only the lowest vibrational state is occupied, so no quenching from the STE state is expected to occur.

2.3.2 Semiconductor nanocrystals

If the dimensions of semiconductor crystals are reduced to the nanoscale, interesting new properties can arise. This happens at sizes where the size of the entire crystal is similar to the size of an exciton. In bulk semiconductor crystals, the excitons practically have an infinite amount of space, but at the nanoscale the excitons are confined. This induces size dependent properties. For example, the band gap of a semiconductor increases when the size of the crystal is reduced. In the nanocrystals of type II-VI semiconductor CdSe, the band gap can vary through the entire visible range of the light spectrum. Therefore, band edge emission from these nanocrystals results in colors spanning the entire rainbow depending on the size of the crystal, shown in **figure 2.8**.

These quantum confinement effects are commonly not significant in elpasolite SNC's [15], however there are other effects that are important at the nanoscale as well. Nanocrystals are smaller than the wavelength of light and therefore only experience Rayleigh scattering. This makes them suitable for application where light transparency is important. Due to their small size they can be suspended in solution as colloids, which is also shown in **figure 2.8**. Nanocrystals have a very high surface to volume ratio, which can be beneficial in catalytic application. However, this can be disadvantageous as a lot of defects are present at the surface of the crystals and a high surface to volume ratio is energetically unfavourable.

The synthesis of nanocrystals requires unconventional synthesis methods. The synthesis of the elpasolite nanocrystals is performed using the hot-injection method [27]. The hot-injection synthesis involves dissolving precursor salts in a high boiling point solvent with coordinating ligands. The salt ions form complexes with the ligands in the solution. These ion-ligand complexes are called monomers. Typically, a monomer solution is created which contains all of the ions of the crystal except one, to prevent spontaneous crystallization. At high temperatures, the final ion is of the desired crystal is injected into the reaction mixture,

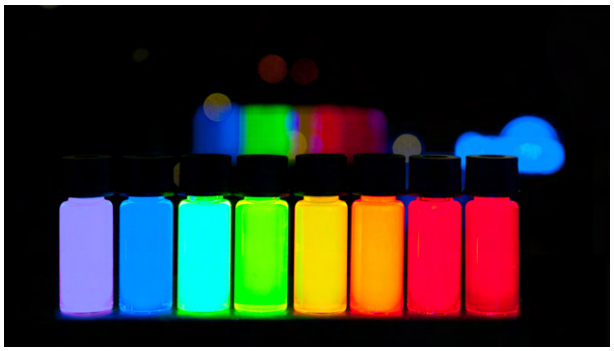

Figure 2.8: Photograph of colloidal CdSe quantum dots under UV light displaying various colors, dependent on their size. Photograph obtained from Wikipedia.

creating a supersaturated solution of the monomers. Then, the nucleation stage starts. Clusters of monomers form and these clusters grow by addition of monomers or by coalescence of two clusters, until small stable nuclei are formed which have wide size distributions. Then, the growth stage starts. In this stage the nuclei grow into nanocrystals and their size distribution becomes smaller. At this stage, the concentration of monomers has decreased. The nuclei grow by addition of monomers. Since the concentration of monomers has decreased, the growth becomes diffusion-limited. In this diffusion-limited regime, small nanoparticles grow faster than large nanoparticles, causing a size-focusing effect. This results in nanocrystals with a narrow size distribution. If the reaction is allowed to carry on, monomer concentrations become so low that smaller nanocrystals dissolve into solution again and larger nanocrystals keep growing, at the expense of smaller nanocrystals. This results in a broadening of the size distribution and is called Ostwald ripening or the defocusing regime. Ideally, the reaction is stopped before this moment.

The presence of coordinating ligands is of great importance. Without the ligands, the crystal growth is not inhibited. This would result in the formation of microcrystals. The ligands also increase the stability of the NC's. They bind to the surface which "passivates" the surface of the nanocrystals, reducing the amount of dangling bonds. The ligands typically contain long apolar chains, which makes the nanocrystals soluble in apolar solvent when they are capped with ligands.

The elpasolite structure consists of corner sharing metal-halide octahedra, stabilized by big cations in the cavities between the octahedra. The structural formula is $A_2^+B^+B'^{3+}X_6^-$. The structure is shown later in **figure 4.1 (c)**. An indication of the stability of perovskite crystals is given by the Goldschmidt tolerance factor and the cation/anion radius ratio (octahedral factor). The Goldschmidt tolerance factor is calculated by:

$$t = \frac{r_A + r_X}{\sqrt{2}(r_B + r_X)} \tag{2.1}$$

Where r_A is the ionic radius of the A cation, r_B is the ionic radius of the B cation, and r_X is the ionic radius of the X anion. The octahedral factor is given by:

$$\mu = \frac{r_B}{r_X} \tag{2.2}$$

For a structure to be theoretically stable, the value of the factors should be $0.75 < t < 1$ and $\mu > 0.41$. Since perovskite and elpasolites are so similar, these factors can also be used to probe the stability of elpasolite crystals [15]. Then, the value of the r_B cation is the individual values of both the B cations. These values should both have the correct value. Note that the factors only give an indication. Stable structures exist of which the values are not in the right range.

2.4 Lanthanide ions

2.4.1 Properties of lanthanides

The lanthanide elements are the group of elements with atomic number 57 to 71, often displayed in a row under the periodic table. Along the lanthanide series, the 4f orbitals are filled up. Lanthanides are most commonly found in the +3 oxidation state, in which they have the electronic configuration [Xe] $4f^n$, where n ranges from 0 for La^{3+} to 14 for Lu^{3+}. The lanthanides are chemically very similar and exhibit special electronic properties. These special electronic properties

give rise to unique luminescence among the lanthanides. This luminescence originates from intraconfigurational f-f electron transitions and are characteristic for each different lanthanide ion (except for La^{3+} and Lu^{3+}, due to their respectively empty and filled f-orbitals). The energy of the f-f transitions is only very weakly affected by the host material that the lanthanide ions are incorporated into, resulting in the same color of emission regardless of the host material. These properties make lanthanide phosphors very useful for various lighting applications.

A common method to make a lanthanide-based phosphor is to dope small amounts of lanthanide ion "impurities" into a host crystal. The lanthanide ions then replace the cations in the crystal. Because of the chemical similarity of the rare earth metals, it is common to dope luminescent lanthanides into a host material made up of non-luminescent rare earth ions, such as Y^{3+} or La^{3+}. For example, a commonly used commercial phosphors is YAG:Ce^{3+}. In this phosphor the host material is yttrium aluminium garnet (YAG, $Y_3Al_5O_{12}$). A small percentage of the Y^{3+} cations is substituted by Ce^{3+}, which gives rise to a broad yellow emission when excited by blue (and UV) light. YAG:Ce^{3+} is commonly used in combination with a blue LED to make a white light source [28, 29].

2.4.2 Considerations when doping lanthanides ions

While doping lanthanides into rare-earth based crystals works well, it is also possible to dope lanthanides into crystals which are not based on rare-earth cations. There are several considerations which have to be taken into account when doping lanthanides. The specific criteria are:

- The coordination number of the crystal site should be higher than 6
- The ionic radius of the crystal site cation should be similar
- The oxidation state of the crystal site ideally is equal

Lanthanides are hard Lewis acids and are therefore stabilized by large electron density. This means a high number of anions is preferred, such as in garnets and fluorides. As a general rule of thumb, cation sites with a coordination number of six or higher are necessary. Many attempts have been made to dope lanthanides into conventional semiconductors, but it has proven to be notoriously difficult, since the crystal sites have a low coordination number of 4 [30].

General considerations of doping any impurity into a host crystal is that the ion radius and the oxidation state of the dopant and crystal site should be similar. In order to incorporate dopants effectively, the size difference must not be too large between the dopant and the crystal site. Generally speaking, it is easier to incorporate a dopant if its ionic radius is slightly smaller than when it is slightly larger than the crystal site. If the dopant is too large or too small, incorporation becomes increasingly difficult and could lead to a reduction of the structural integrity. The oxidation state of the crystal site is also important. Ideally, the oxidation state of the crystal site and dopant should be equal, but a mismatch of oxidation state is also possible. However, it may be necessary to incorporate other ions for charge compensation or defects can form in the crystal [30].

When incorporating dopants into a crystal lattice, a shift in the diffraction angle of the reflection peaks can be seen. If the dopant has a different ionic radius than the ion it replaces in the lattice, it will change the lattice constants of the crystal. If the dopant is larger than the

crystal site, the diffraction angle of the reflection becomes smaller and vice versa, which can be derived from Bragg's law:

$$n\lambda = 2d \sin\theta \tag{2.3}$$

Where n is the diffraction order, λ is the wavelength of the x-rays, d is the lattice spacing and θ is the diffraction angle. We can see from Bragg's law that if the lattice spacing d gets smaller, the diffraction angle θ has to become larger to maintain the value of $n\lambda$. The shift in diffraction angle is a useful metric to verify whether dopants are incorporated into the crystal lattice.

2.4.3 Spectroscopy of lanthanide ions

The characteristic luminescence of the lanthanide ions originates from intraconfigurational f-f transitions, however some lanthanides also show luminescence from other electronic transitions. The spectroscopic properties of the trivalent lanthanides originate from three types of electronic transitions:

1. Charge transfer transitions

Charge transfer transitions are electronic transitions between a metal center and a surrounding ligand. In lanthanides, the most common charge transfer transition is ligand-to-metal charge transfer (LMCT). An electron from an orbital of a ligand is excited to an orbital of the metal. This transition is parity- and spin-allowed and consequently the absorption band is intense. Due to the -1 charge difference of the excited state, the bond strengths of the ground and excited state are significantly different. Therefore the bands of the states are offset in the configuration coordinate diagram and the transition has a broad absorption band. The energy of these transitions is usually very high (<250 nm), except for cations which are more easily reduced (Sm^{3+}, Eu^{3+}, Yb^{3+}, Tm^{3+}) [20]. In these cases the charge transfer transition can appear in the near-UV. It is worth noting that these transitions usually do not show luminescence themselves, but f-f transition can be excited through the charge transfer absorption band. Though, charge transfer luminescence is possible in rare cases [31].

2. 4f-5d transitions

4f-5d transitions are electron transitions from the (partially) filled 4f orbital to the empty 5d orbital. These transitions are fully allowed and have intense absorption bands. The $4f_{n-1}$ $5d_1$ excited state has an electron in the 5d orbital which significantly contributes to bonding and therefore the transition also has a broad band. The location of the d-orbitals is strongly dependent on the crystal environment due to crystal field splitting and therefore differs strongly in energy depending on the host lattice. The transitions have high energy gaps and only those of Ce^{3+}, Pr^{3+} and Tb^{3+} can occur in the near-UV. In some cases these transitions can show luminescence, specifically Ce^{3+}.

3. f-f transitions

f-f transitions are intraconfigurational transitions between the 4f orbitals. These transitions involve a rearrangements of the electrons in the 4f orbitals. The transitions are between the same orbitals, so they are parity forbidden. Also, they often require a spin flip, making them spin forbidden as well. As a result these transitions have a low probability of occurring and have very weak absorption. The 4f-orbitals are very compact and therefore they are shielded from the crystal environment by the 5s- and 5p-orbitals. This shielding effect causes the contribution of the 4f-orbitals to bonding to be very minimal. Because of this, the energy levels of the f-f

transitions is affected very little by the crystal environment. Since the energy of the transitions is almost independent of crystal environment, it is possible to construct a diagram which maps the locations of the energy levels, regardless of the host. This diagram is called the Dieke diagram and is shown in **figure 2.10**. Due to the shielding of the f-orbitals, the difference in bonding between the ground and excited state is also negligible. Therefore the bands are aligned in the configuration coordinate diagram. This causes very sharp absorption and emission lines, as well as almost no Stokes shift. These factors give rise to the characteristics of lanthanide luminescence: sharp absorption and emission lines with a very small Stokes shift, (almost) independent of crystal environment. The lanthanide luminescence of the materials discussed in this thesis originate from f-f transitions, so this will be discussed in further detail.

f-f transitions

To give a better understanding of how the f-f transitions lead to characteristic emission, the energy levels of the trivalent lanthanides will be further explained. The different energy levels arise from different electron configurations in the f-orbitals. Due to coulomb interaction between electrons, the energies of the various electron configurations are different. This results in a splitting of the 4f state into multiple terms. These terms are subsequently split into energy levels by spin-orbit coupling. These energy levels are described with term symbols. Term symbols give an abbreviated description of angular momentum quantum numbers (S, L and J), which is useful in spectroscopy. A term symbol has the form:

$$^{2S+1}L_J \tag{2.4}$$

Where S is the total spin quantum number and $2S+1$ is the spin multiplicity term. L is the total orbital momentum quantum number. J is the total angular momentum quantum number.

The total spin quantum number S is obtained by adding all the spin quantum numbers (m_s) in the different orbitals of the subshell, which have a value of $+\frac{1}{2}$ or $-\frac{1}{2}$. The total orbital momentum quantum number L is obtained by adding the orbital momentum quantum numbers (m_l). In spectroscopic notation, L is represented by letters where 0 = S, 1 = P, 2 = D, 3 = F and 4 = G (continued alphabetically). m_l can have several values depending on the subshell. The values of the total angular momentum quantum number J is calculated with the formulas $J_{max} = L + S$ and $J_{min} = |L - S|$. The values of J range from J_{min} to J_{max} with steps of 1 ($J = J_{min}, J_{min}+1, J_{min}+2, ..., J_{max}$).

Let us consider the Pr^{3+} ion. It has the electron configuration [Xe] $4f^2$. Pr^{3+} is used for sake of simplicity as it is the simplest case of the trivalent lanthanide which has electron-electron interactions, with just two electrons. Table 2.1 shows a box diagram of the ground state electron configuration of Pr^{3+}. There are two electrons, both with spin up ($m_s = +\frac{1}{2}$) in the orbitals with orbital quantum number $m_l = 3, 2$. Adding the spins and orbital quantum numbers and using the formulas for spin multiplicity gives us S = 3 and L = 5, which corresponds to H in spectroscopic notation.

Pr^{3+}		m_l						
		3	2	1	0	-1	-2	-2
m_s	$+\frac{1}{2}$	↑	↑					
	$-\frac{1}{2}$							

Table 2.1: The ground state configuration of Pr^{3+}. Total spin quantum number is $S = (+\frac{1}{2}) + (+\frac{1}{2}) = 1$, spin multiplicity is $2S + 1 = 2 * 1 + 1 = 3$. The total orbital angular momentum is $L = 3 + 2 = 5$, which is "H" in spectroscopic notation. So the term symbol is ^{3}H.

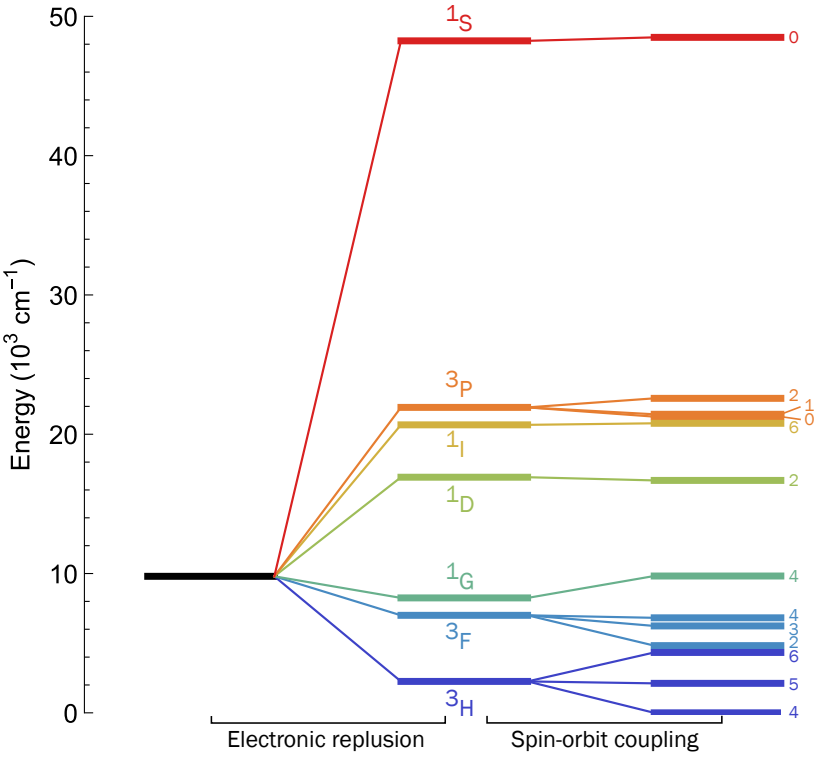

Figure 2.9: The splitting of the 4f energy levels. The energies of the $4f^2$ electron configuration of Pr^{3+} is split into 7 terms by electron repulsion due to coulomb interaction. The terms are further split into energy levels by spin-orbit coupling. These interactions give rise to a separation of almost 50000 cm^{-1} between the ground state $^3H_4$ and the most energetic electron configuration $^1S_0$.

So the ground state term symbol is ^{3}H. This
term can be split into energy levels with different values of J: $J_{min} = |5-1| = 4$ and $J_{max} = |5+1| = 6$, so the values of J are $J = 4, 5, 6$. This gives us the three lowest energy levels of Pr^{3+}: $^3H_4$, $^3H_5$ and $^3H_6$.

Every electron configuration can be assigned a term symbol, which all correspond to different energies. This way the $4f^2$ electron configuration of Pr^{3+} is split into 7 different terms by coulomb interaction, which are subsequently split into a total of 14 energy levels by spin-orbit coupling. This is shown in **figure 2.9**. The values of these energy levels can be calculated and have close resemblance to experimental values [32]. As discussed earlier, the value of the energy levels are only very slightly affected by the host material, so it is possible to map all these energy levels in a universal diagram, called the Dieke diagram, shown in **figure 2.10** [33]. This diagram gives the experimental values of the energy levels of all the lanthanides. Note that the values of the energy levels in **figure 2.9** match up with the values in the Dieke diagram for Pr^{3+}.

Now that term symbols and the energy level splitting have been discussed, we can understand the Dieke diagram and use it. Electronic transitions can be drawn in the Dieke diagram (**fig. 2.10**) as vertical arrows. The energy difference between the energy levels gives the energy of the transition. For example, a transition from the $^5D_0$ level to the $^7F_2$ level of Eu^{3+} gives a energy difference of about 16200 cm^{-1}, which corresponds to a photon with a wavelength of 617 nm. This transition therefore emits a red photon. This transition is the one responsible for the characteristic red luminescence of Eu^{3+}. The transition responsible for the green emission of Tb^{3+} is the $^5D_4 \longrightarrow {}^7F_5$ transition. This transition has an energy of around 18200 cm^{-1}, which corresponds to 549 nm or green light. If the energy difference is small between energy levels, the system can non-radiatively decay through multi-phonon relaxation. Therefore, the most intense emission transitions occur from the states which have large energy gap to the next state lower in energy ($^5D_0$ for Eu^{3+} and $^5D_4$ for Tb^{3+}).

We discussed briefly that the f-f transitions are spin an parity forbidden. This causes them to

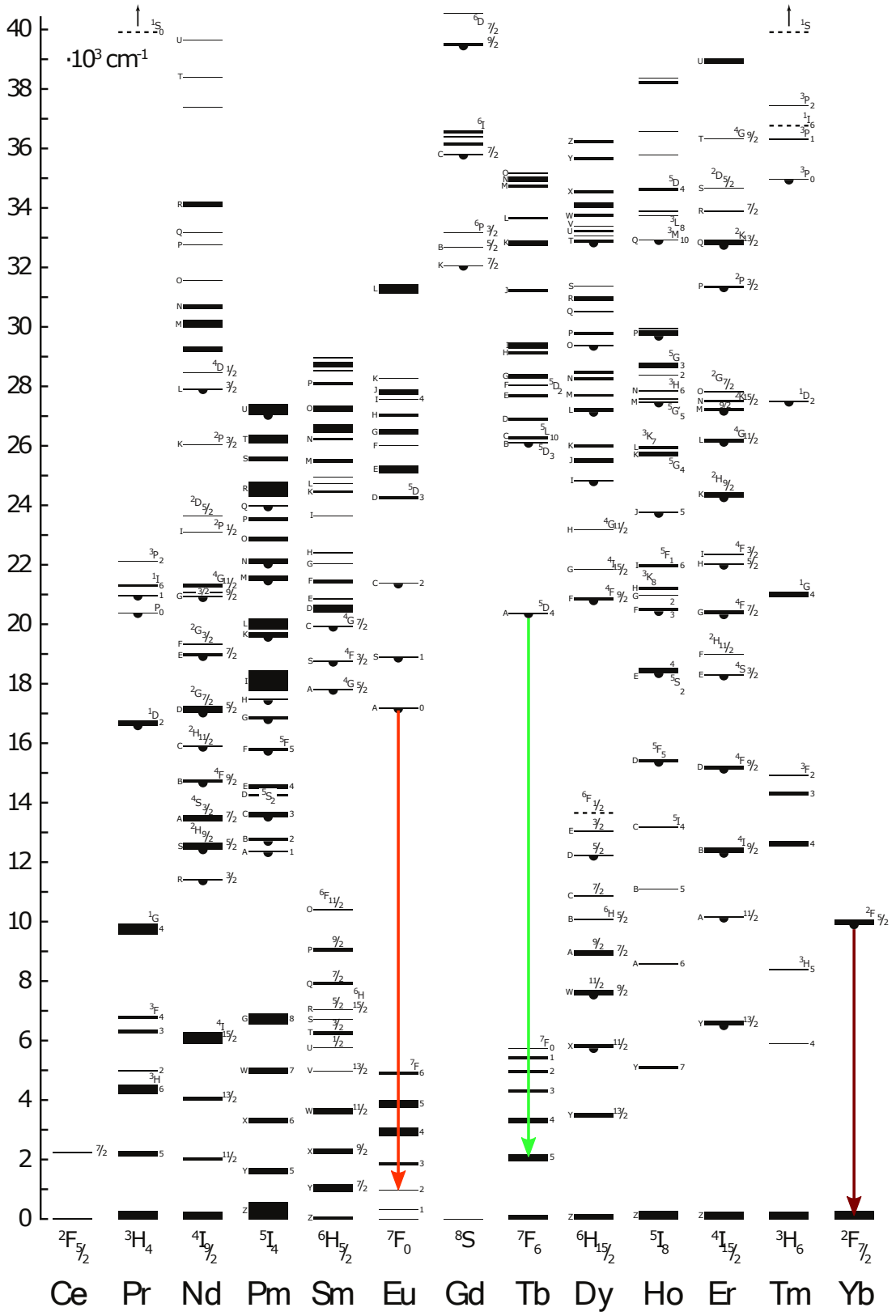

Figure 2.10: The Dieke diagram. Observed experimental values of the energy levels of the trivalent lanthanides. Red arrow: $^5D_0 \longrightarrow {}^7F_2$ transition of Eu^{3+}, responsible for its red luminescence. Green arrow: $^5D_4 \longrightarrow {}^7F_5$ transition of Tb^{3+}, responsible for its green luminescence. Dark red arrow: $^2F_{\frac{5}{2}} \longrightarrow {}^2F_{\frac{7}{2}}$ transition of Yb^{3+}, responsible for its near infra-red emission.

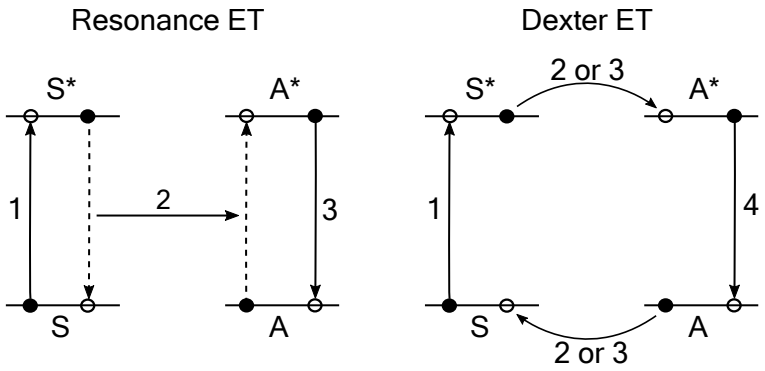

Figure 2.11: Schematic figure showing resonance energy transfer (left) and Dexter energy transfer (right).

have very weak absorption. To efficiently convert incoming light in practical applications, their absorption is too weak. A method to increase the absorption of a lanthanide phosphors, is to use a sensitizer. A sensitizer absorbs light and subsequently excites a luminescent ion through the process of energy transfer. The sensitizer is often a luminescent ion which absorbs light through intense allowed transitions. However, in our case the sensitizer is the semiconductor host material.

The process of energy transfer can be divided into two categories:

- Energy transfer through dipole-dipole resonance coupling, called Förster Resonance Energy Transfer (FRET)
- Energy transfer through electron exchange interaction, called Dexter energy transfer

The processes are schematically shown in **figure 2.11**. Förster resonance energy transfer is a process which occurs when a sensitizer ion and an activator ion are in close proximity to each other. When the sensitizer ion is in the excited state, it can transfer its energy (not its electron) to an activator ion via dipole-dipole resonance interaction. The strength of this interaction is very strongly dependent on the distance ($1/r^6$) between sensitizer and activator and the energy transfer typically occurs over distances less than 10 nm. In Dexter energy transfer, the sensitizer transfers its energy by electron exchange interaction. The sensitizer and activator exchange electrons which excites the activator ion and returns the sensitizer to the ground state. This type of energy transfer requires wavefunction overlap between the sensitizer and activator and therefore occurs over extremely short distances (<5 Å). In semiconductors, energy transfer often occurs through electron exchange. This is because the electrons (and holes) are delocalized over the material. The delocalization effectively means that the wavefunction of the excited state spans over a very large region in the material. Therefore, wavefunction overlap with the activator ion is easily achieved. Effectively, the sensitizer in **figure 2.11** is not a localized state in the material, the entire material *is* the sensitizer.

The luminescence of lanthanide ions can be quenched in different ways. In the context of our research, the most relevant quenching mechanisms are concentration quenching and charge transfer quenching. Concentration quenching is somewhat related to energy transfer. It is the result of a too high concentration of dopants. When the dopant concentration is too high, the dopants are in close proximity to each other. The excited dopant can transfer its energy to other dopants in the vicinity. At high concentration, a network is formed in which the excited state

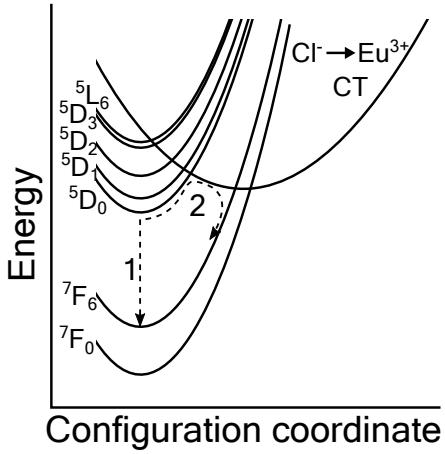

Figure 2.12: Configuration coordinate diagram showing the quenching of Eu^{3+} via the charge transfer state. Arrow 1 indicates emission. Arrow 2 indicates charge transfer quenching.

travel through the material. Like in semiconductors, the traveling excited state state can then diffuse to defects and lose its energy to defects, quenching the emission.

Quenching of trivalent lanthanides in solids mainly occur by charge transfer quenching [34]. In charge transfer quenching, the excited state of the lanthanide is quenched via a charge transfer state. For illustration, an example of charge transfer of Eu^{3+} is shown in the configuration coordinate diagram in **figure 2.12**. The figure shows the ^7F (middle states are not shown for simplicity) and the ^5D states. There is a broad offset band which corresponds to the $Cl^- \longrightarrow Eu^{3+}$ charge transfer state. This state is significantly offset, due to the strong change in bond strengths when Eu^{3+} is reduced to Eu^{2+}, which is essentially what happens when charge transfer occurs from Cl^- to Eu^{3+}. When Eu^{3+} is in the excited ^5D energy levels, thermal crossover can occur to the charge transfer state. From the charge transfer state, thermal crossover can occur to one of the ^7F states. As a result the ^5D state non-radiatively transitions to the ^7F state. Since the quenching occurs through thermal crossover, charge transfer is a thermally activated process.

The nature and position of the charge transfer band depends on the host material and the lanthanide. As discussed earlier, not all lanthanides are easily reduced to the (II) oxidation state. Some lanthanides can be oxidized to the (IV) oxidation state, which gives rise to other charge transfer bands. In semiconductors, electrons and holes are rather freely available and this gives rise to more complex behaviour of lanthanide charge transfer bands. Traditionally, charge transfer transitions are represented by a transitions from the orbital of one ion to the orbital of another ion, such as from $Cl^- \longrightarrow Eu^{3+}$. However, this suggests that the transition occurs from an orbital which is completely Cl^- in character, to an orbital which is completely Eu^{3+} in character. Though in semiconductors, the orbitals are heavily mixed. Therefore, a charge transfer transition from a Cl^- ion in a semiconductor crystal to Eu^- is not a transition from a pure Cl^- orbital, but is a combination of orbitals. The transitions is also not a transition from a localized Cl^--orbital, but from a delocalized orbital. Consequently, a charge transfer transition to Eu^{3+} can be represented as a transition of an electron in the valence band to a Eu^{3+} center, leaving behind a hole in the valence band [35]. The position of this charge transfer band is dependent on the position of the Eu^{2+} state within the band gap of a material, which Dorenbos has extensively studied in many host materials[35–38]. If the Eu^{3+} level is located very low

within the band gap, the charge transfer band will be at low energies. This results in increased charge transfer quenching as the CT state in **figure 2.12** will be located lower, resulting in increased crossover to the CT state and subsequently the GS.

Chapter 3

Experimental methods

3.1 Chemicals

Cesium carbonate (Cs_2CO_3, 99.9%), Silver acetate (CH_3COOAg, 99%), Bismuth (III) acetate ($(CH_3CO_2)_3Bi$, 99.99%), Sodium acetate (CH_3COONa, 99%), Indium (III) acetate ($(CH_3CO_2)_3In$, 99.99%), Europium (III) acetate hydrate ($(CH_3CO_2)_3Eu \cdot xH_2O$, 99.9%), Ytterbium (III) acetate hydrate ($(CH_3CO_2)_3Yb \cdot xH_2O$, 99.95%), Terbium (III) acetate hydrate ($(CH_3CO_2)_3Tb \cdot xH_2O$, 99.9%), Cesium chloride (CsCl, 99.9%), Sodium chloride (NaCl, 99.5%), Indium (III) chloride ($InCl_3$, 99.999%), Cesium bromide (CsBr, 99.9%), Bismuth (III) chloride ($BiCl_3$, 98%), Terbium (III) chloride hexahydrate ($TbCl_3 \cdot 6\,H_2O$, 99.9%), Europium (III) chloride hexahydrate ($EuCl_3 \cdot 6\,H_2O$, 99.99%), Ytterbium (III) chloride hexahydrate ($YbCl_3 \cdot 6\,H_2O$, 99.99%, Strem Chemicals), Bismuth oxide (Bi_2O_3, 99.5%, Baker Reagents), Europium (III) oxide (Eu_2O_3, 99.995%, Highways International), Silver nitrate ($AgNO_3$, 99%), Acetonitrile (99.8%, anhydrous), Ethyl acetate (99.8%, anhydrous), Toluene (99.8%, anhydrous), Ethanol (99.8%, absolute, VWR chemicals), Trimethylsilyl chloride (TMS-Cl, $(CH_3)_3SiCl$, 99%), Trimethylsilyl bromide (TMS-Br, $(CH_3)_3SiBr$, 97%), Oleylamine (OLAM, 98%), 1-Octadecene (ODE, technical grade, 90%), Oleic acid (OA, 90%), Hydrochloric acid (HCl, analytic grade, 37%), Hydrobromic acid (HBr, 48%), Nitric acid (HNO_3, analytic grade, 65%), were all purchased from Sigma Aldrich, unless stated otherwise. All chemicals were generally used without further purification. Cases where purification steps were performed are mentioned in the experimental procedures.

3.2 Synthesis procedures

Reactions under inert atmosphere were performed using Shlenkline techniques with nitrogen as inert gas. Centrifuging was performed with a Rotina 380 centrifuge. Solid state reactions were performed in a Carbolite box oven. Samples were stored under dry nitrogen atmosphere in gloveboxes.

3.2.1 Cs_2AgBiX_6 (X = Cl, Br) and $Cs_2NaBiBr_6$ nanocrystals

The Cs_2AgBiX_6 (X = Cl, Br) and $Cs_2NaBiBr_6$ nanocrystals were synthesized using the hot injection method based on the publication of Creutz *et al.* [39]. Cs_2CO_3 (0.355 mmol), CH_3COOAg (0.5 mmol) or CH_3COONa (0.5 mmol), $(CH_3CO_2)_3Bi$ (0.5 mmol), OLAM (0.5 g), OA (2.5 g) and

ODE (10 mL) were added to a 50 mL 3-necked roundbottom flask. The solution was heated to 110 °C under vacuum with magnetic stirring. The reaction was degassed for 45 minutes under vacuum. During degassing, the solution turned from colorless to yellow to dark brown (Cs_2AgBiX_6) or colorless to yellow ($Cs_2NaBiBr_6$). Then, the temperature was increased to 145 °C under nitrogen atmosphere and TMS-Cl (0.34 mL) or TMS-Br (0.34 mL) was swiftly injected into the reaction mixture under vigorous stirring. Gray precipitate immediately formed. After 15 seconds, the reaction vessel was submerged in an ice-water bath to quench the reaction. When the reaction was cooled to room temperature, the mixture was transferred to a plastic conical tube (eppendorf, 25 mL) and centrifuged for 10 minutes at 4000 rpm (RCF = 3112 g). The dark brown (Cs_2AgBiX_6) or yellow ($Cs_2NaBiBr_6$) supernatant was thoroughly drained and the off-white/gray precipitate was dispersed in toluene (5 mL) with sonication (10 minutes). The solution was centrifuged for 10 minutes at 4000 rpm (RCF = 3112 g). The yellow ($Cs_2AgBiCl_6$ and $Cs_2NaBiCl_6$) or orange ($Cs_2AgBiBr_6$) supernatant containing the nanocrystals was collected for further characterization.

The same procedure was used for the Yb^{3+}-, Eu^{3+}- and Tb^{3+}-doped nanocrystals with a single modification. The dopant precursors $(CH_3CO_2)_3Yb \cdot xH_2O$, $(CH_3CO_2)_3Eu \cdot xH_2O$ or $(CH_3CO_2)_3Tb \cdot xH_2O$ were simply added to the start of the reaction with proportions relative to $(CH_3CO_2)_3Bi$. For example, to a reaction for 5% Eu^{3+} doping, 0.5 mmol of $(CH_3CO_2)_3Bi$ and 0.025 mmol $(CH_3CO_2)_3Eu \cdot xH_2O$ was added. Doping concentrations are represented as a percentage of Bi(III) substituted ($doping\% = [Ln]/([Ln] + [Bi])$).

Any washing steps were performed by adding ethyl acetate or acetonitrile to the nanocrystal solution in equal volume amount to the nanocrystal solution, followed by centrifuging 5 minutes at 3000 rpm (RCF = 1750 g) and discarding the supernatant. The nanocrystal precipitate was redispersed in toluene. If the precipitate did not fully dissolve, another centrifuging step was performed and the supernatant was collected.

3.2.2 $Cs_2NaBi_xEu_{1-x}Cl_6$ (x = 0, 0.25, 0.5, 0.75, 1) microcrystals

The series of $Cs_2NaBi_xEu_{1-x}Cl_6$ (X = 0, 0.25, 0.5, 0.75, 1) microcrystals were synthesized using preparation E of Morss *et al.* [40]. CsCl (2 mmol), NaCl (1 mmol), Eu_2O_3 (amount see table 3.1) and Bi_2O_3 (amount see table 3.1) were dissolved in about 10 mL concentrated hydrochloric acid (37%) in a 50 mL beaker with magnetic stirring and heating. When fully dissolved, the magnetic

Crystal:	Bi_2O_3 added: (mmol)	Eu_2O_3 added: (mmol)
$Cs_2NaBiCl_6$	0.5	0
$Cs_2NaBi_{0.75}Eu_{0.25}Cl_6$	0.375	0.125
$Cs_2NaBi_{0.5}Eu_{0.5}Cl_6$	0.25	0.25
$Cs_2NaBi_{0.25}Eu_{0.75}Cl_6$	0.125	0.375
$Cs_2NaEuCl_6$	0	0.5

Table 3.1: Amount of reagents Bi_2O_3 and Eu_2O_3 used for the $Cs_2NaBi_xEu_{1-x}Cl_6$ (x = 0, 0.25, 0.5, 0.75, 1) microcrystals series.

stirrer was removed and the solution was heated to 80-90 °C to slowly evaporate to dryness. Due to excessive HCl gas formation, working in a fumehood was paramount. As the solution volume decreased, white transparent crystals formed. When the solution was close to dryness, the beaker was transferred to a drying oven (100 °C) for 2 hours to fully evaporate residual liquids. The white table salt-like crystals were washed three times with absolute ethanol and subsequently dried in a drying oven (100 °C) for 1 hour. Due to their hygroscopic nature, the crystals were stored under dry nitrogen atmosphere in a glovebox.

3.2.3 $Cs_2AgInCl_6$

The 10% Eu^{3+}-doped $Cs_2AgInCl_6$ microcrystals were synthesized using a modified procedure based on Volonakis *et al.* [41]. $In(CH_3CO_2)_3$ (0.90 mmol), Eu_2O_3 (0.05 mmol) and $AgNO_3$ (1 mmol) were dissolved in 10 mL 37% HCl in a 50 mL beaker with heating. While hot, CsCl (2 mmol) was added to the beaker. White precipitate immediately formed. The reaction was left at 100-110 °C for about 30 minutes while stirring. The contents of the beaker were vacuum filtered. The residue was washed with absolute ethanol three times and subsequently dried in a drying oven at 100 °C for several hours.

3.2.4 Cs_3InCl_6

The Cs_3InCl_6 microcrystals were synthesized using preparation X of Morss *et al.* [40] and by solid state reaction in an evacuated quartz tube [42]. Following preparation X of Morss *et al.* [40]: CsCl (3 mmol) and $(CH_3CO_2)_3In$ (1 mmol) were dissolved in 10 mL HCl (20 wt% aqueous) in a 50 mL beaker. The solution was heated and stirred to dissolve. When dissolved, the magnetic stirrer was removed and the solution was mildly heated to slowly evaporate until slight precipitate formed. Then heating was turned off and a watch glass was placed on the beaker. Gradual cooling lead to formation of white transparent crystals. After cooling to room temperature, the beaker was transferred to a freezer (T = -20 °C) to promote further crystallization. The crystals were filtered with vacuum filtration and the residue was collected and washed three times with absolute ethanol and subsequently dried in a drying oven at 100 °C for several hours.

For a phase pure product solid state reaction was performed in an evacuated quartz tube. Prior to the reaction, CsCl and CsBr were thoroughly dried overnight in a drying oven at 100 °C. In a dry nitrogen filled glovebox, CsCl (3 mmol) and $InCl_3$ (1 mmol for Cs_3InCl_6, 2 mmol for $Cs_3In_2Cl_9$) were added to a quartz ampoule. The ampoule was connected to a piece of hosing connected to an airtight glass valve. The valve was closed and the closed system was removed from the glovebox and attached to a vacuum pump. The valve was opened under vacuum and the tube was evacuated to $6 * 10^{-2}$ mbar pressure. Then, the valve was closed and the evacuated system was detached from the vacuum pump. The evacuated quartz ampoule was sealed using an oxy-hydrogen torch to obtain a small closed evacuated ampoule filled with precursors. The ampoule was heated to 750 °C in a box oven (ramp rate 10 °C min^{-1}) and held at this temperature for 30 minutes to fully melt the contents. Then the ampoule was cooled to room temperature in the oven under natural cooling. The white crystals were collected by cutting open the ampoule and grinding the contents in an agate mortar. The product was stored in a glovebox.

For both synthesis procedures, doping with Yb^{3+}, Eu^{3+} and Tb^{3+} was performed by partially substituting $InCl_3$ with $YbCl_3$, $EuCl_3$ or $TbCl_3$ for the desired doping amount. For example, 5%

Eu^{3+} doping was performed by using 0.95 mmol $InCl_3$ and 0.05 mmol $EuCl_3$ instead of 1 mmol $InCl_3$. The dry lanthanide chlorides were obtained by dehydrating the $LnCl_3 \cdot 6\,H_2O$ precursors by gradual heating to 220 °C under a vacuum. Heating should occur slowly (5 °C min^{-1}) as oxychlorides of the lanthanides may form under strong heating [43, 44].

For the partial substitution of Cl by Br ($Cs_3InCl_3Br_3$), solid state reaction was performed in an evacuated quartz tube as well. The exact same procedure was used with the single modification that CsCl (3 mmol) was replaced by CsBr (3 mmol).

3.3 Characterization

3.3.1 Structural characterization

Identification of the crystal phase of the materials was done by powder x-ray diffraction. Measurements of $Cs_2AgBiCl_6$ nanocrystals and $Cs_2NaBi_xEu_{1-x}Cl_6$ (x = 0, 0.25, 0.5, 0.75, 1) microcrystals were performed on a Philips PW1820 diffractometer with a Philips PW1729 x-ray generator with Cu K_α radiation at 40 kV and 20 mA. The rest of the measurements were performed on a Panalytical Aeris diffractometer with Cu K_α radiation at 40 kV. Measurements on microcrystals were performed with finely ground samples. Measurements of nanocrystals were performed by dropcasting the nanocrystal on a low background (100) silicon plate followed by evaporation to form a film of nanocrystals. Reference XRD patterns were calculated with the VESTA software [45] using crystal data from crystallography.net [46] or the materials project [47].

TEM images were obtained using a FEI TECNAI T12, operating at 120 kV. The TEM samples were made by dropping 30 μL of nanocrystal solution (300x dilution of the product solution) on carbon coated copper TEM grids.

For the elemental analysis of the Yb^{3+}-doped $Cs_2AgBiBr_6$ series, inductively coupled plasma optical emission spectroscopy (ICP-OES) measurements were performed on a Perkin Elmer inductively coupled plasma-optical emission spectrometer. All samples used for ICP-OES were washed once with acetonitrile. The sample solutions were obtained by first evaporating the solvent of the nanocrystal solutions. Then, the dry nanocrystals were dissolved and diluted in 5% nitric acid with sonication.

3.3.2 Optical characterization

Samples for optical characterization were prepared by 300 times dilution of the nanocrystal stock solution in toluene in a 10x10 mm quartz cuvet. Absorption spectra were measured on a Perkin Elmer Lambda 950 UV/VIS/IR spectrometer. Photoluminescence emission and excitation spectra were measured on an Edinburgh Instruments FS920 spectrometer with a 450 W xenon light source. Visible light spectra were measured on a Hamamatsu R928 photomultiplier tube and infra-red spectra were measured on a liquid-nitrogen cooled Hamamatsu R5509 photomultiplier tube. Room temperature PL decay measurements were performed using a Edinburgh EPL375 pulsed diode laser with pulse period 200 ns and excitation wavelength 375 nm with a Hamamatsu H74422-40 photomultiplier tube. Temperature dependent PL decay were measured using an Obis LX 375 nm laser module operated with a pulse generator with varying pulse widths and repetition rates.

3.3.3 Low temperature measurements

Low temperature measurements up to liquid nitrogen temperatures were performed using a Linkam THMS600 stage placed in the Edinburgh Instruments FS920 spectrometer. Nanocrystal samples were prepared by dropcasting the nanocrystal solution into the sample holder. Microcrystal samples were prepared by pressing the finely ground microcrystals in the sample holder with a quartz glass cover. Measurements at liquid helium temperatures were performed using an Oxford Instruments liquid helium flow cryostat. For the liquid helium temperature PL measurements, the 300 times diluted nanocrystal solution was loaded into a sealed quartz cuvette.

Chapter 4

Results and discussion

In this chapter, the results of our research are presented. We investigate various materials for their potential to incorporate lanthanides. The chapter is divided into two sections: Bismuth-based elpasolite materials and indium-based elpasolite materials. The general properties of the materials are discussed followed by a detailed discussion of the structural characterization and photoluminescence properties of the individual materials.

4.1 Bismuth-based elpasolite materials

We study the properties of several bismuth-based elpasolite materials to investigate their potential for lanthanide incorporation. The crystals discussed in this section have the chemical composition $A_2^+B^+B'^{3+}X_6^-$. They crystallize in the elpasolite structure (shown in **fig. 4.1 (c)**) with space group $Fm\bar{3}m$. The stability of the crystal structure depends on the composition of the crystal. It can be estimated if a structure is stable using the Goldschmidt tolerance factor and the octahedral factor (section 2.3). To maintain the cubic elpasolite structure it is beneficial

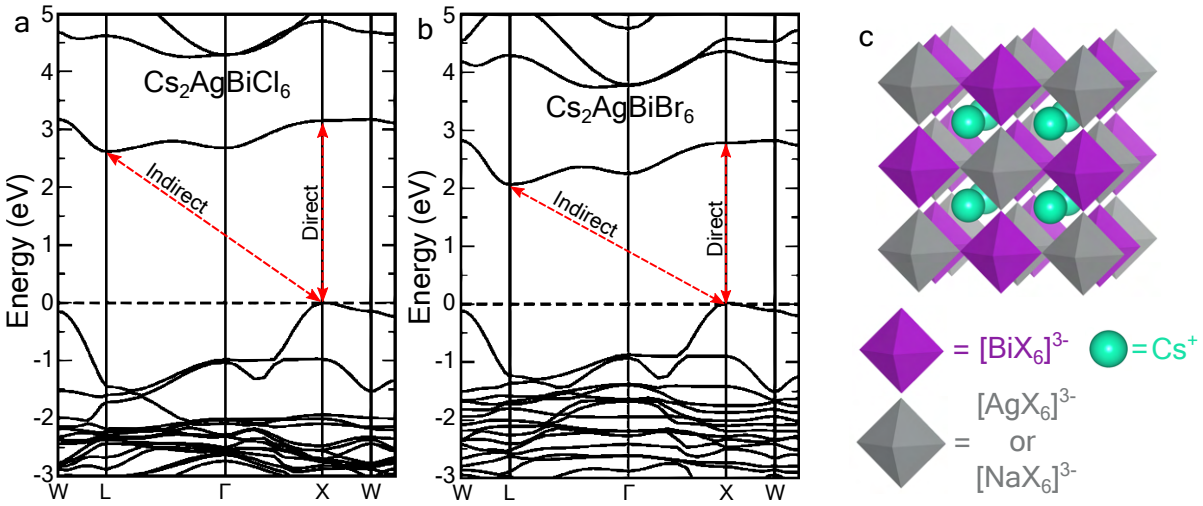

Figure 4.1: The band structure of $Cs_2AgBiCl_6$ **(a)** and $Cs_2AgBiBr_6$ **(b)** [14], red arrows indicate the band-to-band electronic transitions. **(c)** The elpasolite structure, consisting of alternating corner-sharing $AgCl_6$ and $BiCl_6$ octahedra, stabilized by large Cs^+ cations in the cavities between the octahedra.

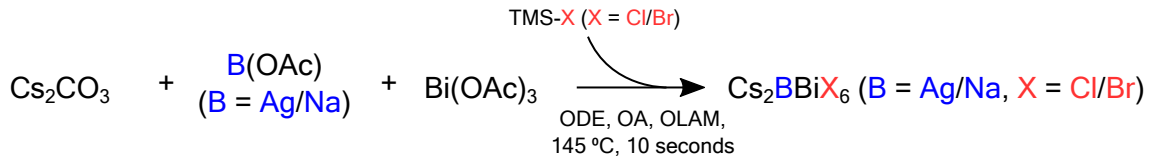

Figure 4.2: Synthesis of the bismuth-based nanocrystals. Metal acetate/carbonate salts are dissolved into octadecene using oleic acid and oleylamine as ligands. The solution is degassed for one hour at 110 °C. After this, the reaction is heated to 145 °C under N_2 atmosphere and TMS-Cl is swiftly injected to initiate nucleation. After 10 seconds the reaction is quenched by submerging the reaction vessel in an ice-water bath.

to have as large as possible A cations. Since Cs^+ is the largest inorganic cation, it is usually the cation of choice. The fact that Cs^+ is the largest inorganic cation presents a limit on how large the other ions in the crystal can be. The limiting factor for stability is usually the halide anion: chlorides are usually stable, bromides often encounter stability issues and few cases of stable iodides are known [15].

The band structure of the elpasolites $Cs_2AgBiCl_6$ and $Cs_2AgBiBr_6$ are shown in **figure 4.1 (a,b)**. Generally, the valence band maximum of the bismuth-based elpasolite semiconductors are made up of bismuth 6s- and halide p-orbitals and depending on the B^+ cation can also have contribution of this cation. The conduction band minimum is made up of bismuth 6p-orbitals. The bismuth elpasolite materials commonly have an indirect band-gap characterized by a slow onset of the absorption band. However at higher energy, direct transitions with very strong absorption are observed. These direct band-to-band transitions result in extremely high absorption. The electronic properties of the material can be tweaked by substituting the B^+ cations and X^- halide anions. This way, we can tune the absorption and PL characteristics. In this section, the B^+ cations Na^+ and Ag^+ are investigated and the X^- anions Cl^- and Br^- are investigated.

The synthesis used for the bismuth-based nanocrystals is based on a publication by Creutz *et al.* [39]. A schematic is shown in **figure 4.2**. A more detailed description of the synthesis is provided in experimental methods (section 3.2.1). For all bismuth-based elpasolite nanocrystals this synthesis was used, adapting for the required ions for the crystal. Washing steps with ethyl acetate and acetonitrile were investigated for some of the syntheses.

4.1.1 $Cs_2AgBiCl_6$ nanocrystals

The synthesis used for the $Cs_2AgBiCl_6$ nanocrystals is based on a publication by Creutz *et al.* [39], discussed earlier. The obtained product was characterized as synthesized and no washing steps were performed.

To investigate the structural properties of the synthesized $Cs_2AgBiCl_6$ nanocrystals, X-ray diffraction (XRD) and transmission electron microscopy (TEM) measurements were performed. **Figure 4.3** presents the structural analysis data of the nanocrystals. **Figure 4.3 (a)** shows the experimental measurement (top) and a calculated diffractogram (bottom). The experimental measurement shows close resemblance to the calculated diffractogram, though the peaks are broadened. The broadened peaks are the result of Scherrer broadening, typical for nanocrystals. Peaks in a diffractogram originate from constructive interference of x-ray reflections. In micro-crystals, the number of reflection planes is extremely large, resulting in very sharp lines due to

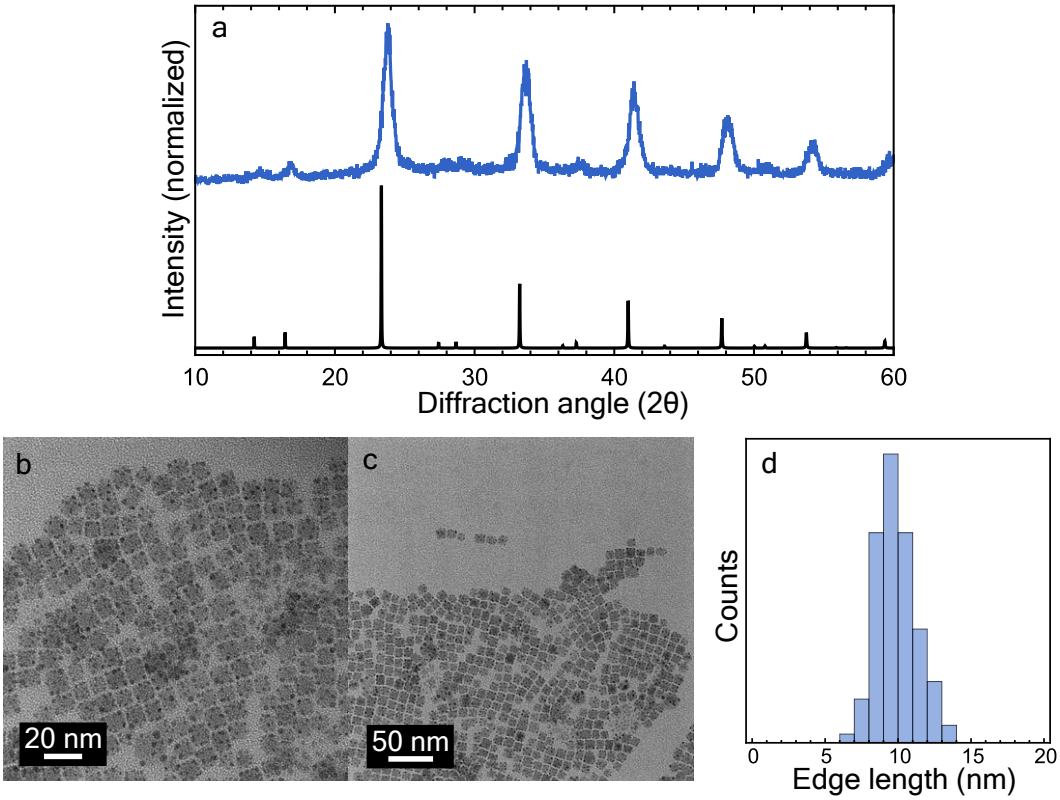

Figure 4.3: Structural data for $Cs_2AgBiCl_6$ nanocrystals. **(a)** X-ray diffractogram of $Cs_2AgBiCl_6$ nanocrystals (top) and calculated reference diffractogram (bottom). **(b,c)** TEM images of the synthesized $Cs_2AgBiCl_6$ nanocrystals and **(d)** corresponding size histogram of the nanocrystals. The edge lengths of the nanocrystals range from 6.8 to 13.7 nm and have an average of 9.9 nm.

very strong interference. In nanocrystals, the number of reflection planes in a single crystal is relatively small, so there is less constructive interference, resulting in broader reflection peaks with lower intensities.

Figure 4.3 (b,c) show TEM images of synthesized nanocrystals. The images show monodisperse cubic nanocrystals with small black dots. The histogram (**fig. 4.3 (d)**) shows the nanocrystals have edge lengths ranging from 6.8 to 13.7 nm with an average of 9.9 nm. The black dots on the nanocrystals have been investigated in various publications and are assigned to small Ag^0 clusters, formed through the reduction of Ag^+ by oleylamine [48]. We will disregard these clusters in this work as they do not seem to be detrimental to the properties of the nanocrystals. Regardless, the structural data confirms that the product of our synthesis has the elpasolite crystal structure are phase pure cubic $Cs_2AgBiCl_6$ nanocrystals.

To investigate the optical properties of the synthesized $Cs_2AgBiCl_6$ nanocrystals, we performed absorption, photoluminescence (PL) and photoluminescence excitation (PLE) measurements. **Figure 4.4** presents the optical data of the synthesized $Cs_2AgBiCl_6$ nanocrystals. **Figure 4.4 (a)** shows the absorption, PLE and PL measurements of the $Cs_2AgBiCl_6$ nanocrystals. The absorption spectrum shows an intense band centered at 360 nm and strong absorption at wavelengths shorter than 320 nm. The intense absorption band originates from the lowest energy direct band-gap transition of $Cs_2AgBiCl_6$. There is an indirect band-gap transition at longer wavelengths, which is characterized by a slow onset of the absorption band. This onset

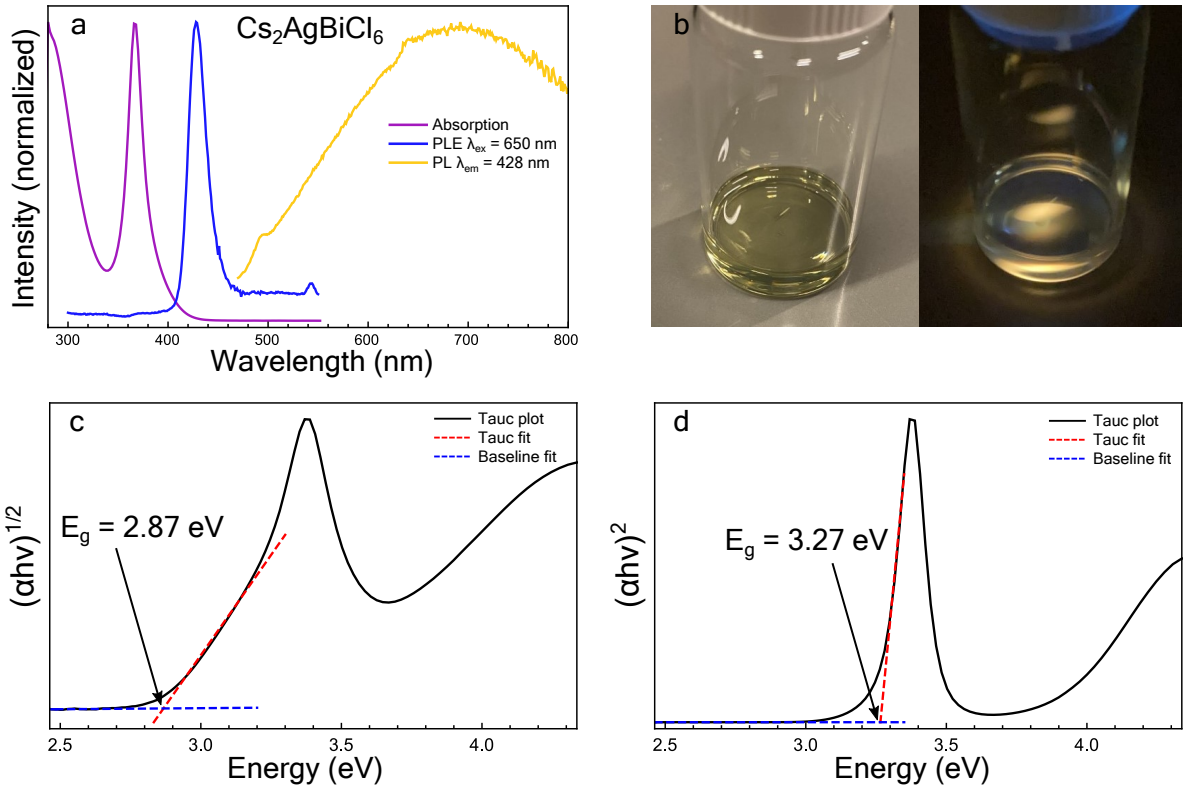

Figure 4.4: Optical properties of the synthesized nanocrystals. (**a**) Absorption, PLE and PL spectra of the $Cs_2AgBiCl_6$ nanocrystals. (**b**) Photograph of the nanocrystal solution under normal light (left) and 405 nm blue (right) laser light excitation. (**c,d**) Tauc plots of the absorption spectrum in indirect mode (**c**) and direct mode (**d**). Result of the fit of the Tauc plots is 2.87 eV for the indirect band gap and 3.27 eV for the direct band gap.

is hard to observe, because it is overshadowed by the intense direct transition. A way to gain insight in the energy of the indirect transition - as well as the direct transition - is to compute a Tauc plot. In a Tauc plot, the photon energy in eV is plotted against the quantity $(\alpha h\nu)^{1/r}$. Where α is the absorption coefficient, h is Planck's constant, ν is the frequency of the photon and r is a number denoting the nature of the transition ($r = \frac{1}{2}$ for direct transitions, $r = 2$ for indirect transitions). When the linear region of this plot is extrapolated to the base of the plot, one obtains an estimate of the optical band gap energy. **Figure 4.4 (c,d)** shows Tauc plots of the absorption spectrum of the $Cs_2AgBiCl_6$ nanocrystals with indirect **(c)** and direct **(d)** calculation. The result of the fit is an indirect band gap of 2.87 eV ($\lambda_{indirect}$ = 432 nm) and a direct band gap of 3.27 eV (λ_{direct} = 379 nm). The value of the indirect band gap is in line with what is found in previous reports (2.9 eV) [14, 39].

In **figure 4.4 (a)**, the PL spectrum shows a broad emission band ranging from about 450 nm into the near-IR when excited with 428 nm light. The emission is very broad, weak and has a large stokes shift, in line with what previous reports have found [19, 39]. It is emission characteristic of a self-trapped exciton (STE). In this material, the holes have a high effective mass (low carrier mobility) and are likely to be locally trapped, causing a lattice deformation and a more stable excited state. Specifically in this material, the holes can get trapped on $[AgCl_6]^{5-}$ octahedra [49]. This process is illustrated in **figure 4.5 (a)**. When a hole diffuses to a $[AgCl_6]^{5-}$ octahedron, effectively an electron is taken away from the Ag^+ ion and the $4d^{10}$ configuration changes to $4d^9$. The $4d^9$ electron configuration can induce a Jahn-Teller distortion, which is an

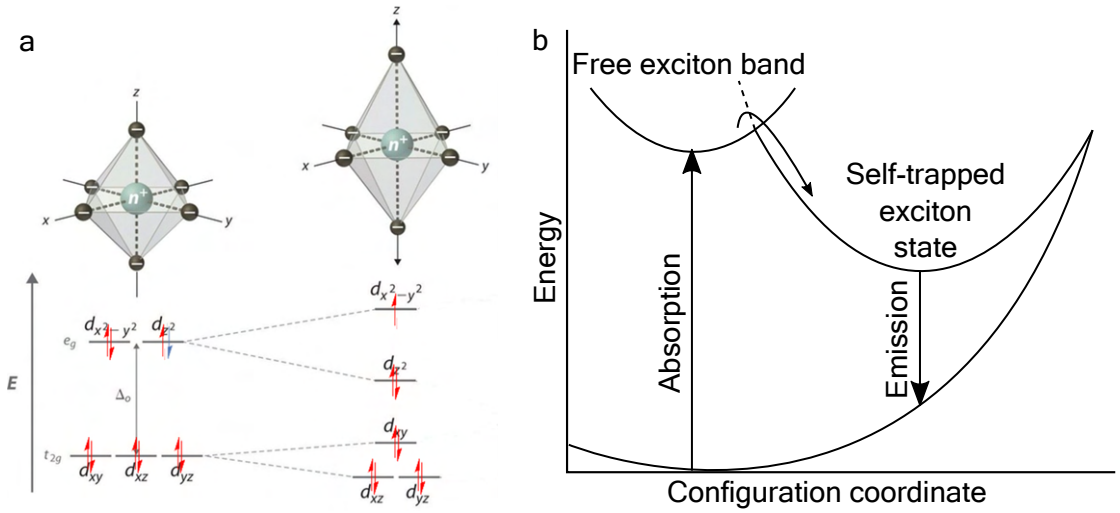

Figure 4.5: Illustration of the lattice deformation caused by hole trapping on $[AgCl_6]^{5-}$ octahedra. **(a)** Jahn-Teller distortion visualized with corresponding electron configuration diagrams. **(b)** Configuration coordinate diagram showing the stabilized STE state.

elongation of the bonds on the z-axis and a compression of the bonds on the x- and y-axis (or vice versa). This causes a splitting of the e_g orbitals, which reduces the system in energy. As a results, the trapping of a hole on a $[AgCl_6]^{5-}$ creates a stabilized state localized in the lattice.

This can also be illustrated in a configuration coordinate diagram shown in **figure 4.5 (b)**. The STE state involves a significant change in bond lengths in the excited state. This results in a large offset of the excited state in the configuration coordinate diagram. This results in a large Stokes shift and a very broad emission band, like we see in the emission spectrum of the $Cs_2AgBiCl_6$ nanocrystals.

The PLE spectrum of the STE emission shows a single peak centered around 430 nm. It is red-shifted relative to the absorption spectrum, which is not expected. In this case, the concentration of nanocrystals is too high. The nanocrystals have extremely strong absorption when concentrated, so light can not pass through the solution. Therefore, the absorption is too strong at shorter wavelengths than about 400 nm and the light cannot penetrate deeply enough into the sample. As a result, the part of the cuvet which is measured for photoluminescence is not excited and the detector collects no reading. Im later measurements, this will be resolved.

Summarizing the analysis of the synthesized nanocrystals, $Cs_2AgBiCl_6$ nanocrystals are cubic nanocrystals with an average edge length of 9.9 nm. The nanocrystals are phase pure according to the XRD measurements. They have strong absorption in the UV-region due to band to band absorption (E_g = 2.87 eV (indirect), 3.27 eV (direct)) and show a weak yellow luminescence originating from STEs.

Ytterbium doping

Now that the host material has been discussed, we investigate the potential for lanthanide incorporation. The first lanthanide we investigate is Yb^{3+}. $Cs_2AgBiCl_6$ nanocrystals have already been doped with Yb^{3+} in the literature by Chen *et al.* [19]. Before we attempt doping with other lanthanides, we first reproduce the results of Chen *et al.* [19]. The authors found that doping with Yb^{3+} replaces Bi^{3+} and that it does not change the crystal structure. They found that Yb^{3+}-doping introduces an additional emission peak in the near-IR, centered at 1000 nm. This emission peak is assigned to the $^2F_{\frac{5}{2}} \longrightarrow {}^2F_{\frac{7}{2}}$ transition of Yb^{3+} and the authors suggest that the emission is sensitized by the $Cs_2AgBiCl_6$ host through an energy transfer process.

The synthesis used for Yb^{3+}-doping of the $Cs_2AgBiCl_6$ nanocrystals is based on the same protocol of Creutz *et al.* [39] with slight modifications for Yb^{3+} incorporation. On top of the precursors used for the undoped synthesis, $Yb(CH_3CO_2)_3$ is simply added to the reaction in ratio 0.05:1 $Yb(CH_3CO_2)_3$:$Bi(CH_3CO_2)_3$ (see experimental section). For this synthesis, a washing step with ethyl acetate was investigated. In this washing step, the nanocrystals are crashed out of solution by ethyl acetate, which acts as an antisolvent. The precipitated nanocrystals are isolated and redispersed in toluene.

To investigate the structural properties of the synthesized Yb^{3+}-doped $Cs_2AgBiCl_6$ nanocrystals, XRD and TEM measurements were performed. **Figure 4.6** presents the structural analysis

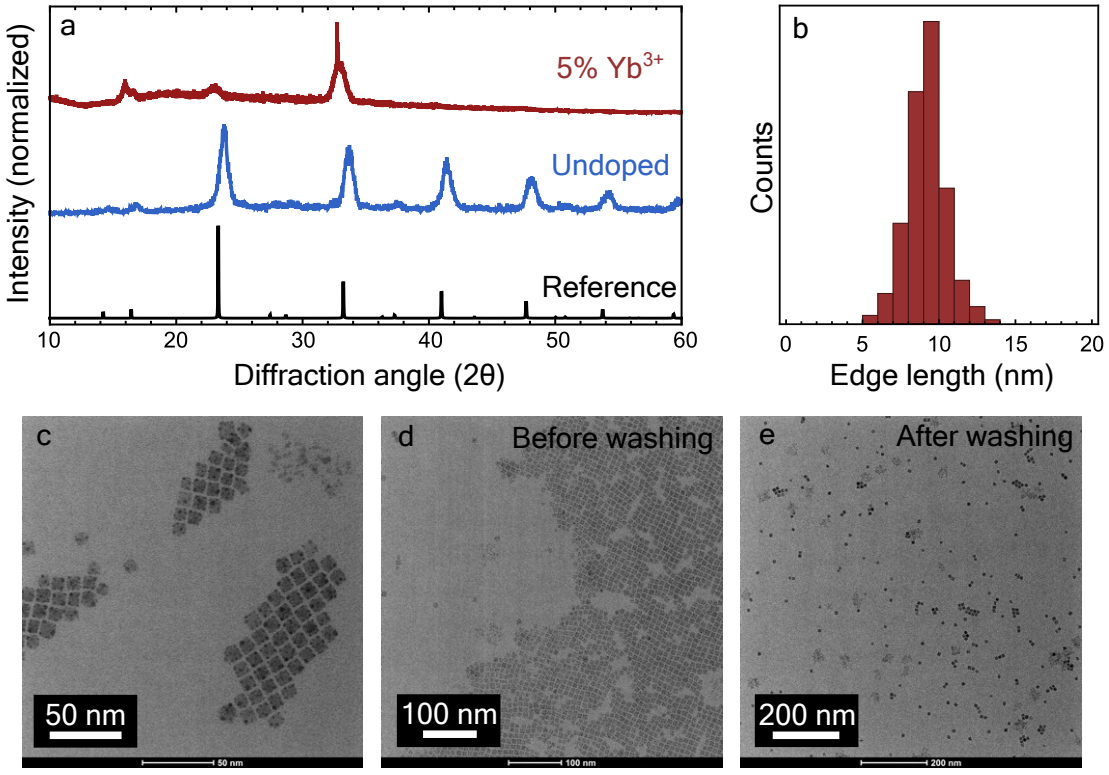

Figure 4.6: Structural data of the Yb^{3+}-doped $Cs_2AgBiCl_6$ nanocrystals. (**a**) XRD measurements of the Yb^{3+}-doped nanocrystals (top), the undoped nanocrystals (middle), reference (bottom). (**b**) Histogram of the edge lengths of the nanocrystals based on TEM images (average edge length 9.2 nm). (**c,d,e**) TEM images of the Yb^{3+}-doped nanocrystals. Images (**c**) and (**d**) show the difference in packing of the nanocrystals before and after a washing step with ethyl acetate.

data for the synthesized Yb^{3+}-doped $Cs_2AgBiCl_6$ nanocrystals. In **figure 4.6 (a)** the XRD measurements of the Yb^{3+}-doped (top), undoped (middle) $Cs_2AgBiCl_6$ nanocrystals are shown with a calculated reference (bottom). All reflection peaks are present, although some at low intensity. No impurities are visible on the XRD. A sharp peak is present at around 33 2θ. The reflection peaks that are more strongly present are the (200) and the (400) lattice plane reflections. This is not indicative of a wrong crystal phase. When preparing the XRD sample, the nanocrystals can aggregate in an ordered way so that some reflections are better aligned to the x-ray beam path than others. This causes some reflection peaks to be more intense compared to when the sample is homogeneously mixed. Interestingly, the dominant reflections are the (200) and (400) reflections, which are the lattice planes along the walls of the cubes. Therefore, it seems that the nanocrystals are organized so that the flat side of the cubic nanocrystals is oriented to the top just like in the TEM images. The sharp peak at 33 2θ could be explained by the fact that the sample had been stored for a while before measuring XRD. Possibly, some of the nanocrystals aggregated over time to form larger crystals, resulting in sharp peak due to less Scherrer broadening.

Figure 4.6 (b-e) show the results of the TEM measurements. The nanocrystals have cubic shapes and have average edge lengths of 9.2 nm. The TEM images show that Yb^{3+}-doping does not affect the shape of the nanocrystals, but the average edge length is slightly smaller than the undoped crystals. There is a major difference between the images of before **(d)** and after **(e)** the washing step with ethyl acetate. Before washing, the deposited dry nanocrystals are aggregated into large nanocrystal clusters. After washing the nanocrystals are significantly more separated. It seems that the concentration of nanocrystals has significantly decreased upon washing. This could be due to (1) loss of nanocrystals that do not crash out of solution upon adding the antisolvent ethyl acetate and (2) loss of nanocrystals that are not redispersed into solution after adding toluene. Option 1 is possible, although the supernatant after centrifuging was colorless, indicating that the majority of the nanocrystals crashed out of solution. Option 2 is more likely since a residue of nanocrystals was present after redispersing the washed precipitate in toluene. The fact that not all the precipitate redissolves could be due to ligand stripping effects of the anti solvent. The washing step does not only separate the nanocrystals from impurities in solution such as precursors, but also ligands. The ligands coordinated to the nanocrystals are in a dynamic equilibrium with ligands in the solution. When the ligands in solution are removed by the washing step, the ligands coordinated to the nanocrystals partially dissolve into solution again to restore the equilibrium. This results in nanocrystals with less coordinating ligands. As a result, the nanocrystals are less soluble [50]. The separation in the TEM image is not necessarily a bad thing, however it indicates that the nanocrystals are partially stripped of ligands, which can result in reduced solubility and worse surface passivation. Nevertheless, the structural data confirms that the synthesized nanocrystals are phase pure cubic nanocrystals.

To investigate the optical properties of the Yb^{3+}-doped $Cs_2AgBiCl_6$ nanocrystals, we performed absorption and photoluminescence (excitation) measurements. **Figure 4.7** presents the optical data of the Yb^{3+}-doped $Cs_2AgBiCl_6$ nanocrystals. The absorption spectrum (**fig. 4.7(a)**) of the Yb^{3+}-doped nanocrystals matches the absorption spectrum of the undoped nanocrystals perfectly. The PL/PLE spectra of the STE emission (**fig. 4.7 (b)**) are very similar, although there is a kink in the emission spectrum at around 490 nm, which is due to the 444 nm long pass filter used in this measurement. When we look at the near-IR PL/PLE spectra (**fig. 4.7 (c)**) we see that a narrow emission peak centered around 1000 nm arises. Sharp emission at this wavelength is characteristic for the $^2F_{\frac{5}{2}} \longrightarrow {}^2F_{\frac{7}{2}}$ transition of Yb^{3+} [19]. When we measure an excitation

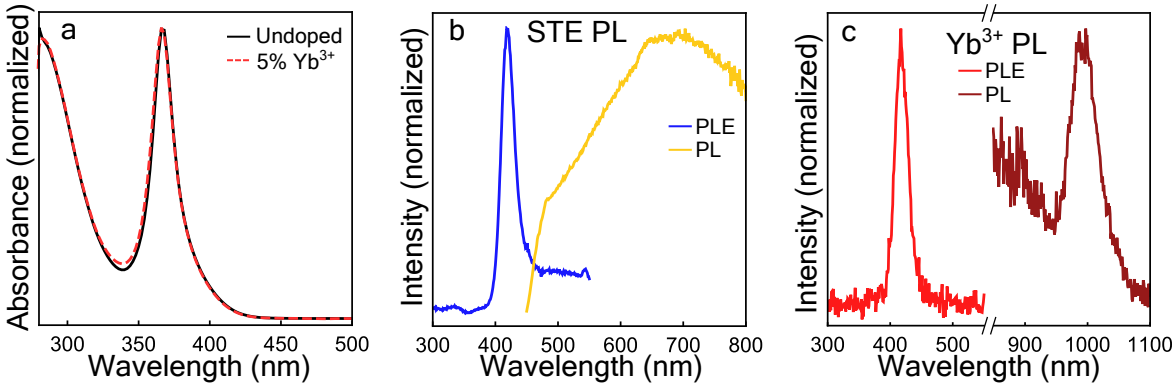

Figure 4.7: Optical properties of $Cs_2AgBiCl_6$ nanocrystals doped with 5% Yb^{3+}. (**a**) Absorption spectra of the undoped and Yb^{3+}-doped nanocrystals. (**b**) Photoluminescence (excitation) spectra of the STE emission ($\lambda_{ex} = 419nm$, $\lambda_{em} = 650nm$). (**c**) PL(E) spectra of the near-infrared Yb^{3+} emission ($\lambda_{ex} = 419nm$, $\lambda_{em} = 993nm$).

spectrum of the near-IR emission, a peak centered around 410 nm is observed. This excitation spectrum matches the excitation spectrum of the STE emission well. This is a good indication that the near-IR emission from Yb^{3+} is excited in the host material: $Cs_2AgBiCl_6$ absorbs light and an energy transfer process occurs from $Cs_2AgBiCl_6$ to Yb^{3+}, as earlier reports have found as well [19].

Summarizing, structural data shows that the incorporation of Yb^{3+} does not affect the crystal structure and nanocrystals morphology. The optical measurements showed that the synthesized Yb^{3+}-doped $Cs_2AgBiCl_6$ nanocrystals retain their optical properties, while an additional near-IR emission peak arises, originating from the $^2F_{\frac{5}{2}} \longrightarrow {}^2F_{\frac{7}{2}}$ transition of Yb^{3+}. Excitation measurements suggest that the Yb^{3+} emission is excited in the host material. Furthermore, a washing step with ethyl acetate did not prove to be advantageous.

Europium doping

Next, we investigate the lanthanide ion Eu^{3+} as a dopant in $Cs_2AgBiCl_6$ nanocrystals. We investigate whether red emission from Eu^{3+} is sensitized by the host material as well. The synthesis of the Eu^{3+}-doped $Cs_2AgBiCl_6$ is based on the protocol of Creutz *et al.* [39]. The same strategy is applied as with Yb^{3+} doping, where the dopant is simply added to the reaction. In this case $Eu(CH_3CO_2)_3$ was added in a stochiometric ratio of 0.05:1 $Eu(CH_3CO_2)_3$:$Bi(CH_3CO_2)_3$. No washing steps were performed. To our knowledge, there have been no reports about Eu^{3+} doping in $Cs_2AgBiCl_6$ in the literature.

To investigate the structural properties of the Eu^{3+}-doped $Cs_2AgBiCl_6$ nanocrystals, we performed XRD and TEM measurements. **Figure 4.8** presents the structural analysis data for the Eu^{3+}-doped nanocrystals. The XRD measurements (**fig. 4.8 (a)**) of the Eu^{3+}-doped nanocrystals (top) are very similar to the XRD measurements of the undoped nanocrystals (middle). A shift in diffraction angle of the reflection is not noticeable, possibly due to the broadness of the peaks. This indicates that either Eu^{3+} has a very similar ion radius in this crystal to Bi^{3+}, or that very little to no Eu^{3+} is incorporated in the crystal. The TEM images (**fig. 4.8 (b)**) show cubic nanocrystals with small black Ag^0 clusters. These nanocrystals are less well defined than the undoped and Yb^{3+}-doped nanocrystals. Some nanocrystals seem to be disintegrated. This

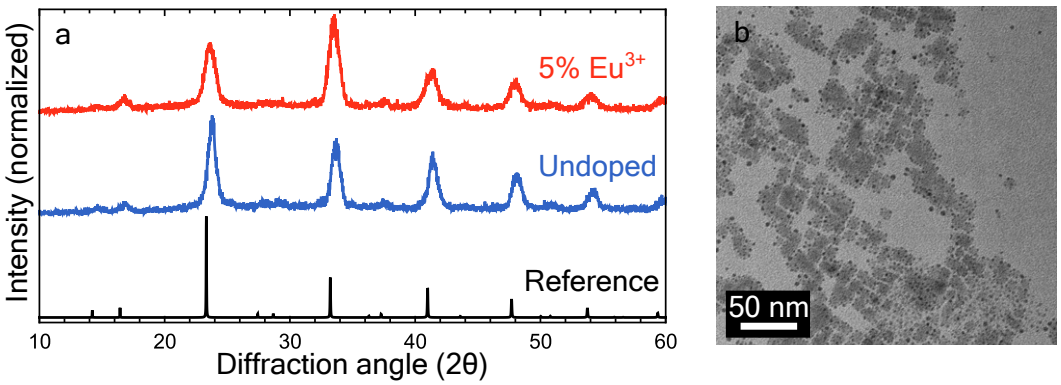

Figure 4.8: Structural data of the Eu^{3+}-doped $Cs_2AgBiCl_6$ nanocrystals. (**a**) XRD measurements of the Eu^{3+}-doped nanocrystals (top), the undoped nanocrystals (middle), reference (bottom). (**b**) TEM image of the nanocrystals.

could be due to prolonged beam exposure in the TEM. When exposing the nanocrystals too long to the electron beam of the TEM, the electrons damage the nanocrystals, causing them to degrade and become less well-defined crystals. For this reason, it was not possible to construct an accurate histogram of the nanocrystal edge lengths. However, judging from the TEM image, the nanocrystals have the same shape as their undoped and Yb^{3+}-doped counterparts. The structural data indicates that the synthesized Eu^{3+}-doped $Cs_2AgBiCl_6$ nanocrystals are structurally comparable to the undoped nanocrystals, however it is not clear to what extent Eu^{3+} is incorporated into the lattice.

To investigate the optical properties of the synthesised Eu^{3+}-doped $Cs_2AgBiCl_6$ nanocrystals, we performed absorption and PL(E) measurements. **Figure 4.9** presents the optical analysis data of the nanocrystals doped with 5% Eu^{3+}. The absorption spectrum (**fig. 4.9 (a)**) matches perfectly with the undoped nanocrystals. The PL measurements are very similar to the undoped nanocrystals as well. Although, the excitation spectrum of the STE emission shows a peak centered around 365 nm and matches the absorption spectrum well, compared to previously discussed measurements. This is due to the higher (and correct) dilution of the sample. No Eu^{3+} emission is observed in the emission spectrum when excited with 360 nm light. We were also

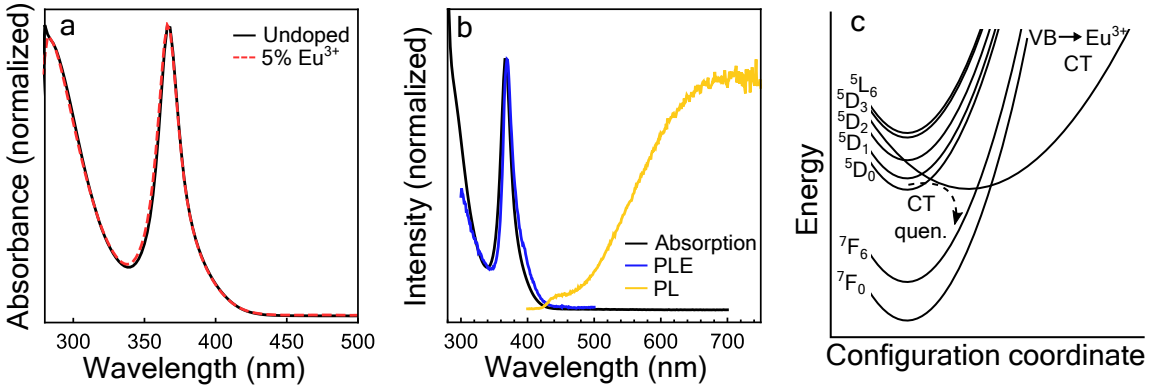

Figure 4.9: Optical properties of $Cs_2AgBiCl_6$ nanocrystals doped with 5% Eu^{3+}. (**a**) Absorption spectra of the undoped and Eu^{3+}-doped nanocrystals. (**b**) Photoluminescence (excitation) spectra ($\lambda_{ex} = 370nm$, $\lambda_{em} = 650nm$). (**c**) Configuration coordinate diagram showing charge transfer quenching of Eu^{3+} through a VB $\longrightarrow$ Eu^{3+} charge transfer state.

unable to observe any Eu^{3+} excitation peaks when measuring an excitation spectrum directly at the wavelength of the $^5D_0 \longrightarrow {}^7F_2$ emission (615 nm) with wide emission slit width. Thus, the sample does not show any Eu^{3+} emission. There are two possible explanations for this. The first explanation is that Eu^{3+} is not incorporated into the lattice during the synthesis. It was not clear from the structural analysis that Eu^{3+}-incorporation was successful. Different analysis techniques are needed to confirm this, such as ICP-OES or STEM-EDX. However, incorporation of Yb^{3+} was successful and Eu^{3+} is chemically very similar to Yb^{3+}. Therefore, it seems that this explanation is unlikely, especially because the ionic radius of Eu^{3+} (0.95 Å) matches Bi^{3+} (1.03 Å) better than Yb^{3+} (0.87 Å). The second explanation is that the luminescence of Eu^{3+} is quenched in this host. Quenching of Eu^{3+} in solids occurs predominantly due to charge transfer (CT) quenching. It is possible that the VB $\longrightarrow$ Eu^{3+} charge transfer state is located at low energies and has significant overlap with the ground state and the ^5D_n levels of Eu^{3+}, like is shown in **figure 4.9 (c)**. Then, when Eu^{3+} is excited into the $^5D_0$ energy levels, it can non-radiatively transition to the ground state. This could be investigated further by measuring emission and excitation of Eu^{3+} at liquid helium temperatures. It is possible that Eu^{3+} emission can then be observed, since CT quenching is a thermally activated process.

Summarizing, the synthesized Eu^{3+}-doped $Cs_2AgBiCl_6$ nanocrystals show no Eu^{3+} emission, which is possibly due to poor incorporation of Eu^{3+} into the crystal lattice or charge transfer quenching.

Terbium doping

The final lanthanide we investigate as a dopant in $Cs_2AgBiCl_6$ is Tb^{3+}. Tb^{3+} has characteristic green emission originating from its $^5D_4 \longrightarrow {}^7F_5$ transition. We investigate whether Tb^{3+} emission is present in $Cs_2AgBiCl_6$ and if it is sensitized by the host material. The synthesis of the Tb^{3+}-doped $Cs_2AgBiCl_6$ nanocrystals is based on the protocol of Creutz *et al.* [39]. The same strategy is applied as with Yb^{3+} and Eu^{3+} doping, where the dopant is simply added to the reaction. In this case $Tb(CH_3CO_2)_3$ was added in a stochiometric ratio of 0.05:1 $Tb(CH_3CO_2)_3$:$Bi(CH_3CO_2)_3$. No washing steps were performed.

To investigate the structural properties of the Tb^{3+}-doped $Cs_2AgBiCl_6$ nanocrystals, we performed XRD and TEM measurements. **Figure 4.10** presents the structural analysis data for

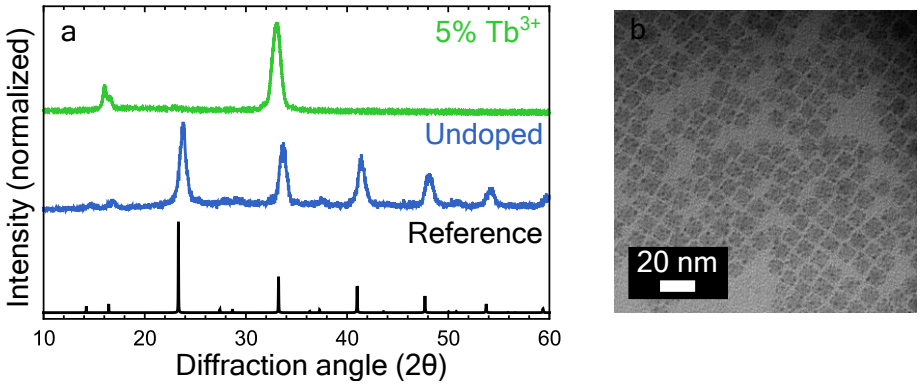

Figure 4.10: Structural data of the Tb^{3+}-doped $Cs_2AgBiCl_6$ nanocrystals. (**a**) XRD measurements of the Tb^{3+}-doped nanocrystals (top), the undoped nanocrystals (middle), reference (bottom). (**b**) TEM image of the nanocrystals.

the 5% Tb^{3+}-doped nanocrystals. The XRD (**fig. 4.10 (a)**) mainly shows the (200) and (400) lattice plane reflection peaks. The other reflections are only slightly visible. No impurity peaks are present. The reflection peak at 31.5 2θ seems to be slightly shifted to lower diffraction angles compared to the undoped nanocrystals, however it is difficult to attribute this to lattice expansion because the XRD measurements of the Tb^{3+}-doped and undoped nanocrystals were performed on different X-ray diffractometers. The TEM image **(b)** shows monodisperse cubic nanocrystals, similar to the undoped nanocrystals. The structural data shows that Tb^{3+} doping does not affect the crystallinity of the nanocrystals significantly.

To investigate the optical properties of the Tb^{3+}-doped $Cs_2AgBiCl_6$ nanocrystals, we performed absorption and PL(E) measurements. **Figure 4.11** presents the optical data for the 5% Tb^{3+}-doped nanocrystals. The absorption spectrum (**fig. 4.11 (a)**) differs from the undoped nanocrystals. An additional feature at 330-340 nm is found, as well as a stronger tail at shorter than 320 nm wavelength. This indicates that there is an additional absorption process, which is not present in the undoped nanocrystals, likely due to the presence of Tb^{3+}. The emission spectrum (**fig. 4.11 (b)**) shows the broad STE emission and additionally, a sharp peak at 545 nm and small peaks at 490, 590 and 620 nm. These additional peaks are characteristic for Tb^{3+}. These peaks originate from the $^5D_4 \longrightarrow {}^7F_n$ transitions from Tb^{3+}, where the peaks and transitions correspond as follows: n = 6 for 490 nm, n = 5 for 545 nm, n = 4 for 590 nm and n = 3 for 620 nm. This confirms that there is Tb^{3+} emission present in the sample. The excitation spectrum of the STE emission shows a peak centered around 365 nm and matches the absorption spectrum well.

To investigate the origin of the Tb^{3+} emission further, we measured excitation spectra of the Tb^{3+} emission and the STE emission. **Figure 4.11 (c)** shows these excitation spectra (normalized) along with the absorption spectrum. It is difficult to measure an accurate excitation spectrum of exclusively the Tb^{3+} emission, as there is a lot of background emission of the STE emission. When we compare the excitation spectra, it is clear that the Tb^{3+} excitation spectrum has a stronger "bump" in the excitation spectrum around 330 nm. This might be due to an excitation process which directly excites the Tb^{3+}. Some of the f-f transitions of Tb^{3+} are located at this wavelength and Tb^{3+} can also have an f-d transition in this region. It is not clear from these spectra however, if the Tb^{3+} emission is excited in the host material, as there is too much STE background emission.

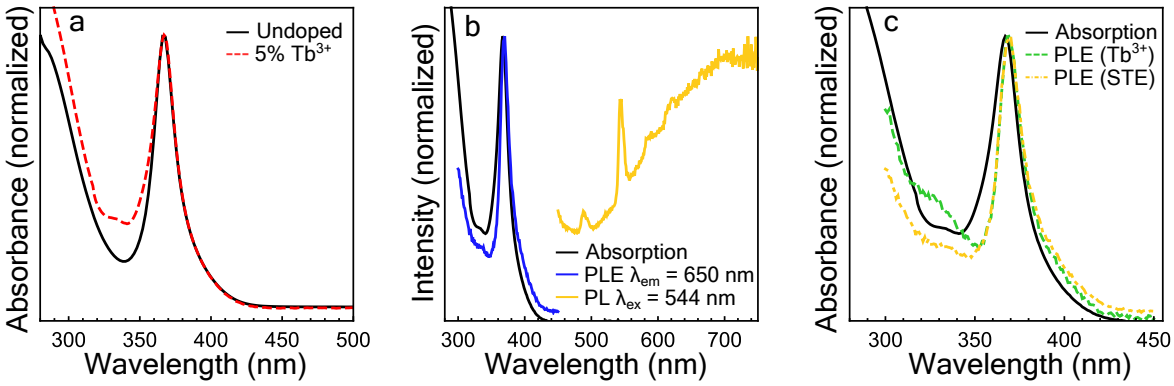

Figure 4.11: Optical properties of $Cs_2AgBiCl_6$ nanocrystals doped with 5% Tb^{3+}. (**a**) Absorption spectra of the undoped and Tb^{3+}-doped nanocrystals. (**b**) Absorption and photoluminescence (excitation) spectra. (**c**) Absorption, PLE spectra of the Tb^{3+} emission ($\lambda_{em} = 544nm$) and the STE emission ($\lambda_{em} = 650nm$).

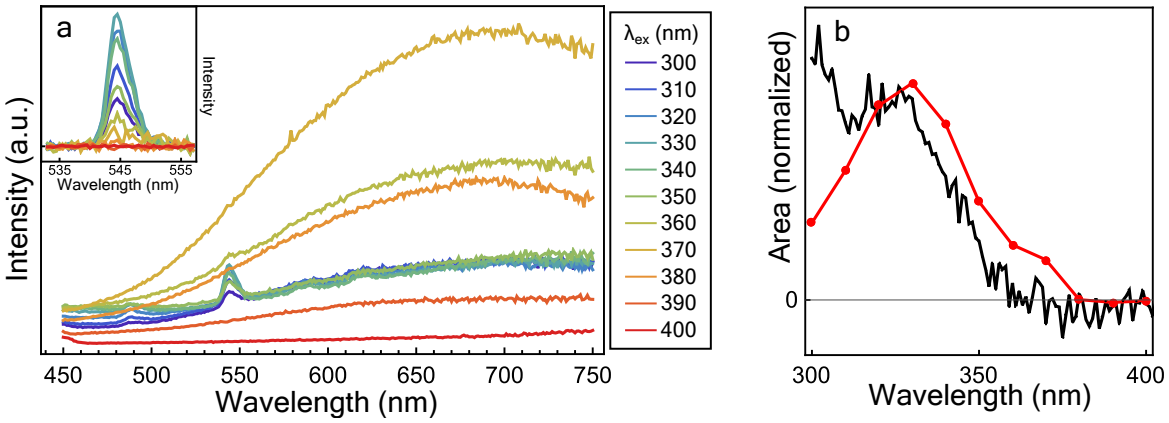

Figure 4.12: PL measurements using varying excitation wavelengths. (**a**) Emission spectra of the $Cs_2AgBiCl_6$ nanocrystals doped with 5% Tb^{3+} measured at varying excitation wavelengths, inset shows the emission of Tb^{3+} corrected for the background STE emission. (**b**) Excitation spectrum of the Tb^{3+} emission calculated in two ways. black: excitation spectrum of the Tb^{3+} emission subtracted by the excitation spectrum of the STE emission. Dotted red: the area of the Tb^{3+} emission peak by excitation wavelength.

To gain more insight about the nature of the Tb^{3+} emission, we measured the emission spectra of the Tb^{3+}-doped nanocrystals at various excitation wavelengths. **Figure 4.12 (a)** shows the emission spectra with varying excitation wavelengths. The broad STE emission is present at all excitation wavelengths with varying intensity. However, the Tb^{3+} emission at 545 nm is only present at excitation wavelengths 300-360 nm. So, when exciting at wavelengths >360 nm, the host material is excited and excitons are generated but no Tb^{3+} emission is present. This indicates that the excitation of Tb^{3+} likely does not occur via the STE, and thus Tb^{3+} is likely not excited in the host material.

With the data at hand, it is possible to sketch a rough excitation spectrum of the Tb^{3+} emission in two ways: (1) by subtracting the excitation spectrum of the Tb^{3+} emission by the excitation spectrum of the STE emission. This way a correction for the background STE emission is performed. (2) By calculating the area of the Tb^{3+} peak of the various emission spectra in the emission map and plotting the area against the corresponding excitation wavelength. The area of the Tb^{3+} peak was calculated as follows: first, a third order polynomial was fitted to the background emission around the Tb^{3+} emission of each individual spectrum. Then, the emission spectra ranging from 520 to 570 nm were subtracted by the fit polynomials. The result of the subtraction is shown in the inset in **figure 4.12 (a)**. When we plot the area of the isolated Tb^{3+} spectra against their corresponding excitation wavelength, we obtain a rough excitation spectrum for the Tb^{3+} emission. The result of these two methods is shown in **figure 4.12 (b)**. The two methods agree with each other quite well, except for the increase at <310 nm for the excitation spectrum subtraction. Other than this feature, both excitation spectrum "sketches" shows a broad excitation band centered around 330 nm. This type of broad excitation band is typical for a Tb^{3+} f-d transition. Since Tb^{3+} is not excited in the host material, it is likely that the Tb^{3+} emission is instead excited in the f-d transition band. This band also explains the additional feature in the absorption spectrum of the Tb^{3+}-doped nanocrystals.

To summarize the optical analysis of the synthesized Tb^{3+}-doped $Cs_2AgBiCl_6$ nanocrystals, Tb^{3+} doping introduced an additional feature in the absorption spectrum due to the f-d transition of Tb^{3+}. When exciting the material in this f-d band, we observed emission characteristic of

Tb^{3+}, as well as STE emission. When exciting the host material at energies outside the f-d absorption band only STE emission was present, suggesting that host excitation does not lead to Tb^{3+} emission.

4.1.2 $Cs_2AgBiBr_6$

The next crystal structure we investigate is $Cs_2AgBiBr_6$. $Cs_2AgBiBr_6$ is structurally and electronically very similar to $Cs_2AgBiCl_6$. Yb^{3+} and Eu^{3+} incorporation into $Cs_2AgBiBr_6$ microcrystals has been attempted before [18], as well as Yb^{3+} incorporation into the nanocrystals [19]. In both the micro- and nanocrystals Yb^{3+} incorporation resulted in near-IR emission from the $^2F_{\frac{5}{2}} \longrightarrow {}^2F_{\frac{7}{2}}$ transition of the Yb^{3+} dopant, sensitized by the host material. Eu^{3+} incorporation resulted in emission from a Eu^{3+}-induced trap state located within the band gap, but no f-f emission was observed. Based on the fact that Eu^{3+} emission is absent in Eu^{3+}-doped $Cs_2AgBiCl_6$ nanocrystals and in $Cs_2AgBiBr_6$ microcrystals [18], it is likely that Eu^{3+} luminescence is quenched in $Cs_2AgBiBr_6$ due to CT quenching. Therefore, $Cs_2AgBiBr_6$ is not a suitable host to sensitize Eu^{3+}. However, it is still important to further investigate $Cs_2AgBiBr_6$ doped with Yb^{3+} to gain insight into the mechanism of energy transfer from host to lanthanide to aid in further research.

In order to gain insight into the luminescence of $Cs_2AgBiBr_6$ and the energy transfer mechanism from host to Yb^{3+}, a series of nanocrystals was synthesized with varying doping concentrations of Yb^{3+} (0, 2.5, 5, 10, 25, 50%). The synthesis was based on a protocol from Creutz *et al.* [39], where the desired amount of dopant precursor ($Yb(CH_3CO_2)_3$) was simply added to the reaction in varying amounts of fractions of $Bi(CH_3CO_2)_3$ content.

To investigate the structural properties of the undoped and Yb^{3+}-doped $Cs_2AgBiBr_6$ we performed XRD and TEM measurements. We performed elemental analysis using ICP-OES to determine the actual Yb^{3+} doping concentration. **Figure 4.13** presents the structural data for the undoped and 5% Yb^{3+}-doped nanocrystals. The XRD pattern (**fig. 4.13 (a)**) shows predominantly the (200) and (400) lattice plane reflections. These peaks agree with the reference pattern well. The other reflections are also present but at low intensities. There is not a significant diffraction angle shift upon doping. There are no peaks present due to impurities, indicating that the nanocrystals are phase pure. The TEM images of the undoped **(b)** and Yb^{3+}-doped **(c)** nanocrystals show monodisperse cubic nanocrystals. The Ag^0 nanoclusters seem to be less present in the bromides nanocrystals, although they are still present. Doping does not affect the morphology of the nanocrystals.

The actual doping concentrations determined by ICP-OES are shown in **table 4.1**. We see that the actual incorporation of Yb^{3+} is very low compared to the amount added into the reaction.

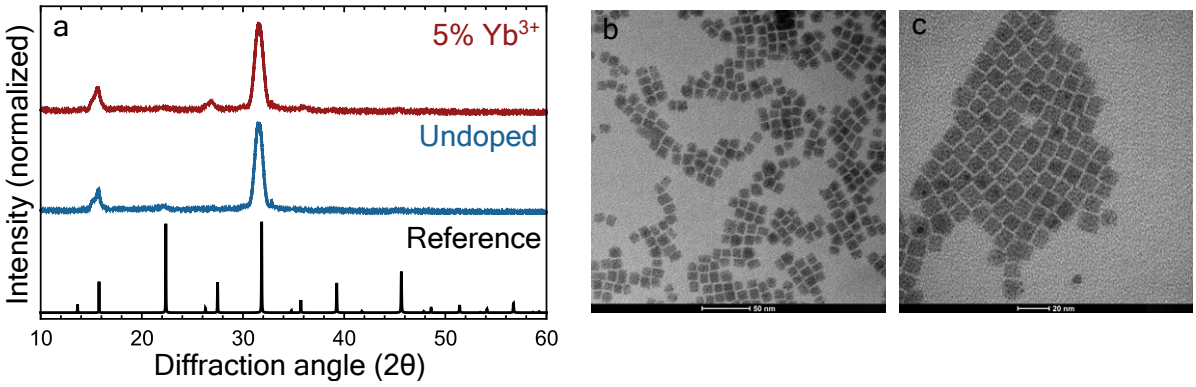

Figure 4.13: Structural data for the undoped and 5% Yb^{3+}-doped $Cs_2AgBiBr_6$ nanocrystals. **(a)** XRD of the undoped and 5% Yb^{3+}-doped nanocrystals. **(b)** TEM image of the undoped nanocrystals. **(c)** TEM image of the 5% Yb^{3+}-doped nanocrystals.

Bi^{3+} added (mmol):	Yb^{3+} added (mmol):	Yb^{3+} doping %:	Actual doping %:
0.5	0	0	0
0.5	0.0125	2.44	0.16
0.5	0.025	4.76	0.23
0.5	0.05	9.09	0.30
0.5	0.125	20	0.68
0.5	0.25	33.33	1.80

Table 4.1: Yb^{3+} doping percentages determined with ICP-OES. Doping percentages are represented by the percentage of Bi^{3+} that Yb^{3+} replaces in the lattice: doping% = [Yb]/([Yb]+[Bi]).

This is surprising, since the Bi^{3+} lattice site is slightly larger than the ionic radius of Yb^{3+} and the site has coordination number 6. This should accommodate Yb^{3+} doping quite well. Possibly, due to the hard Lewis acid nature of the lanthanides, Yb^{3+} binds more strongly to oleic acid than the weaker lewis acid Bi^{3+}[15]. Because of the higher energy needed to dissociate Yb^{3+} from the ligands, the incorporation of Yb^{3+} into the crystal during the reaction might be slightly slower than Bi^{3+}. Interestingly, Chen *et al.* [19] also performed elemental analysis and their Yb^{3+} incorporation is about tenfold higher compared to our measurements. The authors did not specify any washing steps before ICP measurements, so possibly washing significantly reduced the amount of Yb^{3+} in the sample. This indicates that there may still be significant amounts of Yb^{3+} precursor still present in the nanocrystal solution before washing, or that washing results in Yb^{3+} incorporated in the crystal dissolving into solution again. This could possibly be further investigated using STEM-EDX measurements. Nevertheless, the structural data indicates that the $Cs_2AgBiBr_6$ nanocrystals are phase pure and Yb^{3+} incorporation is successful, although in relatively low concentrations.

We first analyze the optical properties of the undoped $Cs_2AgBiBr_6$ nanocrystals. The results of the UV-Vis, PL and PLE spectroscopy measurements of the undoped nanocrystals are presented in **figure 4.14**. The absorption spectrum shows a peak with a slow onset centered around 430 nm. Absorption significantly increases at wavelengths shorter than 380 nm. The emission spectrum shows a broad band centered around 690 nm. The excitation spectrum of the emission overlaps the absorption spectrum. When we compare $Cs_2AgBiBr_6$ to its chloride counterpart (**fig. 4.14 (b)**), we see that the absorption spectrum shifts to longer wavelengths. The emission spectrum is narrower and the stokes shift is smaller. **Figure 4.14 (c,d)** show Tauc plots of the absorption spectra. The result of the fit is a band gap of 2.38 eV in indirect mode **(c)**, and 2.76 eV in direct mode **(d)**. These results are in line with what is found in earlier reports (2.3 eV for the indirect band gap) [14, 39]. It is clear that substituting Cl for Br results in a smaller band gap. Like in $Cs_2AgBiCl_6$, the emission is weak, broad and has a large Stokes shift. Earlier reports have assigned this emission to STE's as well [51]. The fact that the Stokes shift is smaller and that the emission is narrower in the bromide indicates that STE state is shallower. This would mean that the STE's in the bromide cause less lattice deformation. In **figure 4.5 (b)** this would look like a diagonal shift of the STE band closer to the free exciton band, so the band is offset less and the energy difference between free exciton and STE is less. This would result in

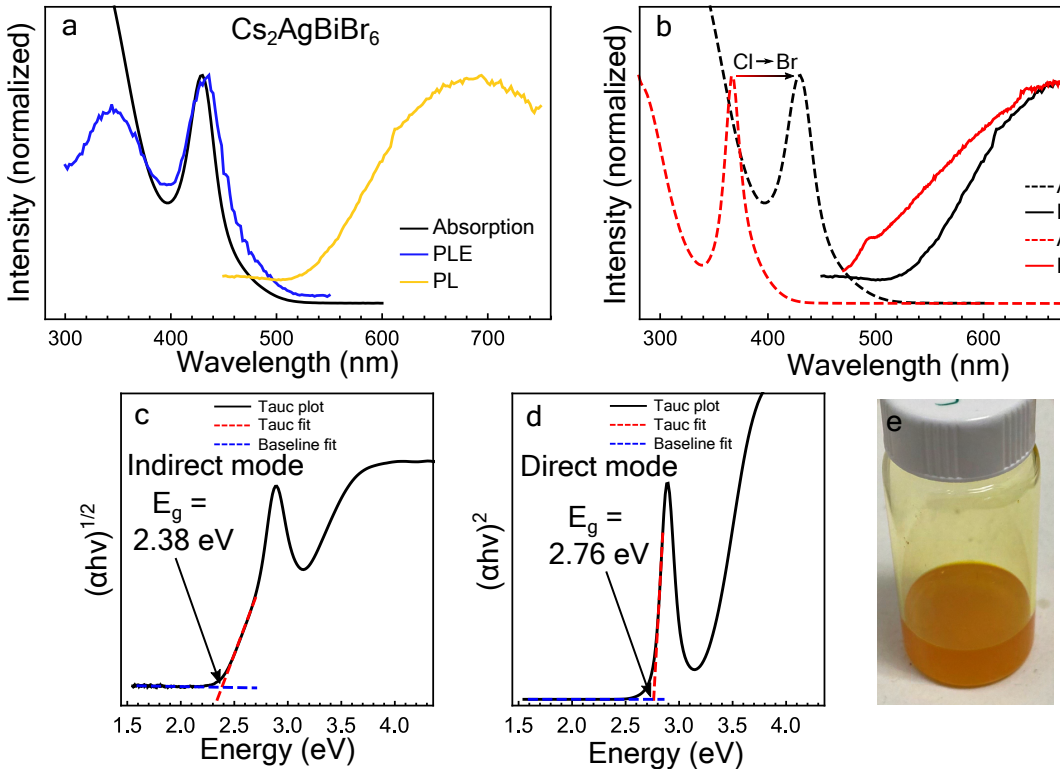

Figure 4.14: Optical properties of the $Cs_2AgBiBr_6$ nanocrystals. (**a**) Absorption, PLE and PL spectra of the $Cs_2AgBiBr_6$ nanocrystals. (**b**) Combined absorption and emission spectra of $Cs_2AgBiCl_6$ and $Cs_2AgBiBr_6$ nanocrystals, it is evident that the substitution of Cl by Br leads to a red-shifted absorption peak due to the decreased band gap. (**c,d**) Tauc plots of the absorption spectrum of $Cs_2AgBiBr_6$ nanocrystals in indirect mode (**c**) and direct mode (**d**). Result of the fit of the Tauc plots is 2.38 eV for the indirect band gap and 2.76 eV for the direct band gap. **(e)** Photograph of the $Cs_2AgBiBr_6$ nanocrystal solution, showing the orange color due to the strong absorption of blue light.

a relatively narrower emission band and a lower Stokes shift.

We now consider the synthesized $Cs_2AgBiBr_6$ nanocrystals with Yb^{3+} doping. Unfortunately, the quality of the samples with different Yb^{3+} doping concentrations varied a lot. Therefore, the samples were hard to compare and we only discuss one doping concentration. **Figure 4.15** presents the optical data for the 5% Yb^{3+}-doped nanocrystals. The absorption spectrum (**fig. 4.15 (a)**) of the Yb^{3+}-doped nanocrystals is nearly identical to the spectrum of the undoped nanocrystals, indicating that Yb^{3+} incorporation does not significantly alter the absorption of the crystal. The STE emission (**fig. 4.15 (b)**) is also largely unaffected. When we look at the near-IR emission spectrum (**fig. 4.15 (c)**), we see a sharp peak centered around 1000 nm. This emission peak originates from the $^2F_{\frac{5}{2}} \longrightarrow {}^2F_{\frac{7}{2}}$ transition of Yb^{3+}, like in the Yb^{3+}-doped $Cs_2AgBiCl_6$ nanocrystals. The excitation spectrum of the Yb^{3+} emission matches the absorption spectrum very well, indicating that the Yb^{3+} emission is excited in the host material. The intensity of the near-IR emission is significantly higher in the bromide, compared to the chloride. It is possible that the energy transfer from the host to Yb^{3+} is more efficient in the bromide. This could have several explanations. For example, incorporation of Yb^{3+} into the lattice is possibly better in the bromide nanocrystals. But possibly more important, the energy transfer efficiency could be higher in the bromide.

To know why the energy transfer is more efficient, it is important to investigate the energy

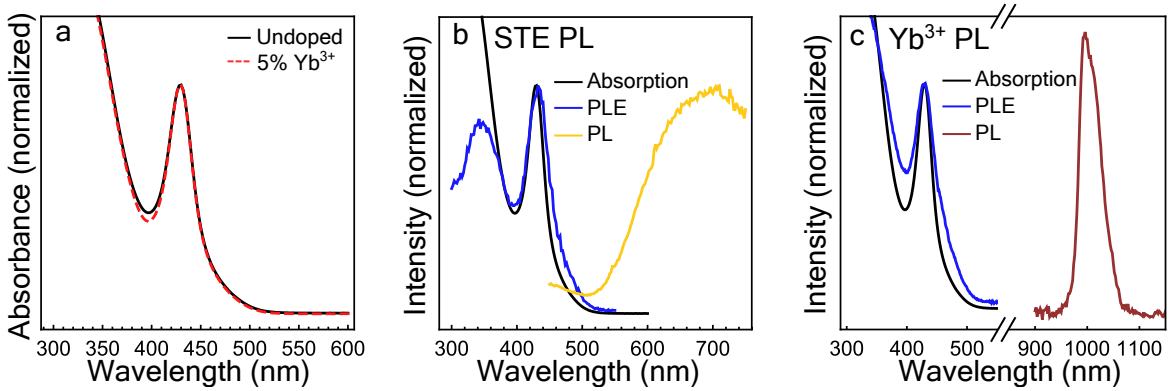

Figure 4.15: Optical properties of $Cs_2AgBiBr_6$ nanocrystals doped with 5% Yb^{3+}. (**a**) Absorption spectra of the undoped and Yb^{3+}-doped nanocrystals. (**b**) Absorption and PL(E) spectra of the STE emission ($\lambda_{ex} = 350nm$, $\lambda_{em} = 700nm$). (**c**) Absorption and PL(E) spectra of the near-IR Yb^{3+} emission ($\lambda_{ex} = 350nm$, $\lambda_{em} = 1000nm$).

transfer mechanism. We consider two possibilities for the energy transfer process: (1) After photoexcitation, the generated free exciton diffuses to an Yb^{3+} ion in the lattice and directly transfers its energy to the Yb^{3+} ion. (2) The free exciton becomes self-trapped and the STE transfers its energy to a nearby Yb^{3+} ion. Both possibilities have been suggested in the literature [16, 18, 19] for lanthanide doped elpasolite systems.

To investigate the nature of the emission pathways, we performed PL spectroscopy measurements at cryogenic temperatures on the undoped and 5% Yb^{3+}-doped $Cs_2AgBiBr_6$ NCs. **Figure 4.16 (a)** shows the emission spectra of $Cs_2AgBiBr_6$ nanocrystals at 4.3 K and at room temperature. The STE emission of $Cs_2AgBiBr_6$ at 4.3 K is significantly more intense than the emission at RT. The peak is narrower and blue shifted. The large increase in intensity at cryogenic temperatures shows that the STE emission is strongly quenched with increasing temperature. This quenching is due to thermal crossover of the STE state to the ground state. This quenching mechanism is shown in **figure 4.16 (b)**. At cryogenic temperatures, only the lowest vibrational levels are occupied, which has two effects: (1) Crossover to the ground state parabola does not occur as the wavefunctions of lowest vibrational levels of the excited state

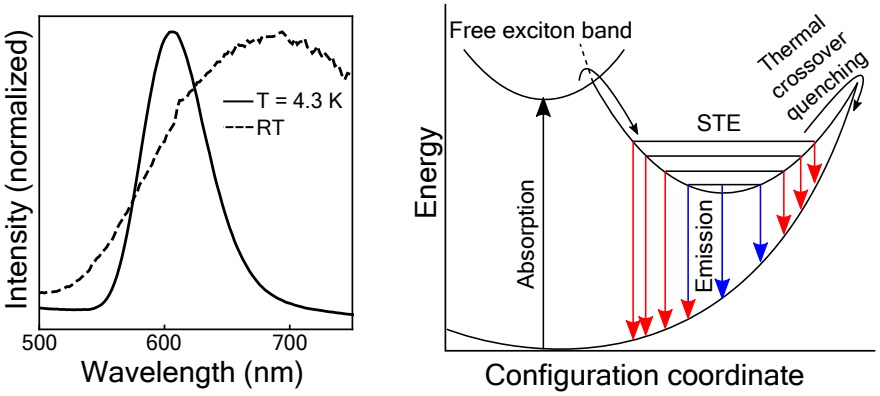

Figure 4.16: STE emission at cryogenic temperature. **(a)** Emission spectra of $Cs_2AgBiBr_6$ nanocrystals at 4 K and room temperature. **(b)** Configuration coordinate diagram showing thermal crossover quenching of the STE state and emission from the different vibrational levels.

do not overlap with the ground state wavefunctions. As a results, emission is not quenched. (2) Emission only occurs from the lowest vibrational states of the excited state, resulting in a relatively narrow emission peak, shown by the blue arrows. At higher temperatures, the higher vibrational states are populated and emission occurs from these states, indicated by the red arrows. This results in the broadening of the emission peak. Interestingly, at 4 K no free exciton recombination is observed. This indicates that the activation energy to go from the free exciton state to the STE state is extremely low. Possibly, the STE band in the configuration coordinate diagram overlaps with the free exciton state at its lowest vibrational level, so that crossover to the STE band always occurs.

Figure 4.17 presents the temperature dependents emission data of the undoped and 5% Yb^{3+}-doped nanocrystals. **Figure 4.17 (a)** and **(b)** show the temperature dependent emission and the area of the emission spectra with increasing temperature of the undoped $Cs_2AgBiBr_6$ nanocrystals. With increasing temperature, the emission intensity reduces significantly due to thermal quenching. A slight red shift of the emission is observed, as well as a slight broadening of the peaks. There is an abrupt decrease from the data point at 50 K due to the phase changes of residual oxygen and nitrogen present in the sample chamber of the cryostat, resulting in worse light transmission in these measurements.

Figures 4.17 (d,e,f) present the temperature dependent measurements of the Yb^{3+}-doped

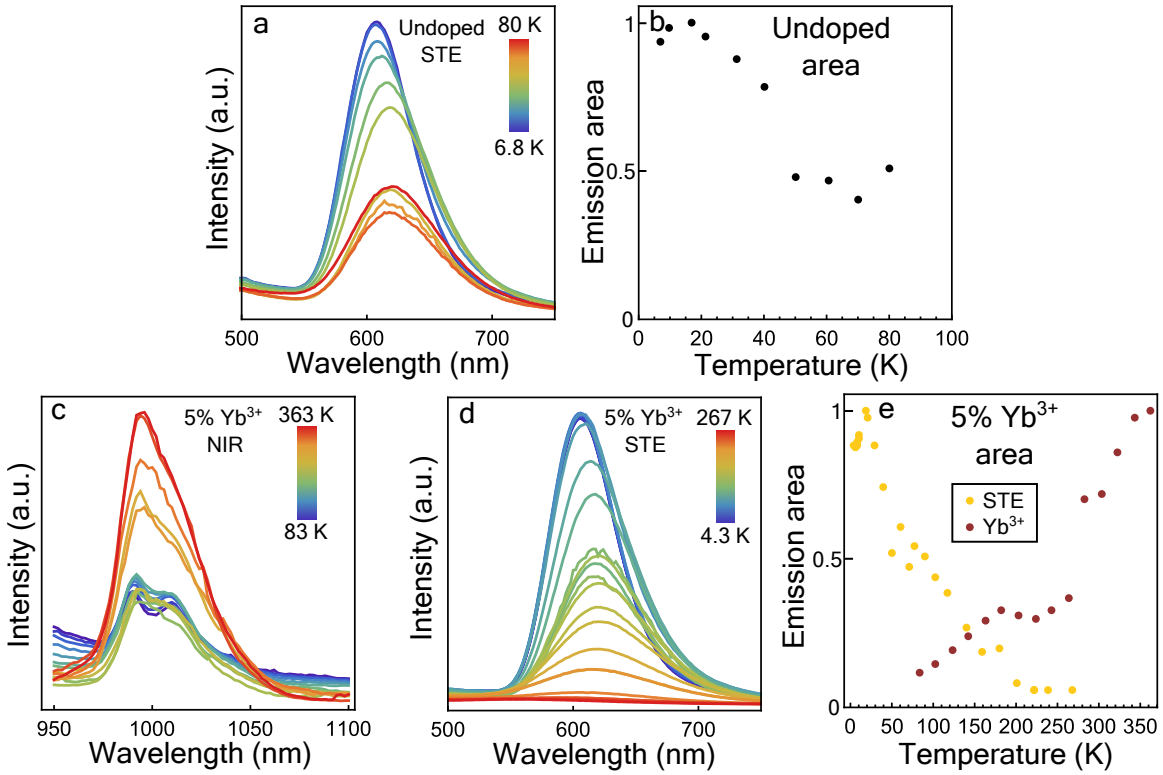

Figure 4.17: Temperature-dependent photoluminescence measurements of the undoped and Yb^{3+}-doped $Cs_2AgBiBr_6$ nanocrystals. **(a)** Temperature dependent emission spectra of the undoped $Cs_2AgBiBr_6$ nanocrystals. **(b)** Area of the temperature dependent emission of $Cs_2AgBiBr_6$ nanocrystals. **(c)** Temperature dependent emission spectra of the near-IR Yb^{3+} emission of the Yb^{3+}-doped $Cs_2AgBiBr_6$ nanocrystals. **(d)** Temperature dependent emission spectra of the STE emission of the Yb^{3+}-doped $Cs_2AgBiBr_6$ nanocrystals. **(e)** Area of the temperature dependent Yb^{3+} and STE emission of Yb^{3+}-doped $Cs_2AgBiBr_6$ nanocrystals. All emission was excited with 375 nm light

NCs. **(d)** and **(e)** show that the STE emission has similar temperature dependent behaviour to the emission of the undoped NCs. Surprisingly, the Yb^{3+} emission - shown in **figure 4.17 (c)** - increases when the temperature increases. This is contrary to what is expected if energy transfer occurs via the STE state. If the STE is an intermediate state in the energy transfer process, then the energy transfer to Yb^{3+} should also be hindered when the STE is strongly quenched. Thus, the current data suggest that energy transfer does not occur through the STE state. However more investigation is necessary to confirm this. The fact that the Yb^{3+} emission increases with temperature is an interesting observation itself. It suggests that the energy transfer process is thermally activated.

Schmitz *et al.* [18] have also doped $Cs_2AgBiBr_6$ with Yb^{3+} and they performed DFT calculation to calculate the configuration coordinate diagram of Yb^{3+} in the material. We can use their data to get a better understanding of the luminescence behaviour. **Figure 4.18** shows their calculation of the configuration coordinate diagram of an Yb ion in $Cs_2AgBiBr_6$. In this diagram, the bottom blue parabola represents the ground state of Yb^{3+} on a Bi^{3+} position. Upon excitation, Yb^{3+} is reduced to Yb^{2+} and a hole remains in the valence band, which is represented by the upper blue parabola. Additionally, we added the $^2F_{\frac{5}{2}}$ excited state of the Yb^{3+} center which is located at approximately 1.23 eV above the ground state ($^2F_{\frac{7}{2}}$). Using this diagram we can speculate about the luminescence mechanism of the Yb^{3+} emission. There is a charge transfer state representing Yb^{2+} accompanied by a hole in the valence band. This state can possibly be reached by the following: First, photoexcitation of an electron to the conduction band, creating an electron-hole pair expressed in the following:

$$\text{host}_{\text{groundstate}} + Yb^{3+} \xrightarrow{h\nu_{E>Eg}} e^-_{cb} + h^+_{vb} + Yb^{3+} \tag{4.1}$$

The charge carriers can travel freely through the material provided they do not get trapped.

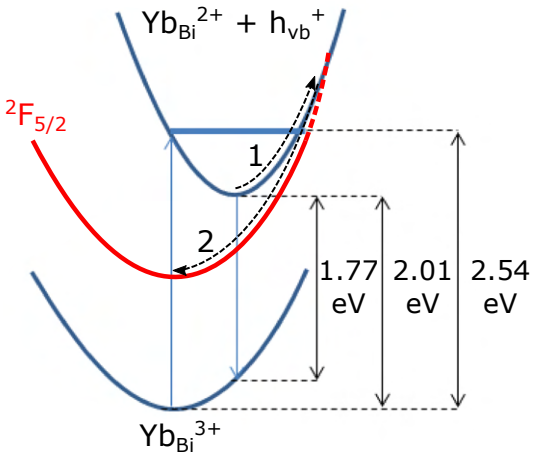

Figure 4.18: Configuration coordinate diagram of Yb^{3+} in $Cs_2AgBiBr_6$, adapted from Schmitz *et al.* [18]. The parabolas represent the states of an Yb ion on a Bi site in the crystal. The bottom blue parabola represent a Yb^{3+} ion in the ground state. The upper blue parabola represents a charge transfer state where Yb is reduced to oxidation state (II) accompanied by a hole in the valence band. In addition to the existing figure of Schmitz *et al.* [18], we overlaid the red parabola, which represents the $^2F_{\frac{5}{2}}$ excited state of Yb^{3+}, at around 1.23 eV (=1000 nm) above the ground state. Arrows 1 and 2 indicate the proposed crossover path from the Yb^{2+} charge transfer state to the Yb^{3+} $^2F_{\frac{5}{2}}$ excited state.

After this, the electron can get trapped on an Yb^{3+} center, reducing it to Yb^{2+}:

$$e^-_{cb} + h^+_{vb} + Yb^{3+} \longrightarrow h^+_{vb} + Yb^{2+} \tag{4.2}$$

Resulting in the charge transfer state displayed in **figure 4.18**. From this charge transfer state, the neutral excited state $^2F_{\frac{5}{2}}$ of Yb^{3+} is reached. Schmitz *et al.* [18] suggest that this mechanism occurs as follows "the activated Yb^-_{Bi} mainly rearranges to form the $F_{\frac{5}{2}}$ neutral excited state by releasing the trapped electron to the CB and decaying with the characteristic emission at 1.25 eV observed in the PL" [18]. However, we argue that this is not the case. In their explanation the electron is promoted back into the conduction band when the rearrangement to the $^2F_{\frac{5}{2}}$ state occurs, followed by relaxation of the $^2F_{\frac{5}{2}}$ state to emit the characteristic 1.25 eV light from Yb^{3+}:

$$h^+_{vb} + Yb^{2+} \longrightarrow e^-_{cb} + h^+_{vb} + Yb^{3+*}(F_{5/2}) \longrightarrow e^-_{cb} + h^+_{vb} + Yb^{3+}(F_{7/2}) + h\nu\,(1.25\,\mathrm{eV}) \tag{4.3}$$

However, it is clear from the equation that the host material is still in the excited state in this case. The 1.25 eV emission would essentially be created without requiring energy and the emission would be able to occur repeatedly without further photoexcitation, which is improbable. Instead, we propose that the rearrangement to the $^2F_{\frac{5}{2}}$ excited state occurs through thermal crossover of the $Yb^{2+} + h^+_{vb}$ charge transfer state to the $^2F_{\frac{5}{2}}$ excited state (represented by arrow 1 and 2 in **fig. 4.18**) caused by the recombination of the hole in the valence band with the Yb^{2+} center, followed by relaxation of the excited Yb^{3+} ion to the ground state configuration emitting 1.25 eV light:

$$h^+_{vb} + Yb^{2+} \longrightarrow Yb^{3+*}(F_{5/2}) + \mathrm{host}_{\mathrm{groundstate}} \longrightarrow Yb^{3+}(F_{7/2}) + h\nu\,(1.25\,\mathrm{eV}) + \mathrm{host}_{\mathrm{groundstate}} \tag{4.4}$$

This results in a full cycle of the emission mechanism. This mechanism does not directly confirm that the excitation of Yb occurs through the STE or the free exciton. However it can be argued that the free exciton case is more likely, since (1) the energy of the free exciton is higher (E_g = 2.38 eV according to indirect Tauc plot) than the partially relaxed STE (emission peak center at 1.77 eV), making it more likely to have sufficient energy to excite Yb to the charge transfer state, and (2) diffusion of e^-_{cb} and h^-_{vb} to an Yb center is more likely when the exciton is not trapped, and thus more mobile.

Figure 4.18 possibly explains the temperature dependent behaviour of the Yb^{3+} emission seen in Yb^{3+}-doped $Cs_2AgBiBr_6$ as well. As mentioned, the excitation to the $^2F_{\frac{5}{2}}$ state of Yb^{3+} happens through thermal crossover from the $Yb^{2+} + h^+_{vb}$ charge transfer state. Thermal crossover is a thermally activated process. Occupation of the higher phonon levels of the $Yb^{2+} + h^+_{vb}$ charge transfer state at higher temperatures results in an increase of thermal crossover to the $^2F_{\frac{5}{2}}$ state of Yb^{3+}. Resulting in an increased population of the $^2F_{\frac{5}{2}}$ state and thus increase in emission of the $^2F_{\frac{5}{2}} \longrightarrow {}^2F_{\frac{7}{2}}$ transition.

To investigate whether energy transfer occurs through the STE, we performed PL decay measurements on the undoped and 5% Yb^{3+}-doped nanocrystals. We can compare the PL decay plot of the STE emission of the undoped material and the Yb^{3+}-doped material. If energy transfer occurs via the STE, the STE will have an additional decay mechanism. This presents itself as a change in the shape of the decay curve, as well as a decrease of the lifetime of the emission.

Figure 4.19 presents the PL decay data of the undoped and 5% Yb^{3+}-doped nanocrystals. The temperature-dependent PL decay curves of the undoped nanocrystals (**fig. 4.19 (a)**) show a significant increase in PL decay rate with increasing temperature. The curves have a strong

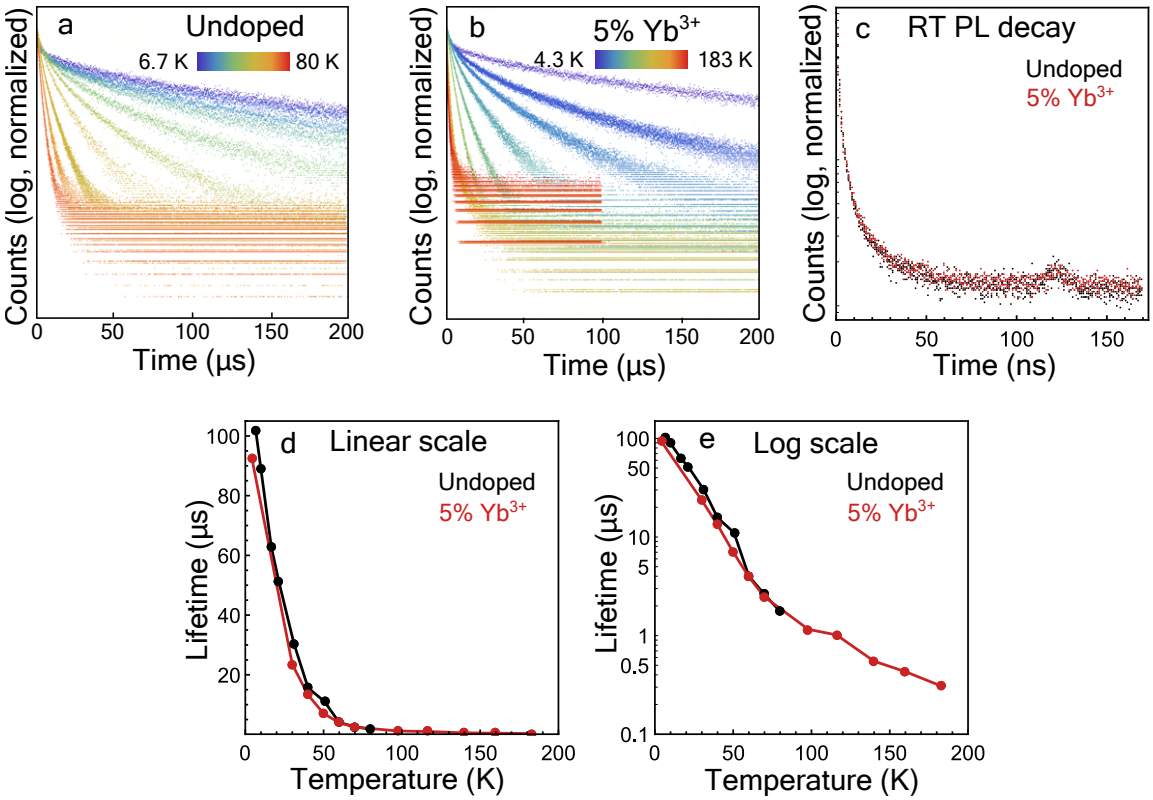

Figure 4.19: Luminescence decay data of undoped and 5% Yb^{3+}-doped $Cs_2AgBiBr_6$ nanocrystals. **(a)** Temperature-dependent PL decay of the undoped nanocrystals, measurements range from 6.7 K (blue) to 80 K (red). **(b)** Temperature-dependent PL decay of the 5% Yb^{3+}-doped nanocrystals, measurements range from 4.3 K (blue) to 183 K (red). PL decay measurements at cryogenic temperatures were permormed with a 375 nm laser with varying repetition rates. **(c)** Room temperature PL decay measurements ($\lambda_e x = 375nm$) with ns time resolution of the undoped (black) and 5% Yb^{3+}-doped (dark red) nanocrystals in short succession under identical measuring conditions. **(d,e)** Temperature-dependent lifetime of the undoped (black) and 5% Yb^{3+}-doped (dark red) nanocrystals on a linear scale **(d)** and a log scale **(e)**. Lifetimes were measured by fitting a triple exponential function with form: $f(t) = A_1 e^{-\frac{t}{\tau_1}} + A_2 e^{-\frac{t}{\tau_2}} + A_3 e^{-\frac{t}{\tau_3}} + C$, weighted averages of the lifetime were obtained with the formula: $\tau = \frac{A_1\tau_1 + A_2\tau_2 + A_3\tau_3}{A_1 + A_2 + A_3}$.

initial drop and have a curved descent after that. The decay curves are not linear on the log-scale, which indicates multi-exponential behaviour and thus multiple decay mechanisms. Based on our earlier findings, we assign the increase in decay with temperature to thermal crossover quenching of the STE. Due to the complexity of the decay curves, we use the weighted average lifetime of the decay for further analysis. This weighted average is calculated by:

$$\tau = \frac{A_1\tau_1 + A_2\tau_2 + A_3\tau_3}{A_1 + A_2 + A_3} \tag{4.5}$$

Where τ_n is the lifetime of the different components in the multi-exponential function and A_n is a pre-factor. When we look at the average lifetimes of the emission as a function of temperature (**fig. 4.19 (d,e)**) we see that the lifetimes are very similar. Thermal quenching already occurs at T < 10 K, since there already is a sharp decrease in lifetime at these temperatures. There seems to be a very small decrease in lifetime in the Yb^{3+}-doped nanocrystals compared to the undoped nanocrystals at various temperatures. However, when we look at the PL decay curves of the doped and undoped nanocrystals at room temperature under identical measuring conditions (**fig. 4.19 (f)**), the curves are practically identical. This strongly suggests that decay from the

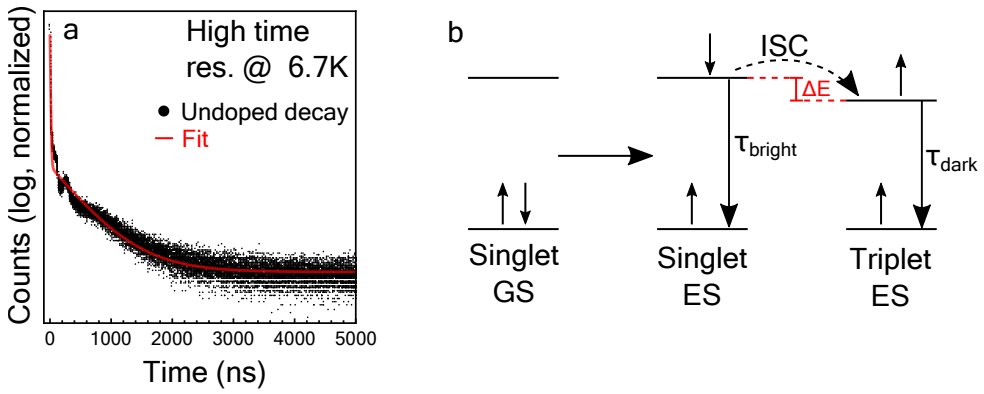

Figure 4.20: PL decay at cryogenic temperatures showing bright-dark state splitting. **(a)** PL decay curve with fit of the undoped nanocrystals at 6.7 K with higher time resolution. Fitted with a double exponential function: $f(t) = A_1 e^{-\frac{t}{\tau_1}} + A_2 e^{-\frac{t}{\tau_2}} + C$, results of the fit are a lifetime of 8.3 ns (short component) and 0.56 μs (long component). **(b)** Schematic showing singlet and triplet state involved in bright-dark state splitting

STE state is identical in the undoped and Yb^{3+}-doped nanocrystals, indicating that energy transfer does not occur via the STE. This confirms our previous observations that the energy transfer mechanism of host to Yb^{3+} does not involve the STE.

Figure 4.20 (a) shows the PL decay of the undoped nanocrystals at 6.7 K with higher time resolution. The sudden drops and rises in the initial part of the decay curve are artefacts caused by afterpulses of the photomultiplier tube used in the measurements. In this figure, a strong initial drop in the decay curve is visible. This initial drop only occurs in the decay curves up to about 50 K. This feature is possibly due to bright-dark state splitting. Bright-dark state splitting can occur in some materials at low temperatures. **Figure 4.20 (b)** shows schematically how bright-dark state splitting occurs. To explain further, when an electron is excited from a singlet ground state to a singlet excited state, the excited state can relax radiatively to the ground state. This relaxation is rapid as singlet-singlet transitions are spin allowed, therefore it has a very short lifetime (τ_{bright}) and is referred to as the bright state. However, the singlet excited state can also non-radiatively relax to a triplet excited state with slightly lower energy called intersystem crossing (ISC). Radiative decay from this triplet state is slow (long lifetime, τ_{dark}), because it involves a spin flip and thus is spin-forbidden. This state is referred to as the dark state. At higher temperatures, emission from the bright and dark state is indistinguishable, because the dark state can populate the bright state freely due to thermal energy ($kT > \Delta E$). However at low temperatures, thermal energy is very low - too low to populate the bright state from the dark state - and a splitting occurs: after excitation the bright state and the dark state are both populated, but now the dark cannot populate the bright so emission occurs from the bright and the dark state separately. This results in two radiative decay pathways, one with very short lifetime (τ_{bright}) and one with long lifetime (τ_{dark}). This presents itself in the PL decay curve as a sharp initial drop and a gradual decay after that. The fit procedure yields lifetimes of τ_{bright} = 8.3 ns and τ_{dark} = 0.56 μs.

Based on our observations we can try to construct a possible mechanism for the luminescence of $Cs_2AgBiBr_6$ doped with Yb^{3+}. The nanocrystals have a dual emission profile with a broad emission band centered around 700 nm originating from STE's and a sharp emission peak at 1000 nm originating from the Yb^{3+} dopant. Both emissions are excited in the host absorption

band. To sum up the findings about the Yb^{3+} emission:

- The Yb^{3+} emission originates from the $^2F_{\frac{5}{2}} \longrightarrow {}^2F_{\frac{7}{2}}$ transition of the Yb^{3+}. The excitation spectrum of the Yb^{3+} emission shows that it is excited in the host VB -> CB absorption bands.
- Temperature dependent PL measurements show that the Yb^{3+} emission increases with increasing temperature, while the STE emission is strongly quenched with increasing temperature. This suggests that Yb^{3+} emission is not excited by the STE.
- There is a Yb charge transfer state located within the band gap, which corresponds to Yb in oxidation state (II) accompanied by a hole in the valence band [18].
- Lifetime measurements show no significant reduction of STE lifetime when the nanocrystals are doped with Yb^{3+}, confirming the fact that Yb^{3+} is not sensitized by the STE.

Using these finding we propose a excitation mechanism for the Yb^{3+} emission. **Figure 4.21 (a)** presents an overview of the proposed mechanism of the Yb^{3+} emission. The process starts with absorption of a photon (step 1), promoting an electron from the VB to the CB (e^-_{cb}) of $Cs_2AgBiBr_6$ and leaving a hole behind in the VB (h^+_{vb}). The free e^-_{cb} and h^+_{vb} migrate through the material (step 2) until it encounters an Yb^{3+} center (alternatively it can become self-trapped due to lattice deformations). Then the electron can get trapped on an Yb center (step 3), reducing the Yb ion from oxidation state (III) to (II). Whether this reduction occurs is dependent on the Ln(II/III) reduction potential and may not occur for every lanthanide. The reduction potential for Yb(II/III) is relatively low and consequently the charge transfer state is located within the band gap of $Cs_2AgBiBr_6$ [18]. This charge transfer state can then non-radiatively relax to the

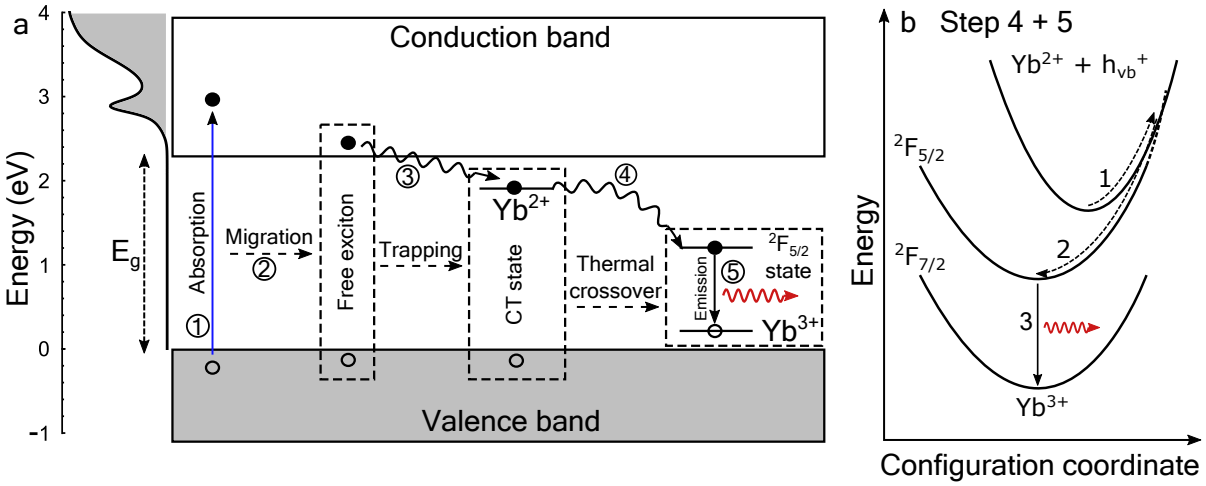

Figure 4.21: Overview of the emission mechanism of Yb^{3+}-doped $Cs_2AgBiBr_6$. **(a)** Step 1, absorption of a photon by the host material, creating an electron in the CB and a hole in the VB. Step 2, migration of the electron-hole pair through the material. Step 3, trapping of e^-_{cb} on an Yb center, reducing Yb^{3+} to Yb^{2+}. Step 4, relaxation of the $Yb^{2+} + h^+_{vb}$ CT state to the $^2F_{\frac{5}{2}}$ excited state of Yb^{3+}. Step 5, radiative relaxation of the $^2F_{\frac{5}{2}}$ excited state to the $^2F_{\frac{7}{2}}$ ground state of Yb^{3+}, emitting 1000 nm light. (b) The configuration coordinate diagram of an Yb center in $Cs_2AgBiBr_6$, arrow 1 and 2 indicate the thermal crossover of the $Yb^{2+} + h^+_{vb}$ CT state to the $^2F_{\frac{5}{2}}$ excited state of Yb^{3+}. Arrow 3 shows the $^2F_{5/2} \longrightarrow {}^2F_{7/2}$ transition of the Yb center, responsible for the 1000 nm emission.

$^2F_{\frac{5}{2}}$ excited state of Yb^{3+} (step 4). This step is best explained using the configuration coordinate diagram shown in **fig. 4.21 (b)**: After step 3, the system is in the Yb^{2+} + h_{vb}^+ charge transfer state located in the top right of the diagram. From this CT state, thermal crossover can occur to the $^2F_{\frac{5}{2}}$ excited state of Yb^{3+} indicated by arrow 1 and 2 in the diagram. In this process, h_{vb}^+ recombines with the Yb^{2+} ion, yielding the Yb^{3+} excited state. After this, the $^2F_{\frac{5}{2}}$ state can radiatively relax to the $^2F_{\frac{7}{2}}$ state - indicated by arrow 3 - resulting in the characteristic 1000 nm emission peak of Yb^{3+}. This step is also shown in **fig. 4.21 (a)** as step 5. This mechanism is often seen in wide band gap phosphors and scintillators [52, 53]. Considering the fact that Yb^{3+} is excited by free excitons in this material, it is plausible that the energy transfer follows this mechanism. However, more investigation is needed to exclude the possibilities of intermediate states aiding in the energy transfer process.

4.1.3 $Cs_2NaBi_xEu_{1-x}Cl_6$ microcrystals

We now know that the STE is not involved in the energy transfer mechanism of our elpasolite semiconductor host to lanthanide, at least in the case of Yb^{3+}. Consequently, that means we do not need STE emission in order for energy transfer to occur. In fact, since it is a competitive process between self-trapping and energy transfer, it might even be undesirable to have self-trapping of excitons. Therefore we investigate a new compound in this section: $Cs_2NaBiCl_6$. In the previously discussed materials, the STE's originated from trapping of holes on $[AgCl_6]^{5-}$ octahedra. Therefore, if we substitute Ag^+ for Na^+, we might reduce self-trapping. This seems to be the case, as in previous reports only very weak host emission was found from $Cs_2NaBiCl_6$ [54]. The material has a larger band gap than $Cs_2AgBiCl_6$ though. In $Cs_2AgBiCl_6$, the 4d orbitals of Ag^+ contributed significantly to the valence band maximum. The valence orbitals of Na^+ are the 2p orbitals, which are located a lot deeper into the valence band and barely contribute to the valence band maximum [54].

To investigate the potential for Eu^{3+} doping we synthesized a series of $Cs_2NaBiCl_6$ microcrystals in which we gradually substitute Bi^{3+} for Eu^{3+} ($Cs_2NaBi_xEu_{1-x}Cl_6$, x = 0, 0.25, 0.5, 0.75, 1). We chose to synthesize microcrystals because the microcrystal synthesis is a more robust way of incorporating Eu^{3+} into the crystal compared to the nanocrystal synthesis. We investigate whether the crystal structure is stable when Bi^{3+} and Eu^{3+} are mixed and by making a series of $Cs_2NaBi_xEu_{1-x}Cl_6$ microcrystals we aim to see when Eu^{3+} emission ($Cs_2NaEuCl_6$ shows Eu^{3+} luminescence due to f-f transitions [55]) or host emission appears and if the emission is excited in the same absorption band.

To investigate the structural properties of the microcrystal series we performed XRD measurements. **Figure 4.22** presents the XRD measurements of the $Cs_2NaBi_xEu_{1-x}Cl_6$ microcrystals. All the samples agree with the reference diffractograms well. They are some very minor impurity peaks due to CsCl (red arrow) and NaCl (blue arrow). The black arrows indicate the diffraction

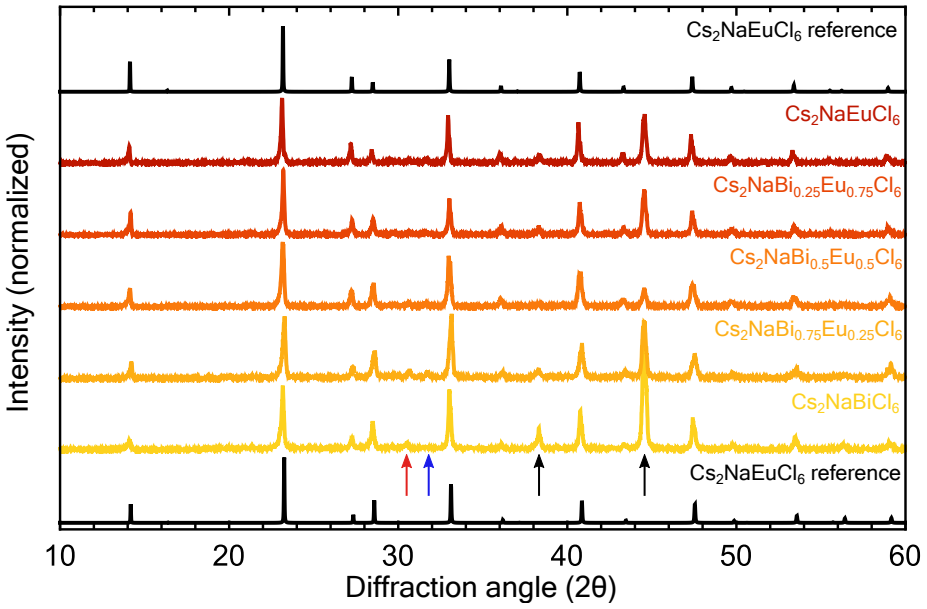

Figure 4.22: X-ray diffraction data of the $Cs_2NaBi_xEu_{1-x}Cl_6$ microcrystals series. Red arrow indicates reflection peak of CsCl, blue arrow indicates reflection peak of NaCl, black arrow indicate reflection peaks of aluminium sample holder.

peaks of Al metal, which are present due to the aluminium sample holder. Surprisingly, there is no shift in diffraction angle upon substitution with Eu^{3+}. This indicates that the Bi^{3+} and Eu^{3+} ions have an identical radius in this crystal lattice, even though the ionic radius in sixfold coordination of Eu^{3+} is smaller (0.947 Å) than Bi^{3+} (1.03 Å). A possible explanation is the following [56]: The effective radius of Bi^{3+} is smaller in a crystal with a perfectly symmetrical octahedral environment. This is likely due to the $6s^2$ electron pair of Bi^{3+}. Because of the perfectly symmetrical environment, the $6s^2$ electron pair is forced into a diffuse antibonding s-orbital. The bismuth ion is effectively lacking two electrons, making the ion smaller and the bond lengths shorter. Since the antibonding s-orbital is so diffuse due to the large size of Bi^{3+}, it does not interact much with the surroundings, so it affects the bond lengths very weakly. Combined, this results in an effectively smaller Bi^{3+} ion in the lattice. Regardless, the XRD measurements show the elpasolite structure is formed, although with minor amounts of CsCl and NaCl impurities.

To investigate the optical properties of the microcrystal series, we performed PL spectroscopy. **Figure 4.23** presents the optical data for of the $Cs_2NaBi_xEu_{1-x}Cl_6$ microcrystal series. The emission spectra **(a)** show sharp emission lines at several wavelengths for all samples except for the 100% Bi^{3+} sample. The emission intensity increases from 0 to 25% Bi^{3+} incorporation, after that it decreases the more Eu^{3+} is substituted for Bi^{3+}. The sharp emission lines are due to the f-f transitions of Eu^{3+}. Usually, the $^5D_0 \longrightarrow {}^7F_2$ transition at 615 nm is the most intense of the Eu^{3+} transitions. However, in this case the $^5D_0 \longrightarrow {}^7F_1$ transition at 593 nm is the most intense. When Eu^{3+} is in a crystal site with inversion symmetry, only transitions that are magnetic dipole transitions are allowed. The electronic dipole transitions are strongly forbidden [55]. The $^5D_0 \longrightarrow {}^7F_2$ transition of Eu^{3+} is an electric dipole transition and therefore, the emission at 615 nm is weaker than the emission at 593 nm. Despite the transition being forbidden, vibronic transitions can still occur resulting in a spectrum built of vibronic bands. Interestingly, the Eu^{3+} emission is present in the sample with 100% Eu^{3+}. This indicates that concentration quenching of the Eu^{3+} emission is not an issue. The intensity of the emission does seem to increase when reducing the Eu^{3+} content from 100% to 75%, so there is possibly some concentration quenching in the pure Eu^{3+} crystal. The excitation spectrum **(b)** monitored at emission wavelength 615 nm shows sharp excitation lines and a broad band at around 300-320 nm in the samples with Eu^{3+}.

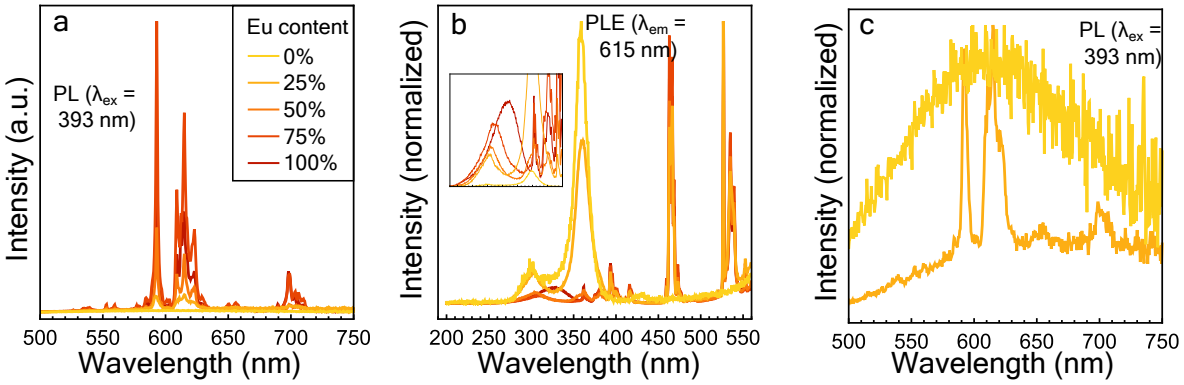

Figure 4.23: Optical data of the $Cs_2NaBi_xEu_{1-x}Cl_6$ (x = 0, 0.25, 0.5, 0.75, 1) microcrystals series. **(a)** PL spectra of the microcrystals, directly exciting Eu^{3+} at 393 nm ($^7F_0 \longrightarrow {}^5L_7$). **(b)** Excitation spectra of the nanocrystals, monitoring at emission wavelength 615 nm. **(c)** broad emission from the samples with 75% and 100% Bi^{3+}.

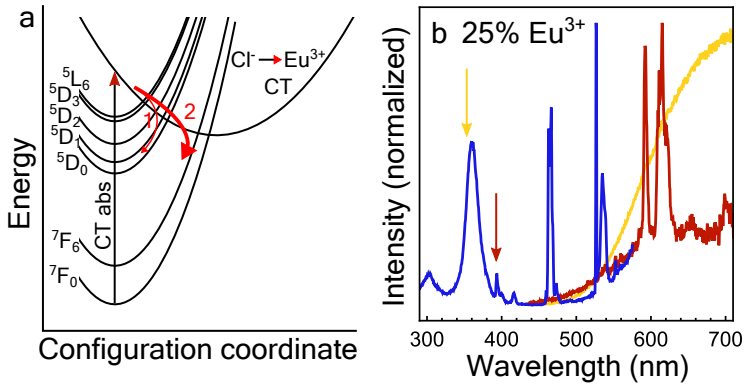

Figure 4.24: (a) Configuration coordinate diagram showing a possible scenario for the quenching of the CT state. Thickness of the arrows give an indication of the rate of occurrence. Some of the ^7F_N levels are not shown for simplicity. **(b)** PL spectra of the 25% Eu^{3+} sample, exciting Eu^{3+} directly and exciting into the host absorption band.

The samples with 75% and 100% Bi^{3+} show a broad excitation band centered around 360 nm. The sharp excitation lines originate from the f-f transitions of Eu^{3+}. The broad band at 300-320 nm could possibly be a $Cl^- \longrightarrow Eu^{3+}$ charge transfer absorption band (magnified in the inset), however these are usually significantly stronger as they are fully allowed transitions. Possibly, the CT state is partially quenched, i.e., the CT state has significant overlap with the ground state, as shown in **figure 4.24 (a)**. Excitation into the CT band would result in relaxation to the ^5D_N levels of Eu^{3+} (arrow 1) followed by emission, or relaxation to the ^7F_N levels (arrow 2), resulting in quenching. The position of this CT band would also explain why the $^7F_0 \longrightarrow {}^5L_7$ excitation peak (393 nm) is very weak. When exciting into the $^5L_7$ level, the excited state can crossover to the CT state followed by crossover to the ground state, resulting in quenching. The transitions $^7F_0 \longrightarrow {}^5D_1$ (530 nm) and $^7F_0 \longrightarrow {}^5D_2$ (470 nm) are more intense, because the crossover point to the CT state is located significantly higher, so less quenching is expected. The $^7F_0 \longrightarrow {}^5D_0$ (>560 nm) is often not visible at all because this transition is strongly forbidden ($\Delta J = 0$, J and J' both zero). Regarding the broad excitation band at 360 nm of the 75% and 100% Bi^{3+} samples, exciting in this band results in a weak broad emission similar to the emission shown in **figure 4.23 (c)**. The fact that the broad emission only shows up in samples with >75% Bi^{3+} and not in samples with low amounts of Bi^{3+} indicates that this emission cannot be due to a localized Bi^{3+} transition. The broad emission is very similar to the emission of $Cs_2AgBiCl_6$ suggesting that it might be STE emission as well, which is also what other reports found [57].

Our findings indicate that there seems to be some emission as a result of the generation of excitons in samples containing more than 75% Bi^{3+}. In the 75% Bi^{3+} sample also some Eu^{3+} emission is present, so it is interesting to investigate whether the Eu^{3+} is excited in the broad absorption band at 360 nm. **Figure 4.24 (b)** shows the emission spectra of the sample containing 75% Bi^{3+}, while directly exciting Eu^{3+} and exciting in the host absorption band. When directly exciting Eu^{3+} we see characteristic Eu^{3+} emission lines and background host emission. However when exciting in the host absorption band, no Eu^{3+} is detected and only STE emission is observed. Therefore, it seems that energy transfer does not occur from the host to Eu^{3+}.

Summarizing our results for $Cs_2NaBiCl_6$, we found that incorporation of Eu^{3+} into $Cs_2NaBiCl_6$ is possible and Eu^{3+} incorporation leads to characteristic Eu^{3+} emission lines. However, the Eu^{3+}

emission is not excited in the host absorption band.

4.1.4 $Cs_2NaBiBr_6$

The next crystal we investigate is $Cs_2NaBiBr_6$. We have seen incorporation of Eu^{3+} into $Cs_2NaBiCl_6$ gives rise to characteristic Eu^{3+} emission, which is not excited in the host absorption band. We now investigate whether this is the case for $Cs_2NaBiBr_6$. The measurements on $Cs_2NaBiCl_6$ show that Eu^{3+} can substitute Bi^{3+} in the lattice well. Therefore, we synthesize the nanocrystals of $Cs_2NaBiBr_6$ to keep in mind our wishes to create a nanocrystalline phosphor. The synthesis we use for the nanocrystals is based on the procedure of Creutz *et al.* [39] with the modification that we substitute CH_3COOAg for CH_3COONa.

To investigate the structural properties of the synthesized undoped and 10% Eu^{3+}-doped $Cs_2NaBiBr_6$ nanocrystals we performed XRD and TEM measurements. **Figure 4.25** presents the structural data of the undoped and 10% Eu^{3+}-doped $Cs_2NaBiBr_6$ nanocrystals. The XRD patterns **(a)** show good agreement with the reference XRD pattern, although the peaks are significantly broader. There seems to be a small sharp peak at 33 2θ due to an unknown impurity. The TEM image of the undoped nanocrystals **(b)** shows nanocrystals with varying shapes and sizes. Small nanocrystals have cubic shapes and larger crystals are more round. Compared to $Cs_2AgBiBr_6$ nanocrystals, they are significantly less monodisperse. The same is true for the Eu^{3+}-doped nanocrystals **(c)**. In this TEM image, the cubic nanocrystals are more visible. This synthesis procedure seems to work better for the cesium silver bismuth halide nanocrystals than for $Cs_2NaBiBr_6$ nanocrystals, although the product is relatively phase pure.

We used PL spectroscopy to study the optical properties of the undoped and 10% Eu^{3+}-doped $Cs_2NaBiBr_6$ nanocrystals. **Figure 4.26** presents the optical data for the nanocrystals. The absorption spectra in **figure 4.26 (a)** has an intense band centered around 390 nm. This band is due to the first direct band gap transition of $Cs_2NaBiBr_6$. The Tauc plot **(c)** shows that the direct band gap has an energy of 3.14 eV. There also is an indirect band gap at lower energies, however this crystal has relatively flat bands, so the first direct and indirect transitions are very close in energy [58]. When we look at the PL spectra, we see that in both the undoped **(a)** and 10% Eu^{3+}-doped **(b)** nanocrystals a tail of an emission is present from 450 nm onwards. This emission does not originate from the nanocrystals itself but is due to degraded ligands. At the high temperatures of the hot injection reaction, oleic acid and oleylamine can react to form various compound which show blue fluorescence. This fluorescence is excited at short

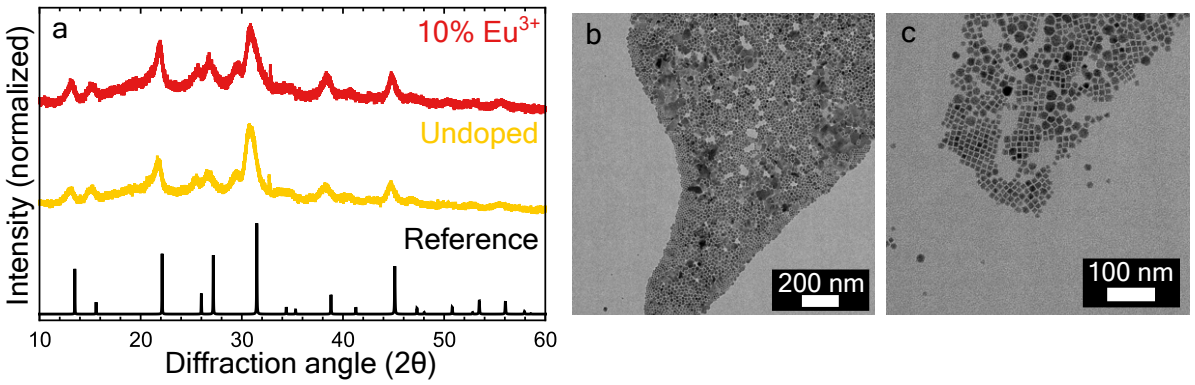

Figure 4.25: Structural data of the undoped and Eu^{3+}-doped $Cs_2NaBiBr_6$ nanocrystals. **(a)** XRD patterns of the Eu^{3+}-doped (top) and undoped (middle) nanocrystals with reference XRD pattern (bottom). **(b,c)** TEM images of the undoped nanocrystals **(b)** and the Eu^{3+}-doped nanocrystals **(c)**.

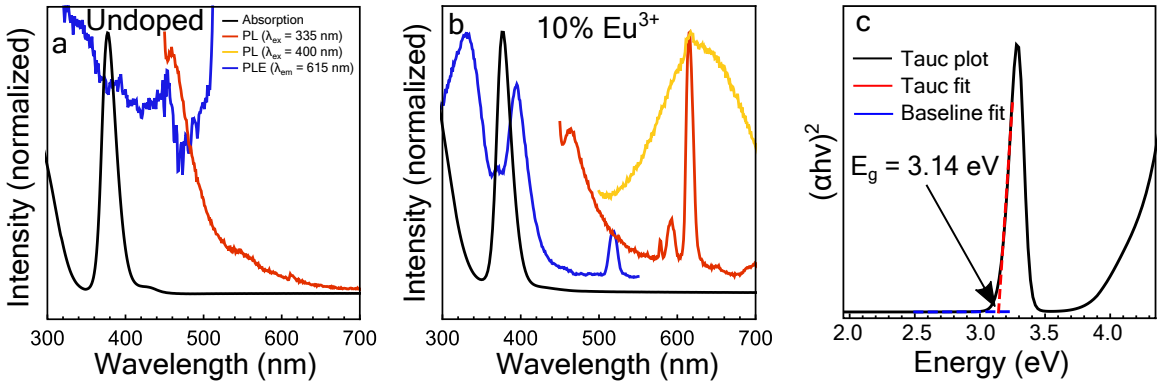

Figure 4.26: Optical data of the undoped and 10% Eu^{3+}-doped nanocrystals. **(a)** Absorption, PL and PLE of the undoped nanocrystals. **(b)** Absorption, PL and PLE of the 10% Eu^{3+}-doped nanocrystals. **(a)** Tauc plot of the absorption spectrum of $Cs_2NaBiBr_6$ in direct mode, fit results in a direct band gap of 3.14 eV.

wavelengths around 300 nm and results in a excitation wavelength dependent UV to blue emission that looks the tail seen in the emission spectra [59]. The Eu^{3+}-doped compound shows sharp emission peaks due to Eu^{3+} f-f transitions. Peculiarly, the Eu^{3+}-doped sample shows a broad emission band originating from STE's when exciting at 400 nm, while the undoped nanocrystals do not show this emission band. When an excitation spectrum is measured while monitoring emission wavelength 615 nm, the undoped compound mostly shows noise. The Eu^{3+}-doped sample shows three distinct bands, one centered around 400 nm, one centered around 335 nm and a small peak at 510 nm. The small peak at 510 nm is a Raman peak, as it shifts with varying excitation wavelength. When exciting in the 335 nm band, the Eu^{3+} emission shown in **(b)** arises. When exciting in the 400 nm band, the STE emission band arises. This is the first sign that the Eu^{3+} emission is not excited in the host material. The attentive reader will have noticed that contrary to the Eu^{3+} emission in $Cs_2NaBiCl_6$, the most intense Eu^{3+} emission peak is from the $^5D_0 \longrightarrow {}^7F_2$ transition at 615 nm. This suggest that the emitting Eu^{3+} ion is not located in a site with inversion symmetry. The question is now whether the Eu^{3+} emission originates from the crystals at all. The answer lies in **figure 4.27**. This figure shows the PL spectra after 20 days. In the excitation spectrum, the absorption band at 400 nm has faded. Exciting in this band lead to STE emission. The STE emission is not present anymore in the sample after 20 days. This suggests that the sample has degraded. However, the Eu^{3+} emission

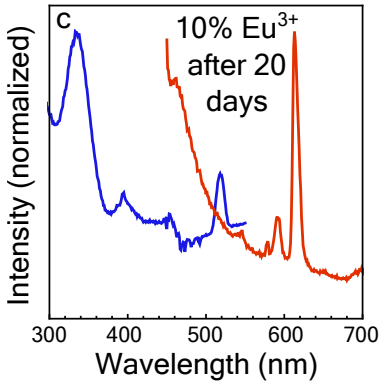

Figure 4.27: PL and PLE spectra of the 10% Eu^{3+}-doped $Cs_2NaBiBr_6$ nanocrystals after 20 days in ambient conditions.

is still present. This indicates that the Eu^{3+} emission does not originate from the nanocrystals. Probably, the emission originates from Eu^{3+} which is in a complex in solution. This also explains why the Eu^{3+} site does not have inversion symmetry. The broad absorption band at 335 nm is possibly a ligand-to-metal charge transfer absorption band from one of the complexated ligands to the Eu^{3+} ion. In short, the synthesized $Cs_2NaBiBr_6$ nanocrystals show STE emission, although the crystals seem to be very unstable. Eu^{3+} only seems to be present from complexated Eu^{3+} ions in solution.

4.2 Indium-based elpasolite materials

In this section we discuss the elpasolite crystal systems based on indium. There are a few important differences between elpasolites with In^{3+} and Bi^{3+}. Structurally, both occupy the same site in the crystal structure. In^{3+} has a smaller ionic radius (0.8 Å) than Bi^{3+} (1.03 Å). This might make lanthanide incorporation slightly more difficult, but reports show that it is possible [16].

The most important differences are electronic. Contrary to Bi^{3+}, the In^{3+}-based elpasolite semiconductors usually have a direct band gap. The first band gap transitions are often parity forbidden and have weak absorption [60, 61]. Due to the forbidden nature of the lowest energy transition, the lifetime of charge carriers is quite long and luminescence is very weak and originates from STE's. **Figure 4.28** shows the change of band structure when substituting Bi^{3+} for In^{3+} in Cs_2AgMBr_6 (M = Bi^{3+}, In^{3+}) [62]. We see that substitution of Bi^{3+} with In^{3+} changes the band gap from indirect to direct. In the pure indium compound, the lowest conduction band is made up completely by delocalized In 5s orbitals. The band is highly dispersive so high electron mobility is expected, which might be beneficial for energy transfer. The valence band maximum is made up of Ag 4d orbitals and Br 4p orbitals.Contrary to Bi^{3+}, In^{3+} has no contribution to the valence band maximum, because the In 4d orbitals are located deep in the valence band. This effectively results in a lower lying VBM and CBM. A lower VBM might cause less charge transfer quenching. When the VBM lies lower, the $Eu^{2+} + h_{vb}^{+}$ CT state effectively lies in a higher position within the band gap, shown in **figure 4.29**. The higher position of the CT band causes less CT quenching, because crossover to the CT state and CT state to ground state requires more energy. Therefore, indium based elpasolite semiconductors are interesting to investigate for lanthanide doping. In fact, reports have shown that doping $Cs_2AgInCl_6$ nanocrystals with Tb^{3+} results in host sensitized Tb^{3+} emission [16]. In this section, we inves-

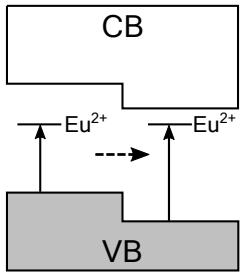

Figure 4.29: Simplified schematic showing the change in position of the Eu^{2+} state within the band gap.

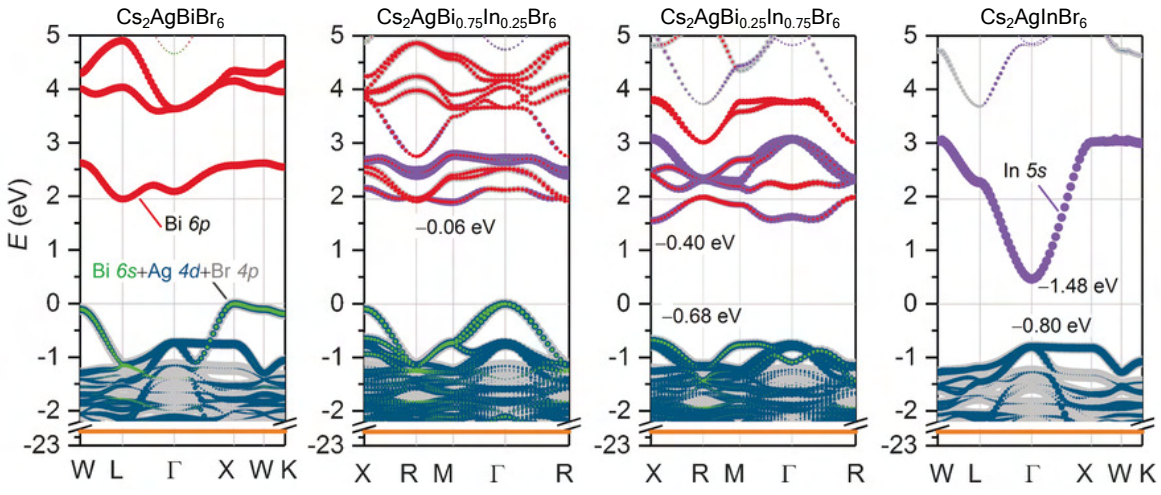

Figure 4.28: Band structures of the elpasolite semiconductors $Cs_2AgBiBr_6$ and $Cs_2AgInBr_6$ and In/Bi alloyed intermediates.

tigate mainly investigate the elpasolites $Cs_2AgInCl_6$ and Cs_3InCl_6 and attempt doping with various lanthanides.

4.2.1 $Cs_2AgInCl_6$

The first Indium based elpasolite we briefly discuss is $Cs_2AgInCl_6$. We attempted doping this material Eu^{3+} as a proof of concept. In $Cs_2AgBiCl_6$, the Eu^{3+} PL is fully quenched due to CT quenching. If lowering the VBM by substituting Bi^{3+} for In^{3+} results in less CT quenching, we might be able to see Eu^{3+} emission in Eu^{3+}-doped $Cs_2AgInCl_6$. This would substantiate our claims that indium compounds experience less CT quenching. Therefore, we synthesize $Cs_2AgInCl_6$ microcrystals with 10% Eu^{3+} doping. The synthesis is based on the synthesis procedure of Volonakis *et al.* [41], in which we partially substitute $InCl_3$ for $EuCl_3 \cdot 6\,H_2O$. The synthesis is a simple precipitation reaction from a concentrated HCl solution, details found in the experimental section.

We performed XRD measurements to investigate the structural properties of the Eu^{3+}-doped $Cs_2AgInCl_6$ microcrystals. **Figure 4.30 (a)** shows the XRD pattern of the synthesized material with a reference pattern of $Cs_2AgInCl_6$. The experimental pattern shows good agreement with the reference XRD pattern. The pattern shows two broad peaks at lower diffraction angles which are from the sample holder. The XRD measurements confirm that the synthesized Eu^{3+}-doped $Cs_2AgInCl_6$ microcrystals are phase pure.

To investigate the PL properties of the Eu^{3+}-doped $Cs_2AgInCl_6$ microcrystals, we performed PL spectroscopy. **Figure 4.30** shows the emission and excitation spectra of the Eu^{3+}-doped $Cs_2AgInCl_6$ microcrystals. The emission spectrum with excitation wavelength 370 nm shows a broad band centered around 590 nm with a large Stokes shift. When exciting at 393 nm, the emission spectrum also shows this broad band and additionally sharp peaks at 590, 615 and 700 nm. The excitation spectrum of the broad emission monitored at 570 nm consists of a single band centered around 370 nm. When measuring the excitation spectrum of the sharp emission, an almost identical spectrum is obtained. Like in the silver bismuth halide elpasolite, the broad emission originates from STE's that are caused by hole-trapping on $[AgCl_6]^{5-}$ octahedra [60]. The sharp peaks in the emission spectrum excited at 393 nm are the emission peaks of the Eu^{3+} dopant. The Eu^{3+} emission is only observed when exciting Eu^{3+} directly at 393 nm. Therefore it seems that Eu^{3+} is not excited in the host absorption band and thus no energy transfer occurs.

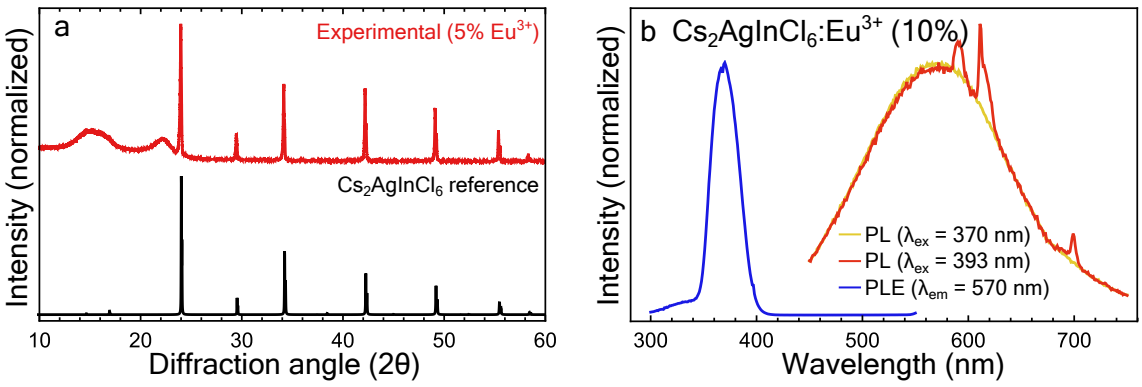

Figure 4.30: Analysis data of the 5% Eu^{3+}-doped $Cs_2AgInCl_6$ microcrystals. **(a)** XRD pattern of the synthesized microcrystals (top) with a calculated reference (bottom). **(b)** PL(E) spectra of the microcrystals.

However, contrary to $Cs_2AgBiCl_6$, we do see Eu^{3+} emission in $Cs_2AgInCl_6$. This indicates that substitution of Bi^{3+} by In^{3+} results in less charge transfer quenching. The emission of Eu^{3+} is quite weak though, so it is still strongly quenched. Nevertheless, it supports our hypothesis that substitution of Bi^{3+} for In^{3+} results in less charge transfer quenching due to lowering the VBM.

4.2.2 Cs_3InCl_6

The next material we investigate is Cs_3InCl_6. We have seen that substituting Bi^{3+} for In^{3+} results in less charge transfer quenching. If it is the case that a lower VBM leads to less quenching, we can also substitute other ions to lower the VBM. The Ag^+ 4d orbitals contribute significantly to the VBM in $Cs_2AgInCl_6$. Consequently, substitution of Ag^+ for an ion with lower lying valence orbitals should lower the VBM. The ion we investigate for substitution in this section is Cs^+. Since the 5p orbitals of Cs^+ are very stable, they should be located deeper in the valence band. This should lower the VBM even further. This has the added effect of increasing the band gap energy though.

We first attempted synthesizing Cs_3InCl_6 microcrystals doped with 10% Eu^{3+} using preparation E of Morss *et al.* [40]. We investigated the structural properties of the synthesized microcrystals with XRD. The result of the XRD measurement is shown in **figure 4.31 (a)**. The XRD pattern shows that the Cs_3InCl_6 crystal is not formed, but rather a hydrated cesium indium chloride crystal with chemical formula $Cs_2InCl_5 \cdot H_2O$, shown in **figure 4.31 (b)**. It seems that a synthesis performed in an aqueous medium results in a hydrated crystal. This means that the synthesis procedure of Morss *et al.* [40] is not suitable for the synthesis of Cs_3InCl_6 microcrystals.

Despite the failed synthesis of Cs_3InCl_6, it is still interesting to study the properties of the hydrated crystal. We performed PL spectroscopy to study the luminescence properties of the Eu^{3+}-doped $Cs_2InCl_5 \cdot H_2O$ microcrystals. **Figure 4.32** presents the results of the PL spectroscopy measurements. The emission spectrum of the Eu^{3+}-doped microcrystals **(a)** shows sharp peaks from Eu^{3+} f-f transitions. the excitation spectrum shows the typical excitation lines of Eu^{3+}. The Eu^{3+} emission is quite intense, compared to our previously investigated materials.

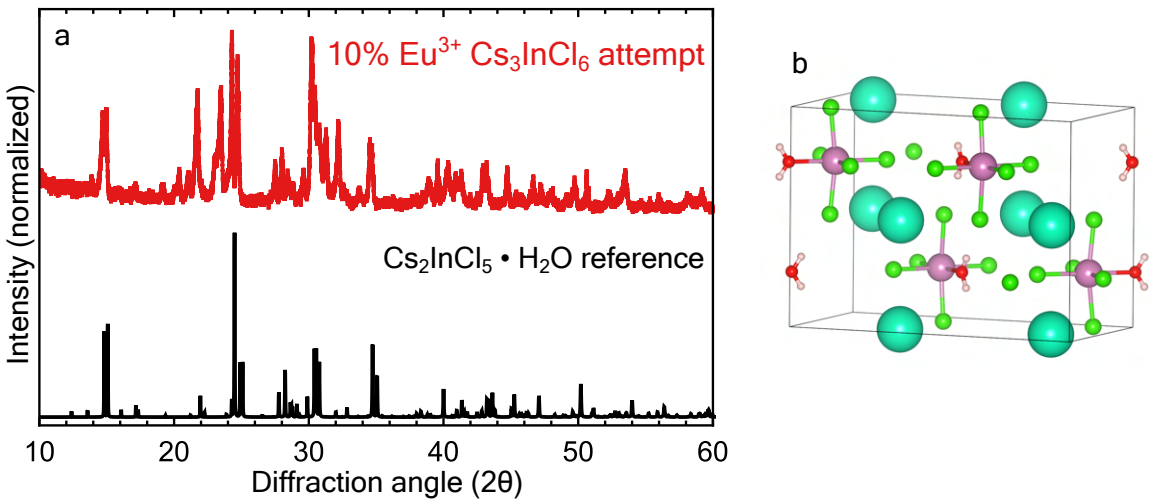

Figure 4.31: Structural data of the synthesized nanocrystals using preparation E of Morss *et al.* [40]. **(a)** XRD pattern of the synthesized microcrystals with reference pattern of $Cs_2InCl_5 \cdot H_2O$. **(b)** Crystal structure of the hydrated cesium indium chloride crystal.

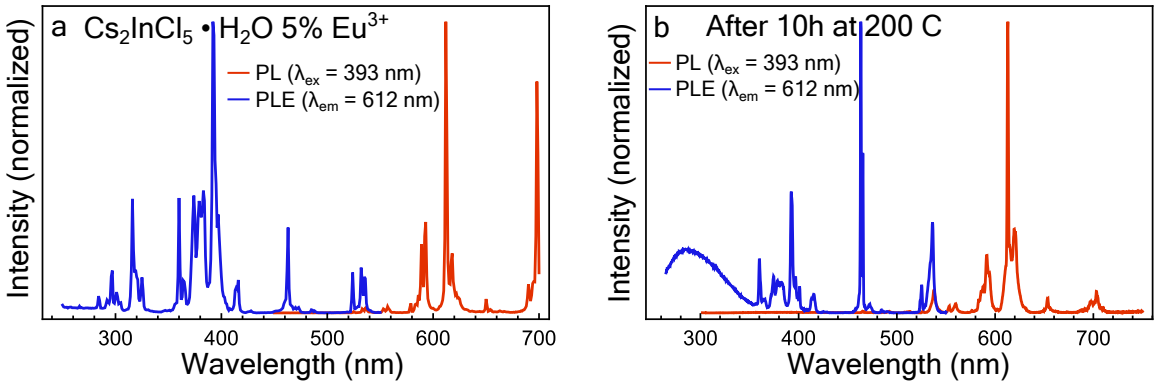

Figure 4.32: PL spectroscopy results of the synthesized hydrated microcrystals. **(a)** PL(E) spectra of the fresh sample. **(b)** PL spectra after heating the sample.

The material does not have any intrinsic host emission. It seems that Eu^{3+} is incorporated into the crystal quite well. The effect of the non-centrosymmetric environment of the Eu^{3+} ions is immediately clear, since the emission due to the $^5D_0 \longrightarrow {}^7F_2$ transition is by far the most intense. Regardless of the failed synthesis attempt, Eu^{3+} doping in the hydrated crystal $Cs_2InCl_5 \cdot H_2O$ gives rise to quite intense Eu^{3+} emission.

We also investigated the PL properties of the microcrystals after heating the sample to 200 °C for 10 hours. This heating step was performed to see if the crystal dehydrates at higher temperatures. **Figure 4.32 (b)** shows the PL spectra of the crystals after this heating step. The emission spectrum shows similar emission peaks from Eu^{3+}. Interestingly, a broad band appears around 300 nm in the excitation spectrum after heating the sample. Heating the sample seems to have changed the crystal, suggesting that dehydration might occur.

Since the synthesis procedure of Morss *et al.* [40] does not produce the desired crystal phase, we performed an alternative synthesis. This synthesis is based on a procedure from Meyer [42]. It is a solid state reaction performed in an evacuated quartz tube. The procedure was performed under water free conditions to prevent the formation of the hydrated crystal.

To investigate the structural properties of the synthesized Cs_3InCl_6 microcrystals we performed XRD measurements. The results of the XRD measurements are presented in **figure 4.33**. We first synthesized the Eu^{3+}-doped microcrystals. The XRD pattern of the Eu^{3+}-doped microcrystals agree well with the reference XRD pattern with no impurity peaks present. Following this observation, we also synthesized Cs_3InCl_6 doped with 5% Tb^{3+}, Yb^{3+} and the undoped crystal. These XRD patterns are also shown in the figure. None of the samples with lanthanide doping have impurities present judging from the XRD patterns. The pattern of the undoped microcrystals has additional peaks, which match with the reference pattern of CsCl. No $InCl_3$ impurities are present, so possibly the amount of precursors added was measured incorrectly in this sample. Some CsCl impurity should not be detrimental to the PL properties of the sample. The diffraction angle of the reflection peaks shifts to slightly lower values upon doping with Eu^{3+} and Yb^{3+}. This indicates that incorporation of Eu^{3+} and Yb^{3+} causes a lattice expansion of the crystal, which is expected as the ionic radii of Eu^{3+} (0.95 Å) and Yb^{3+} (0.87 Å) are larger than In^{3+} (0.80 Å). This shift of the diffraction angle is a good indication that the lanthanides are incorporated into the crystal structure. Surprisingly, the sample with Tb^{3+} does not show a shift in diffraction angle even though Tb^{3+} (0.92 Å) has a significantly larger ionic radius than In^{3+}. It is possible that Tb^{3+} is not incorporated into the lattice as well as Eu^{3+} and Yb^{3+}. Nevertheless,

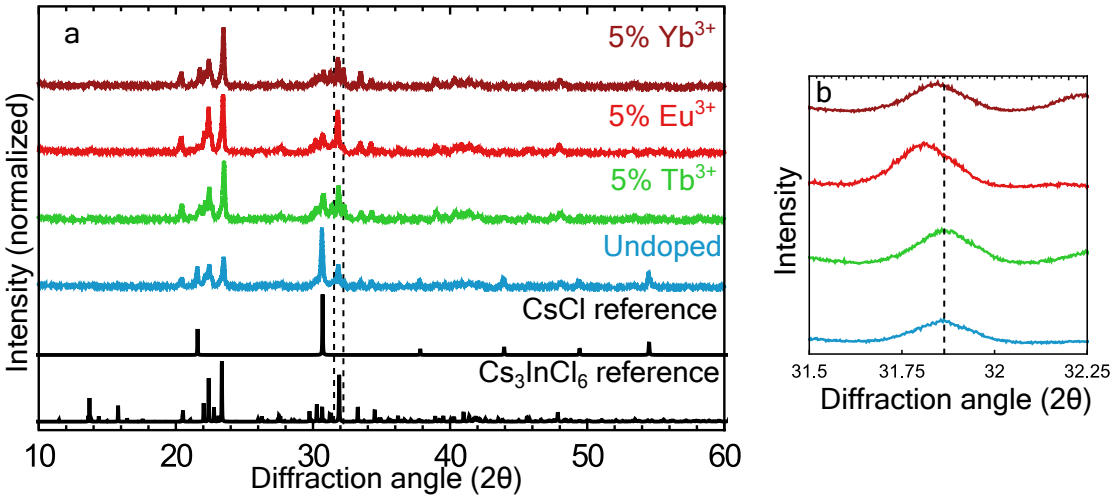

Figure 4.33: (a) X-ray diffraction data of the Cs_3InCl_6 microcrystals with various lanthanide dopants synthesized by solid state reaction in an evacuated quartz tube. Cs_3InCl_6 reference and CsCl reference are supplied. **(b)** Magnification of the reflection peak at 31.8 2θ, showing the diffraction angle shift upon doping.

it seems that the solid state reaction in an evacuated quartz tube based on Meyer [42] is a more suitable synthesis strategy, as phase pure Ln^{3+}-doped Cs_3InCl_6 microcrystals are produced.

To investigate the optical properties of the lanthanide doped Cs_3InCl_6 microcrystals, we performed PL spectroscopy measurements. **Figure 4.34** presents the PL spectroscopy results of the various Cs_3InCl_6 microcrystals. The emission spectrum of the undoped sample **(a)** shows a broad cyan emission band centered around 500 nm. The excitation spectrum of the broad emission is a band centered around 290 nm. The Stokes shift of the emission is quite large. The broad band and large Stokes shift are characteristics of STE emission and this broad band has been attributed to STE's in previous reports [63, 64]. The fact that the emission originates from STE indicates that the excitation band at 290 nm is the host absorption band. Interestingly, the emission is quite intense compared to STE emission of our previously discussed materials. It seems that quenching of the STE due to thermal crossover is not as strong as in the smaller band gap materials we have previously discussed. This could be because the emission is higher in energy. Therefore the STE state must be located higher above the ground state in the CC diagram. Consequently, the crossover point of the STE state to the ground state could be positioned at higher energies.

Regarding the doped Cs_3InCl_6 microcrystals, the PL spectra of the Yb^{3+}-doped nanocrystals are shown in **figure 4.34 (b)**. Interestingly, upon doping the host emission completely disappears. There is a very weak emission present from the Yb^{3+} dopant at 1000 nm. When we measure an excitation spectrum of this emission, a very noisy spectrum is obtained. The excitation starts around 300 nm and increases sharply, but the signal is very low. It seems that the incorporation of Yb^{3+} suppresses the host STE emission. Possibly, when the charge carriers are generated, they are trapped on Yb^{3+} centers or defects induced by Yb^{3+} doping before self trapping occurs. However, it seems that this trapping does not result in efficient sensitization of the Yb^{3+} emission. If trapping on the Yb^{3+} centers does occur, an explanation for the lacking sensitization could be that the Yb^{2+} state is located higher within the band gap in the indium based elpasolites compared to the bismuth based elpasolites.

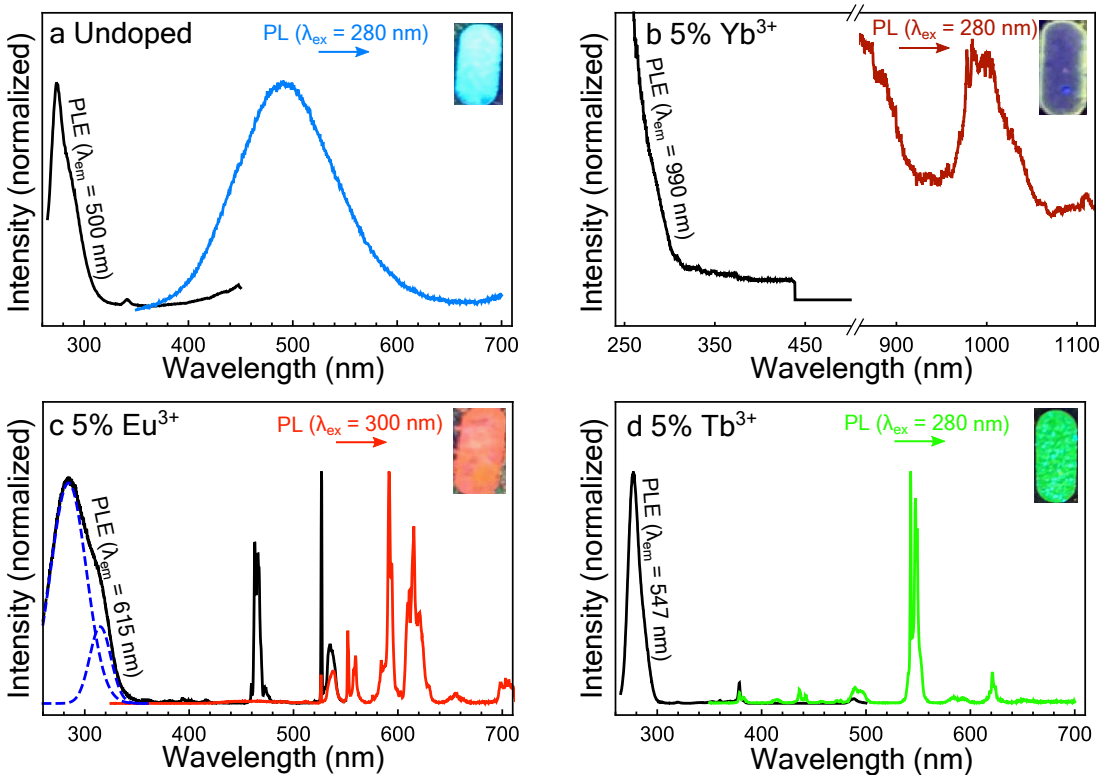

Figure 4.34: Photoluminescence (excitation) spectra of the synthesized **(a)** undoped and **(b)** 5% Yb^{3+}-, **(c)** Eu^{3+}- and **(d)** Tb^{3+}-doped Cs_3InCl_6 microcrystals. The deconvulution of the Eu^{3+} excitation band was done by fitting two Gaussian functions to the curve (R^2 = 0.9998). The insets in the figures are photographs of the samples under UV-light illumination.

If we look back at **figure 4.21 (b)**, in $Cs_2AgBiBr_6$:Yb^{3+} the Yb^{2+} + h_{vb}^+ CT band overlaps with the $^7F_{5/2}$ state of Yb^{3+}. If the Yb^{2+} + h_{vb}^+ CT band is shifted upwards as a result of the higher position within the band gap, the overlap might decrease resulting in less crossover to the $^7F_{5/2}$ state, shown in **figure 4.35**. This would explain the weak sensitization. If this is the case, it would be interesting to investigate whether any charge transfer luminescence occurs in this material. CT luminescence is a process which is seen in some Yb^{3+}-doped crystals [31]. It involves radiative decay from the CT band to the $^7F_{5/2}$ or $^7F_{7/2}$ levels of Yb^{3+}.

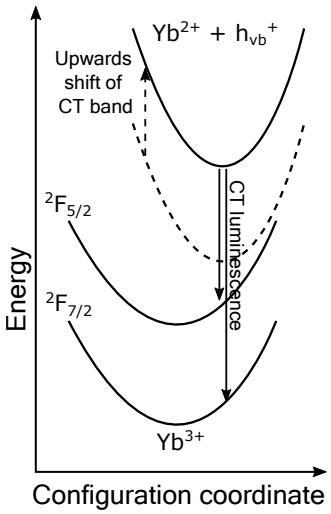

Figure 4.35: Configuration coordinate diagram showing the upwards shift of the CT band and the CT luminescence that could occur.

When we look at the PL spectra of the Eu^{3+}-doped material (**fig. 4.34 (c)**), we see the characteristic emission lines from Eu^{3+}. The lower relative intensity of the $^5D_0 \longrightarrow {}^7F_2$ shows that Eu^{3+} is incorporated in a site with inversion symmetry, as is expected if it substitutes In^{3+} in the lattice. Compared to the Yb^{3+}-doped sample, it has significantly more intense emission. The excitation spectrum shows a broad band at 300 nm. The excitation band can be deconvoluted into 2 separate bands, shown by the blue dashed lines. One band centered around 315 nm and one more intense band centered around 285 nm. It is possible that the band at 315 nm is due to charge transfer

absorption and the band at 285 nm is due to host absorption. However, the 285 nm band is slightly broader than the excitation band seen in the undoped material, so it is not certain that it has the same origin. More investigation is needed to confirm if the Eu^{3+} emission is sensitized by the host material. It is likely though, since the STE emission completely disappears upon Eu^{3+} doping. This suggests that the doping with Eu^{3+} somehow prevents the self-trapping of excitons when they are generated. It is only logical to think that this happens due to the trapping of charge carriers on Eu^{3+} centers. A subsequent step to sensitize the Eu^{3+} center would be a very plausible next step. Compared to Yb^{3+}, sensitization of Eu^{3+} through the CT state is significantly more likely when the CT band is located higher in energy, since Eu^{3+} has many more available energy levels above the $^5D_0$ levels to which crossover can occur from the CT state. This would explain why the Eu^{3+}-doped material has significantly more intense luminescence compared to the Yb^{3+}-doped material.

Lastly, the spectroscopy results of the Tb^{3+}-doped Cs_3InCl_6 microcrystals are shown in **figure 4.34 (d)**. The emission spectrum shows a very intense sharp peak at 545 nm. There are several other less intense peaks. The excitation spectrum show that the emission is excited in an intense band at 280 nm. This emission originates from the $^5D_4 \longrightarrow {}^7F_n$ transitions of Tb^{3+}. In this material the STE emission has completely disappeared upon doping as well. The excitation band of the Tb^{3+} emission is located at the same wavelength as the host emission excitation band of the undoped material. This strongly suggest that the Tb^{3+} emission is sensitized by the host material. The signal while measuring the Tb^{3+} emission was an order of magnitude higher than the Eu^{3+}-doped sample, indicating that the emission of Tb^{3+} is excited very efficiently in the UV absorption band relative to the Eu^{3+} doped sample. It would be interesting to perform PL quantum yield measurements to investigate whether the quantum yield actually increases upon doping with Tb^{3+}, compared to the undoped material.

It is important to discuss the sensitization of Tb^{3+} in this material. If the Yb^{3+} and Eu^{3+} emission is sensitized by the host in Cs_3InCl_6, it seems plausible that it follows a similar mechanism to what is discussed in section 4.1.2 for Yb^{3+} in $Cs_2AgBiBr_6$. However, while it is possible for an electron to be trapped on Eu^{3+} or Yb^{3+} to reduce it to oxidation state (II), this is not likely for Tb^{3+}. Terbium is not easily reduced to oxidation state (II). However, this does not invalidate our proposed energy transfer mechanism for Tb^{3+}. Tb^{3+} is not easily reduced to oxidation state (II), but it is rather easily oxidized to oxidation state (IV). This means that instead of sensitization through the $Ln^{2+} + h^+_{VB}$ CT state, sensitization could occur via a $Tb^{4+} + e^-_{CB}$ CT state. In this process, the hole would be trapped first on the Tb^{3+} center, oxidizing it to Tb^{4+}. Then from this $Tb^{4+} + e^-_{CB}$ CT state, crossover to the $^5D_4$ level can occur as well as to the energy levels located above the $^5D_4$ level. To investigate the sensitization mechanism of the lanthanide emission in the materials, it would be insightful to investigate the PL properties at low doping concentrations or cryogenic temperatures. In these measurements STE emission could be present simultaneously with lanthanide luminescence. Then the effect of Ln^{3+} doping on the host emission can be studied more thoroughly. PL decay measurements can for example indicate whether sensitization occurs through the STE or not. Nevertheless, these results show that Cs_3InCl_6 is an excellent host for the incorporation of Tb^{3+} and Eu^{3+}.

Our observation of the significant increase in Eu^{3+} luminescence in the Cs_3InCl_6 microcrystals further substantiates our hypothesis that the indium based elpasolites experience less CT quenching. Selecting crystals with a lower lying valence band results in stronger Eu^{3+} luminescence in our case. The intensity of the Eu^{3+} luminescence in the various chloride elpasolite crystals has the order $Cs_3InCl_6 > Cs_2NaBiCl_6 > Cs_2AgInCl_6 > Cs_2AgBiCl_6$. This suggests that the

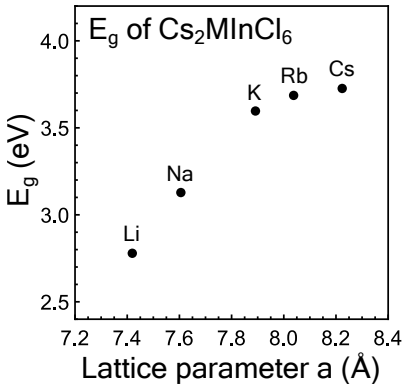

Figure 4.36: The change of the band gap due to the lattice contraction of smaller M^+ ions in Cs_2MInCl_6

substitution of Ag^+ by an alkali cation has a greater impact on the luminescence quenching than substitution of Bi^{3+} by In^{3+}. This makes sense, since the 4d orbitals of Ag^+ have significantly more contribution to the VBM than the Bi^{3+} 6s orbitals [65, 66]. This means substituting either of these ions with an ion that does not contribute to the VBM would have a more profound effect on the Ag^+ case. It would be interesting to investigate the quenching temperatures of the different Eu^{3+}-doped materials. This would be a more robust way of investigating the effect of the various ions on the luminescence of Eu^{3+}. In this experiment, it might be preferred to compare the materials with $Cs_2NaInCl_6$ instead of Cs_3InCl_6 to increase the similarity between the materials. Regardless of this experiment, $Cs_2NaInCl_6$ would be an interesting crystal to investigate for Eu^{3+} and Tb^{3+} doping. The reduction of the lattice parameters upon substitution could reduce the band gap, shifting it slightly more to the blue region. The contraction of the lattice can lead to a smaller band gap, because the decreased bond lengths can increase orbital overlap between the octahedra in the lattice [67, 68]. **Figure 4.36** shows the effect of lattice contraction of Cs_2MInCl_6 (M = Li, Na, K, Rb, Cs) on the band gap, based on values taken from the Materials Project [69]. Note that the calculations underestimate the band gap of the materials [70]. A clear upward trend is seen when increasing the lattice parameters. While the band gap likely will not decrease enough to efficiently absorb in the blue region, $Cs_2NaInCl_6$ is definitely worth investigating for Eu^{3+} and Tb^{3+} doping (as well as $Cs_2LiInCl_6$).

Another method to shift the absorption band to lower energies is to substitute Cl^- for Br^-. It is known that in perovskites the band gap decreases when going down the halides in the periodic table and that partial substitution of the halides is possible and leads to gradual band gap evolutions [39, 71]. Substitution of Cl^- for Br^- has the risk of increased Ln^{3+} quenching through the CT state though, because the substitution should lower the lanthanide charge transfer band energy [72]. To investigate the effect of Br^- substitution, we synthesized Cs_3InCl_6 microcrystals with 50% substitution of Cl^- by Br^- ($Cs_3InCl_3Br_3$) and doped the crystals with 5% Eu^{3+} and Tb^{3+}. We use the same synthesis we used for the Cs_3InCl_6 microcrystals with the modification of using CsBr as precursor instead of CsCl. This resulted in stochiometrically equal amounts of Cl^- and Br^- in the precursor mix.

To investigate the structural properties of the undoped, 5% Eu^{3+}- and 5% Tb^{3+}-doped $Cs_3InCl_3Br_3$ microcrystals, we performed XRD measurements. The results of the XRD measurements are shown in **figure 4.37 (a)**. The reference XRD pattern of Cs_3InCl_6 is adjusted to shift the diffraction peaks to match the experimental patterns due to the lattice expansion upon substitution of Br^-. The peak positions of the undoped and Tb^{3+}-doped samples match the

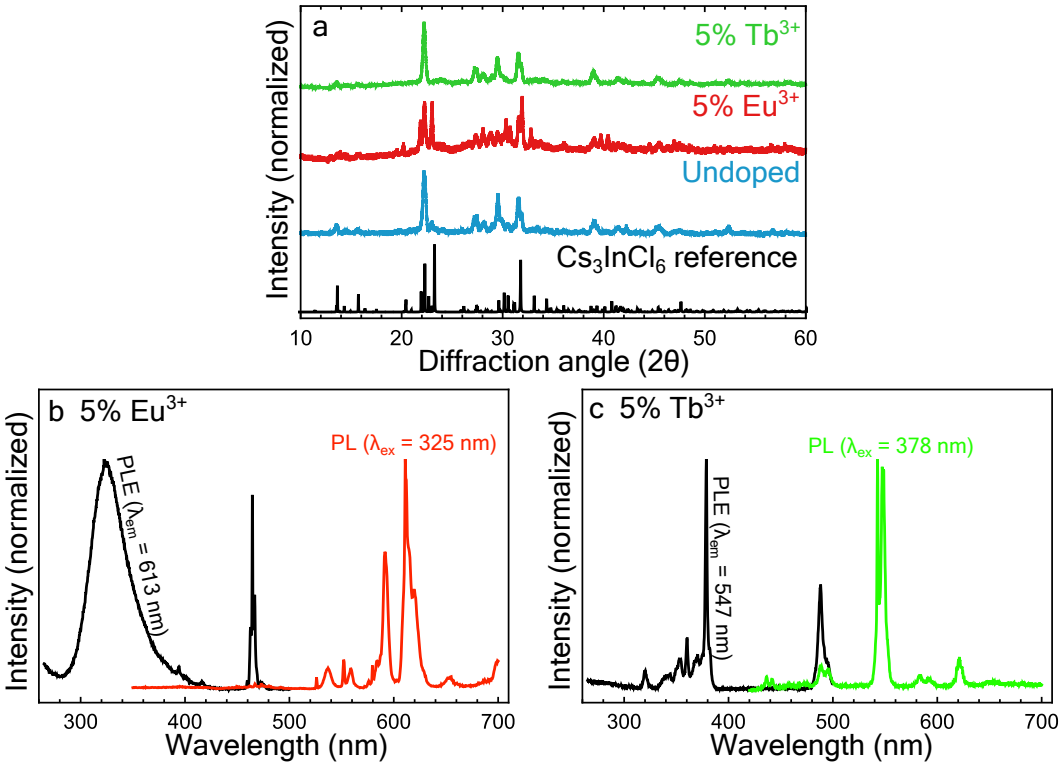

Figure 4.37: Characterization data of the undoped, 5% Eu^{3+}- and Tb^{3+}-doped $Cs_3InCl_3Br_3$ microcrystals. **(a)** XRD patterns of the synthesized microcrystals with a reference pattern of Cs_3InCl_6, corrected to match the diffraction angles of the experimental patterns. **(b)** Emission and excitation spectra of the 5% Eu^{3+}-doped material. **(c)** Emission and excitation spectra of the 5% Tb^{3+}-doped material.

reference pattern, however the relative peak intensities seem to be changed after Br^- substitution. The Eu^{3+}-doped samples shows the same peaks, however this pattern also has some other peaks. Many of the peaks seem to be split in two, indicating that possibly two phases are present in which one is predominantly Cl^- and the other Br^-. While the crystal structure seems to have formed judging from the XRD patterns, it is difficult to draw conclusions of the phase purity of the samples, since there is no reference pattern available for the partially substituted crystal $Cs_3inCl_3Br_3$.

Regardless of the questionable phase purity of the synthesized $Cs_3InCl_3Br_3$ microcrystals, we investigate the photoluminescence properties of the synthesized microcrystals. **Figure 4.37 (b)** and **(c)** show the emission and excitation spectra of the 5% Eu^{3+}- and Tb^{3+}-doped $Cs_3InCl_3Br_3$ microrystals. The undoped sample did not show any luminescence so it is not included. The Eu^{3+}-doped sample shows the characteristic luminescence of Eu^{3+}. Compared to the Cs_3InCl_6 microcrystals, the relative intensity of the $^5D_0 \longrightarrow {}^7F_2$ is higher. This indicates that the substitution for Br^- likely is successful to some extent, as incorporation of Br^- would lead to mixed halide $[EuX_6]^{3-}$ octahedra, breaking the inversion symmetry. The Eu^{3+} emission is excited in a broad band centered around 330 nm. This is red-shifted by about 40 nm compared to the Eu^{3+}-doped Cs_3InCl_6 microcrystals. Since we were not able to measure an excitation spectrum of the host emission it is difficult to say whether this absorption band is due to host absorption. However, the Tb^{3+}-doped sample does not show a broad excitation band at all, shown in **figure 4.37 (c)**. Therefore, it is likely that the Eu^{3+} absorption band is not host excitation either, but rather a charge transfer absorption band. The location of the charge

transfer band also shifts to higher wavelengths when substituting Cl^- for Br^-. Regarding the spectra of the Tb^{3+}-doped sample in **figure 4.37 (c)**, only excitation lines of f-f transitions of Tb^{3+} are present. This shows there is no host absorption for Tb^{3+}. However there is also no f-d absorption band. This strengthens our case that Tb^{3+} is host sensitized in Cs_3InCl_6, since the absence of an f-d absorption band in $Cs_3InCl_3Br_3$ decreases the likelihood that the 285 nm band absorption in Cs_3InCl_6 is due to an f-d transition.

The question is why there is no host absorption or emission in this material. This could have several explanations: (1) the $Cs_3InCl_3Br_3$ crystal structure is not properly formed. This is possible since the results of the XRD measurements are questionable. (2) The energy transfer is hindered by the substitution. The fact that the undoped crystal is not luminescent at all is indicative that the charge carrier dynamics are different in this material. Possibly, the partial substitution of Cl^- by Br^- results in a substantial amount of defects in the material, where charge carriers are trapped on defects before being able to recombine or sensitize the lanthanides.

Our results indicate that the indium-based elpasolite Cs_3InCl_6 is an excellent host material for Eu^{3+} and Tb^{3+}. The materials show narrow red and green emission from the Eu^{3+} and Tb^{3+} dopants, desired for display lighting applications. The luminescence of the lanthanides is excited in an intense absorption band at 290 nm, which is likely due to host absorption. The absorption in this region is strong, showing their potential for small scale applications such as MicroLED. A logical next step would be to reduce the size by synthesizing the nanocrystals. There are a couple of reports which synthesized these nanocrystals with different procedures [63, 64]. One synthesis is a room temperature ligand assisted anti solvent precipitation and the other is a hot-injection synthesis. It can be argued that for doping lanthanides the hot injection method is preferable. The high temperature of the hot injection method should promote the incorporation of the lanthanides. A room temperature synthesis may struggle with incorporation of the lanthanides. It would be interesting to see the materials performance in nanocrystalline form. One drawback to the material is the relatively high energy absorption band located in the UV. Strong absorption in the blue light range is desirable if the material is used for display lighting applications. To shift the absorption band to the blue range, the composition of the crystal could be tweaked further. Investigating Li or Na as a substitution for Cs^+ is a possible option, as well as further exploring the substitution of Cl^- by Br^-.

Chapter 5

Conclusion and outlook

Elpasolite semiconductor nanocrystals are an interesting alternative to lead-halide perovskite nanocrystals. Like lead halide perovskites, the elpasolite semiconductors have very strong absorption, but contrary to lead-halide perovskites they are stable and non-toxic. Doping the elpasolites with lanthanides is a promising method to improve the photoluminescence properties. They have potential for use in phosphors for microLED applications. Phosphors for microLED must be strongly absorbing, have very small dimensions and emit narrow band red and green emission. The desired narrow band red and green emission can be attained by doping with the lanthanides Eu^{3+} and Tb^{3+}. The challenge is to have efficient sensitization of the lanthanide dopants by the host material through energy transfer. The mechanism of this energy transfer is often not well-understood. In this thesis we report the study of various elpasolite crystals doped with lanthanides Yb^{3+}, Eu^{3+} and Tb^{3+}.

We investigated several elpasolite systems and their potential for lanthanide doping. most of the elpasolite materials showed weak host luminescence due to self-trapped excitons. Lanthanide doping helped to improve the emission characteristics in some crystals. Yb^{3+} doping in $Cs_2AgBiCl_6$ and $Cs_2AgBiBr_6$ lead to host sensitized near-IR Yb^{3+} emission as was reported by others [18, 19]. We observed red Eu^{3+} luminescence in $Cs_2NaBiCl_6$, $Cs_2AgInCl_6$ and Cs_3InCl_6. In $Cs_2AgBiCl_6$ the Eu^{3+} emission was quenched due to charge transfer quenching. In $Cs_2NaBiCl_6$ and $Cs_2AgInCl_6$, Eu^{3+} emission was only present when directly exciting into the f-orbital energy levels of Eu^{3+}. In Cs_3InCl_6, the Eu^{3+} emission was excited in an intense band at 290 nm, possibly due to host absorption. Regarding Tb^{3+} doping, we observed characteristic green Tb^{3+} emission in $Cs_2AgBiCl_6$ and Cs_3InCl_6. The Tb^{3+} emission in $Cs_2AgBiCl_6$ was very weak and seemed to be excited in an f-d absorption band, not by host excitation. In Cs_3InCl_6, the Tb^{3+} emission was intense and excited in the host absorption band at 290 nm, suggesting an energy transfer process from host to lanthanide.

We found that there is a trend in the amount of charge transfer quenching of Eu^{3+} in the different elpasolites. The intensity of the Eu^{3+} emission is in the order $Cs_3InCl_6 > Cs_2NaBiCl_6 > Cs_2AgInCl_6 > Cs_2AgBiCl_6$. We concluded that substitution of Bi^{3+} by In^{3+} results in less charge transfer quenching and even more so when substituting Ag^+ by an alkali metal cation. This was attributed to a lowering of the valence band maximum. The substitution of Bi^{3+} by In^{3+} removes the contribution to the valence band maximum of the bismuth 6s orbitals, effectively lowering the valence band maximum as In^{3+} does not contribute to the valence band maximum significantly. The same was true for the substitution of Ag^+ by an alkali metal cation. The contribution of the 4d orbitals of Ag^+ to the valence band maximum is removed and the alkali

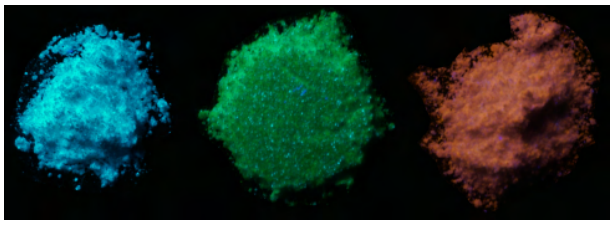

Figure 5.1: Photograph of our Cs_3InCl_6 microcrystals without doping (left), 5% Tb^{3+} doping (middle) and 5% Eu^{3+} doping (right)

metal cations valence orbitals are located deep in the valence band. The lowering of the valence band maximum effectively increases the $Eu^{2+} + h_{vb}^+$ charge transfer state in energy, which results in less overlap of the charge transfer state with the ground state and thus less non-radiative decay from the charge transfer state to the ground state.

We conducted thorough analysis on the sensitization of Yb^{3+} in the elpasolite $Cs_2AgBiBr_6$. The debate is whether the sensitization of Yb^{3+} occurs through the self-trapped exciton state or that the sensitization occurs directly from free excitons. We have concluded that the STE state is not involved in the energy transfer process as photoluminescence decay measurements of the undoped and 5% Yb^{3+}-doped $Cs_2AgBiBr_6$ nanocrystals revealed that there is no difference in lifetime of the STE between the undoped and the 5% Yb^{3+}-doped material. Combined with the findings of Schmitz *et al.* [18] that an $Yb^{2+} + h_{vb}^+$ charge transfer state is located within the band gap, we concluded that the energy transfer mechanism likely occurs through the trapping of photoexcited electrons from the conduction band on Yb centers to form a $Yb^{2+} + h_{vb}^+$ charge transfer state, followed by non-radiative relaxation to the $^7F_{5/2}$ excited state of Yb^{3+}, from which the characteristic 1000 nm emission from Yb^{3+} occurs.

Our findings provide motivation to investigate doping of lanthanides in elpasolite materials. We have shown that the absorption of lanthanides can be significantly increased by sensitizing the lanthanides with charge carriers in elpasolite semiconductors. We hope our research improves the understanding of lanthanide luminescence in this class of materials. The materials we researched are just the tip of an iceberg of many more materials that can be researched. Other crystals compositions can be investigated as well as alloying of the crystal ions.

While the photoluminescence properties of the lanthanide doped Cs_3InCl_6 material are a good proof of principle of effectively increasing the absorption of lanthanides, there are still challenges to be overcome before it could be suitable for application. The absorption band is located at relatively high energies. For applications for microLED, it is desired to have strong absorption in the blue region from 430 to 450 nm to be effectively excited by a blue LED.

Finally, further research should be directed to investigation on how to shift the absorption band to lower energies while limiting charge transfer quenching in Cs_3InCl_6. Substitution of Cl^- by Br^- could be investigated further as well as the substituting the sixfold coordinated Cs^+ for a smaller cation such as Li^+ or Na^+ yielding $Cs_2LiInCl_6$ or $Cs_2NaInCl_6$. Efforts should also be made to synthesize the nanocrystals of Cs_3InCl_6. With this further research, the material could improve to achieve the desirable properties needed for microLED applications.

Acknowledgements

I would like to wholeheartedly thank Jur de Wit. We've had some good laughs in between our fruitful discussions. You helped me ground my thoughts when I went down another rabbit hole of some weird theory. You provided me with great guidance and definitely helped me through the project and were always greatly involved. Next I would like to thank Andries Meijerink for giving me the opportunity to do this project. The great passion and knowledge you have for the field of luminescence is contagious and the discussions we had every other week were the source of many of the insights in this project. Finally, the Condensed Matter and Interfaces group deserves my thanks for providing me with a great working environment even during Corona times.

Bibliography

1. Chen, H.-W., Lee, J.-H., Lin, B.-Y., Chen, S. & Wu, S.-T. Liquid crystal display and organic light-emitting diode display: present status and future perspectives. *Light: Science & Applications* **7,** 17168–17168 (2018).
2. Chansin, G. LCD fights back against OLED with MiniLED backlight technology. *Information Display* **37,** 49–51 (2021).
3. Hunt, R. W. G. *The reproduction of colour* (John Wiley & Sons, 2005).
4. Liu, B.-M., Huang, L., Xuan, T.-T. & Wang, J. in *Phosphor Handbook* 1–32 (CRC Press, 2022).
5. Jin, S., Li, J., Li, J., Lin, J. & Jiang, H. GaN microdisk light emitting diodes. *Applied Physics Letters* **76,** 631–633 (2000).
6. Jiang, H., Jin, S., Li, J., Shakya, J. & Lin, J. III-nitride blue microdisplays. *Applied Physics Letters* **78,** 1303–1305 (2001).
7. Wu, T. *et al.* Mini-LED and micro-LED: promising candidates for the next generation display technology. *Applied Sciences* **8,** 1557 (2018).
8. Murphy, J. *et al. 11.1: Invited Paper: Narrow-Band Phosphors for Next Generation MiniLED and MicroLED Displays* in *SID Symposium Digest of Technical Papers* **52** (2021), 165–168.
9. Dai, X. *et al.* Solution-processed, high-performance light-emitting diodes based on quantum dots. *Nature* **515,** 96–99 (2014).
10. Chen, H.-S., Hsu, C.-K. & Hong, H.-Y. Ingan-cdse-znse quantum dots white LEDs. *Ieee photonics technology letters* **18,** 193–195 (2005).
11. Dutta, P. & Khanna, A. Eu3+ activated molybdate and tungstate based red phosphors with charge transfer band in blue region. *ECS Journal of Solid State Science and Technology* **2,** R3153 (2012).
12. Wang, H.-C. *et al.* Mesoporous silica particles integrated with all-inorganic CsPbBr3 perovskite quantum-dot nanocomposites (MP-PQDs) with high stability and wide color gamut used for backlight display. *Angewandte Chemie International Edition* **55,** 7924–7929 (2016).
13. Huang, H., Bodnarchuk, M. I., Kershaw, S. V., Kovalenko, M. V. & Rogach, A. L. Lead halide perovskite nanocrystals in the research spotlight: stability and defect tolerance. *ACS energy letters* **2,** 2071–2083 (2017).
14. McClure, E. T., Ball, M. R., Windl, W. & Woodward, P. M. Cs2AgBiX6 (X= Br, Cl): new visible light absorbing, lead-free halide perovskite semiconductors. *Chemistry of Materials* **28,** 1348–1354 (2016).

15. Khalfin, S. & Bekenstein, Y. Advances in lead-free double perovskite nanocrystals, engineering band-gaps and enhancing stability through composition tunability. *Nanoscale* **11,** 8665–8679 (2019).

16. Liu, Y. *et al.* Incorporating Rare-Earth Terbium (III) Ions into Cs2AgInCl6: Bi Nanocrystals toward Tunable Photoluminescence. *Angewandte Chemie International Edition* **59,** 11634–11640 (2020).

17. Liu, Y., Molokeev, M. S. & Xia, Z. Lattice doping of lanthanide ions in Cs2AgInCl6 nanocrystals enabling tunable photoluminescence. *Energy Material Advances* **2021** (2021).

18. Schmitz, F. *et al.* Lanthanide-Induced Photoluminescence in Lead-Free Cs2AgBiBr6 Bulk Perovskite: Insights from Optical and Theoretical Investigations. *The Journal of Physical Chemistry Letters* **11,** 8893–8900 (2020).

19. Chen, N. *et al.* Yb-and Mn-doped lead-free double perovskite Cs2AgBiX6 (X= Cl–, Br–) nanocrystals. *ACS applied materials & interfaces* **11,** 16855–16863 (2019).

20. Blasse, G. & Grabmaier, B. in *Luminescent materials* (Springer, 1994).

21. CIE, C. Commission internationale de l'eclairage proceedings, 1931. *Cambridge University, Cambridge* (1932).

22. Huang, Y., Hsiang, E.-L., Deng, M.-Y. & Wu, S.-T. Mini-LED, Micro-LED and OLED displays: Present status and future perspectives. *Light: Science & Applications* **9,** 1–16 (2020).

23. Bransden, B. & Joachain, C. *Quantum Mechanics* ISBN: 9780582356917 (Prentice Hall, 2000).

24. Lax, M. The Franck-Condon principle and its application to crystals. *The Journal of chemical physics* **20,** 1752–1760 (1952).

25. Hook, J. R. & Hall, H. E. *Solid state physics* (John Wiley & Sons, 2013).

26. Reshchikov, M. A. Mechanisms of thermal quenching of defect-related luminescence in semiconductors. *physica status solidi (a)* **218,** 2000101 (2021).

27. Shamsi, J., Urban, A. S., Imran, M., De Trizio, L. & Manna, L. Metal halide perovskite nanocrystals: synthesis, post-synthesis modifications, and their optical properties. *Chemical reviews* **119,** 3296–3348 (2019).

28. Krames, M. R. *et al.* Status and future of high-power light-emitting diodes for solid-state lighting. *Journal of display technology* **3,** 160–175 (2007).

29. Tucureanu, V., Matei, A. & Avram, A. Synthesis and characterization of YAG: Ce phosphors for white LEDs. *Opto-electronics review* **23,** 239–251 (2015).

30. Marin, R. & Jaque, D. Doping lanthanide ions in colloidal semiconductor nanocrystals for brighter photoluminescence. *Chemical Reviews* **121,** 1425–1462 (2020).

31. Van Pieterson, L., Heeroma, M., De Heer, E. & Meijerink, A. Charge transfer luminescence of Yb3+. *Journal of Luminescence* **91,** 177–193 (2000).

32. Wensky, D. & Moulton, W. Energy levels of Pr3+ in various crystal hosts. *The Journal of Chemical Physics* **53,** 3957–3969 (1970).

33. Dieke, G. H. Spectra and Energy Levels of Rare Earth Ions in Crystals. (1968).

34. Blasse, G. & Sabbatini, N. The quenching of rare-earth ion luminescence in molecular and non-molecular solids. *Materials chemistry and physics* **16,** 237–252 (1987).

35. Dorenbos, P. Systematic behaviour in trivalent lanthanide charge transfer energies. *Journal of Physics: Condensed Matter* **15,** 8417 (2003).

36. Bos, A. J., Dorenbos, P., Bessière, A. & Viana, B. Lanthanide energy levels in YPO4. *Radiation Measurements* **43,** 222–226 (2008).

37. Dorenbos, P. Absolute location of lanthanide energy levels and the performance of phosphors. *Journal of luminescence* **122,** 315–317 (2007).

38. Pidol, L., Viana, B., Galtayries, A. & Dorenbos, P. Energy levels of lanthanide ions in a Lu 2 Si 2 O 7 host. *Physical Review B* **72,** 125110 (2005).

39. Creutz, S. E., Crites, E. N., De Siena, M. C. & Gamelin, D. R. Colloidal nanocrystals of lead-free double-perovskite (elpasolite) semiconductors: synthesis and anion exchange to access new materials. *Nano letters* **18,** 1118–1123 (2018).

40. Morss, L. R., Siegal, M., Stenger, L. & Edelstein, N. Preparation of cubic chloro complex compounds of trivalent metals: Cs2NaMCl6. *Inorganic Chemistry* **9,** 1771–1775 (1970).

41. Volonakis, G. *et al.* Cs2InAgCl6: a new lead-free halide double perovskite with direct band gap. *The journal of physical chemistry letters* **8,** 772–778 (2017).

42. Meyer, G. Zur Kenntnis der Chloro-und Bromo-Indate (III). A3In2Cl9 (A= Cs, Rb, In, Tl) und Cs3In2Br9- x Clx (x= 0, 3, 6, 7, 8). *Zeitschrift für anorganische und allgemeine Chemie* **445,** 140–146 (1978).

43. Stump, N. A., Schweitzer, G. K., Gibson, J. K., Haire, R. G. & Peterson, J. R. Luminescence study of the thermal decomposition of europium trichloride hexahydrate, EuCl 3· 6H 2 O. *Applied spectroscopy* **48,** 937–944 (1994).

44. Wendlandt, W. The thermal decomposition of the heavier rare earth metal chloride hydrates. *Journal of Inorganic and Nuclear Chemistry* **9,** 136–139 (1959).

45. Momma, K. & Izumi, F. VESTA: a three-dimensional visualization system for electronic and structural analysis. *Journal of Applied crystallography* **41,** 653–658 (2008).

46. Gražulis, S. *et al.* Crystallography Open Database–an open-access collection of crystal structures. *Journal of applied crystallography* **42,** 726–729 (2009).

47. Jain, A. *et al.* Commentary: The Materials Project: A materials genome approach to accelerating materials innovation. *APL materials* **1,** 011002 (2013).

48. Levy, S. *et al.* The Role Silver Nanoparticles Plays in Silver-Based Double-Perovskite Nanocrystals. *Chemistry of Materials* **33,** 2370–2377 (2021).

49. Zhang, L. *et al.* Tuning emission and electron–phonon coupling in lead-free halide double perovskite Cs2AgBiCl6 under pressure. *ACS Energy Letters* **4,** 2975–2982 (2019).

50. De Roo, J. *et al.* Highly dynamic ligand binding and light absorption coefficient of cesium lead bromide perovskite nanocrystals. *ACS nano* **10,** 2071–2081 (2016).

51. Wright, A. D. *et al.* Ultrafast excited-state localization in Cs2AgBiBr6 double perovskite. *The journal of physical chemistry letters* **12,** 3352–3360 (2021).

52. Belsky, A. & Krupa, J. Luminescence excitation mechanisms of rare earth doped phosphors in the VUV range. *Displays* **19,** 185–196 (1999).

53. Bizarri, G. Scintillation mechanisms of inorganic materials: From crystal characteristics to scintillation properties. *Journal of Crystal Growth* **312,** 1213–1215 (2010).

54. Zhu, D. *et al.* Compositional Tuning of Carrier Dynamics in Cs2Na1–x Ag x BiCl6 Double-Perovskite Nanocrystals. *ACS energy letters* **5,** 1840–1847 (2020).

55. Serra, O. & Thompson, L. Emission spectra of cesium sodium europium chloride (Cs2NaEuCl6) and cesium sodium europium yttrium chloride (Cs2Na (Eu, Y) Cl6). *Inorganic Chemistry* **15,** 504–507 (1976).

56. Smit, W., Dirksen, G. & Stufkens, D. Infrared and Raman spectra of the elpasolites Cs2NaSbCl6 and Cs2NaBiCl6: Evidence for a pseudo Jahn-Teller distorted ground state. *Journal of Physics and Chemistry of Solids* **51,** 189–196 (1990).

57. Jiang, J. *et al.* Transformation between the Dark and Bright Self-Trapped Excitons in Lead-Free Double-Perovskite Cs2NaBiCl6 under Pressure. *The Journal of Physical Chemistry Letters* **12,** 7285–7292 (2021).

58. Lamba, R. S., Basera, P., Singh, S., Bhattacharya, S. & Sapra, S. Lead-Free Alloyed Double-Perovskite Nanocrystals of Cs2 (Na x Ag1–x) BiBr6 with Tunable Band Gap. *The Journal of Physical Chemistry C* **125,** 1954–1962 (2021).

59. NAG, A. & KSHIRSAGAR, A. S. Synthesis and optical properties of colloidal Cs2AgSb1-xBixCl6 double perovskite nanocrystals (2019).

60. Liu, Y., Nag, A., Manna, L. & Xia, Z. Lead-free double perovskite Cs2AgInCl6. *Angewandte Chemie* **133,** 11696–11707 (2021).

61. Meng, W. *et al.* Parity-forbidden transitions and their impact on the optical absorption properties of lead-free metal halide perovskites and double perovskites. *The journal of physical chemistry letters* **8,** 2999–3007 (2017).

62. Du, K.-z., Meng, W., Wang, X., Yan, Y. & Mitzi, D. B. Bandgap engineering of lead-free double perovskite Cs2AgBiBr6 through trivalent metal alloying. *Angewandte Chemie International Edition* **56,** 8158–8162 (2017).

63. Zhang, F. *et al.* Room-temperature synthesis of blue-emissive zero-dimensional cesium indium halide quantum dots for temperature-stable down-conversion white light-emitting diodes with a half-lifetime of 186 h. *Materials Horizons* **8,** 3432–3442 (2021).

64. Huang, J. *et al.* Controlled Structural Transformation in Sb-Doped Indium Halides A3InCl6 and A2InCl5. H2O Yields Reversible Green-to-Yellow Emission Switch. *Advanced Optical Materials* **9,** 2002267 (2021).

65. Guechi, N., Bouhemadou, A., Bin-Omran, S., Bourzami, A. & Louail, L. Elastic, Optoelectronic and Thermoelectric Properties of the Lead-Free Halide Semiconductors Cs2AgBiX 6 (X= Cl, Br): Ab Initio Investigation. *Journal of Electronic Materials* **47,** 1533–1545 (2018).

66. Lamba, R. S., Basera, P., Bhattacharya, S. & Sapra, S. Band Gap Engineering in Cs2 (Na x Ag1–x) BiCl6 Double Perovskite Nanocrystals. *The Journal of Physical Chemistry Letters* **10,** 5173–5181 (2019).

67. Zhang, L. *et al.* Pressure-induced emission enhancement, band-gap narrowing, and metallization of halide perovskite Cs3Bi2I9. *Angewandte Chemie International Edition* **57,** 11213–11217 (2018).

68. Prasanna, R. *et al.* Band gap tuning via lattice contraction and octahedral tilting in perovskite materials for photovoltaics. *Journal of the American Chemical Society* **139,** 11117–11124 (2017).

69. Jain, A. *et al.* The Materials Project: A materials genome approach to accelerating materials innovation. *APL Materials* **1,** 011002. ISSN: 2166532X (2013).

70. Jain, A. *et al.* A high-throughput infrastructure for density functional theory calculations. *Computational Materials Science* **50,** 2295–2310 (2011).

71. Akkerman, Q. A. *et al.* Tuning the optical properties of cesium lead halide perovskite nanocrystals by anion exchange reactions. *Journal of the American Chemical Society* **137,** 10276–10281 (2015).

72. Dorenbos, P. Lanthanide charge transfer energies and related luminescence, charge carrier trapping, and redox phenomena. *Journal of alloys and compounds* **488,** 568–573 (2009).